UNIVERSIDADE FEDERAL RURAL DE PERNAMBUCO
UNIDADE ACADÊMICA DO CABO DE SANTO AGOSTINHO
PROGRAMA DE PÓS-GRADUAÇÃO EM ENGENHARIA FÍSICA

STEPHANY DE MOURA SANTOS

Propagation in Light-Induced Photonic Structures and Study of the Velocity Redistribution of Excited Atoms in Cesium Rydberg Atom Spectroscopy

Cabo de Santo Agostinho - PE
2024

STEPHANY DE MOURA SANTOS

Propagation in Light-Induced Photonic Structures and Study of the Velocity Redistribution of Excited Atoms in Cesium Rydberg Atom Spectroscopy

Dissertation presented to the Postgraduate Program in Physical Engineering of the Academic Unit of Cabo de Santo Agostinho of the Federal Rural University of Pernambuco to obtain the title of Master in Physical Engineering.

Area of Concentration: Optoelectronics
Advisor: Prof. Dr. Sergio Vladimir Barreiro DiGiorgi
Co-Advisor: Prof. Dr. Weliton Soares Martins

Cabo de Santo Agostinho - PE
2024

Dados Internacionais de Catalogação na Publicação
Sistema Integrado de Bibliotecas da UFRPE
Bibliotecário(a): Ana Catarina Macêdo – CRB-4 1781

S237p Santos, Stephany de Moura.
Propagation in light-induced photonic structures and study of the velocity redistribution of excited atoms in cesium rydberg atom spectroscopy / Stephany de Moura Santos. – Cabo de Santo Agostinho, 2024.
102 f.; il.

Orientador(a): Sergio Vladimir Barreiro DeGiorgi.
Co-orientador(a): Weliton Soares Martins.

Dissertação (Mestrado) – Universidade Federal Rural de Pernambuco, Unidade Acadêmica Cabo de Santo Agostinho - UACSA, Programa de Pós-Graduação em Engenharia Física, Cabo de Santo Agostinho, BR-PE, 2024.

Inclui referências.

1. Luz - Propagação . 2. Césio. 3. Análise espectral. 4. Luz - Transmissão 5. Física - Estudo e ensino . I. DeGiorgi, Sergio Vladimir Barreiro, orient. II. Martins, Weliton Soares, coorient. III. Título

CDD 621

Stephany de Moura Santos

Propagation in Light-Induced Photonic Structures and Study of the Velocity Redistribution of Excited Atoms in Cesium Rydberg Atom Spectroscopy

Master's Dissertation presented to the Postgraduate Program in Physical Engineering, Academic Unit of Cabo de Santo Agostinho, Federal Rural University of Pernambuco, as a partial requirement for obtaining the title of Master in Physical Engineering.

APPROVED IN: 27/08/2024.

Examining Board

Prof. Sergio Vladimir Barreiro DiGiorgi - UFRPE
Advisor

Prof. Athanasios Laliotis - Université Sorbonne Paris Nord
External Examiner

Prof. Martine Patrícia Arlette Chevrollier – UFRPE
Internal Examiner

ACKNOWLEDGMENTS

Gostaria de expressar minha sincera gratidão a todos que contribuíram para a conclusão deste trabalho. Primeiramente, agradeço aos meus pais Elizabeth e Girles, pelo apoio incondicional em todas as minhas escolhas e pela confiança no meu potencial, o que sempre me motivou a seguir em frente. Ao meu noivo, Edilson Amaral, sou grata por me apoiar na busca dos meus sonhos, por querer vivenciá-los comigo e por sempre estar ao meu lado em cada passo desta jornada.

Aos meus amigos, que a física trouxe para minha vida, sou imensamente grata, em especial a Wibson, Flávia e Allan que me acompanham nessa jornada acadêmica, tornando-a mais leve e enriquecedora. À minha amiga Natalia Melo, sempre presente e me inspirando a ser uma excelente pesquisadora.

I would also like to express my gratitude to the LPL - Laboratoire de Physique de Lasers of the Université Sorbonne PARIS 13, which allowed the experimental part of this work to be carried out. A special thanks to the OCR team: Athanasios Laliotis, Isabelle Maurin, Hippolyte Mouhanna and Paolo Petri, who warmly welcomed me as part of their family. In particular, *Mon Ami* Esther Butery, who not only fully trusted my work but also supported me throughout the entire experimental journey of this project.

Sou também profundamente grata à CAPES e ao PPEngFIS pelo apoio financeiro essencial para a realização desta pesquisa, sem o qual este trabalho não teria sido possível. Por fim, mas não menos importante, agradeço aos meus orientadores, Sergio e Welliton, que sempre estiveram presentes de forma atenciosa e paciente. Eles me apoiaram e aconselharam em todas as decisões cruciais para a construção deste trabalho, e sua orientação foi fundamental para meu desenvolvimento acadêmico e pessoal.

A todos vocês, minha eterna gratidão.

"You can’t always get what you want, but if you try sometimes, you might find, you get what you need."

— The Rolling Stones, "You Can’t Always Get What You Want"

RESUMO

Nesse trabalho estudamos a propagação da luz em estruturas fotônicas induzidas por luz em um meio do tipo Kerr. Começa-se com uma revisão das equações de Maxwell, em seguida é abordado a equação de Helmholtz, a interação átomo-campo descrita pelas equações de Bloch e o sistema de dois níveis atomicos. Em seguida, é explorada a propagação de feixes de luz em meios não lineares utilizando o método de propagação de feixes por passos divididos (SSBPM), com foco em meios tipo Kerr. O estudo culmina na análise dos efeitos de autofocalização e autodesfocalização por meio de simulações em python usando o SSBPM. Na segunda parte, o trabalho se concentra na espectroscopia atômica de Rydberg em átomos de césio em células volumétricas e célula de espessura nanometrica. É apresentada uma descrição detalhada do sistema atômico e do aparato experimental utilizado. São discutidos os níveis atômicos do césio e o esquema espectroscópico empregado. O setup experimental é explicado, incluindo métodos para medição de espessura e aquisição de dados com escala de frequência. O estudo experimental tem foco na investigação da redistribuição de velocidade em átomos excitados de césio por meio de colisões e interações com átomos de Rydberg dentro de células nanométricas. Resultados obtidos tanto em células volumétricas quanto em células finas são apresentados, destacando variações na potência de bombeamento, densidade e frequência. Este trabalho integra estudos teóricos sobre a propagação da luz em estruturas fotônicas com investigações experimentais em espectroscopia atômica, demonstrando uma exploração abrangente de fenômenos ópticos e atômicos.

Palavras-chaves: Propagação da luz; meio tipo kerr; espectroscopia de Rydberg; redistribuição de velocidade; átomos de césio.

ABSTRACT

In this work we studied the propagation of light in photonic structures induced by light in a Kerr-type medium. It begins with a review of Maxwell's equations, follow on the Helmholtz equation, atom-field interaction described by Bloch equations, and the two-level atomic system. Next, the propagation of light beams in nonlinear media is explored using the Split Step Beam Propagation Method (SSBPM), with a particular emphasis on Kerr-type media. The study culminates in the analysis of self-focusing and self-defocusing effects through Python simulations using SSPBM.In the second part, the focus shifts to atomic Rydberg spectroscopy in cesium atoms within volumetric and nanometric-thin cells. A detailed description of the atomic system and experimental apparatus is provided. Cesium atomic levels and the employed spectroscopic scheme are discussed. The experimental setup is explained, including methods for thickness measurement and data acquisition with frequency scaling. The experimental study investigates velocity redistribution in excited cesium atoms through collisions and interactions with Rydberg atoms within nanometric cells. Results obtained from both volumetric and thin cells are presented, highlighting variations in pumping power, density, and frequency.This work integrates theoretical studies on light propagation in photonic structures with experimental investigations in atomic spectroscopy, demonstrating a comprehensive exploration of optical and atomic phenomena.

Keywords: Light propagation; kerr media; rydberg spectroscopy; velocity redistribution; cesium atoms.

LIST OF FIGURES

LIST OF TABLES

LIST OF EQUATIONS

TABLE OF CONTENTS

1 INTRODUCTION

The propagation of light in nonlinear media is a research field with applications in various areas of optics and photonics (Santos, 2009). One phenomenon we can mention is the interaction of light with Kerr-type media (MELO, Rosália Luana de Oliveira Silva et al, 2022) and (Gouveia, 2016), where the refractive index varies with the intensity of the incident light. This nonlinear behavior of the refractive index can lead to interesting effects such as the formation of optical solitons and is crucial for the development of photonic devices with controllable functionalities. In this first part of our work, we explore the principle of refractive index variation in Kerr-type media. When a light beam interacts with such a medium, intensity variations of the beam cause corresponding modulations in the refractive index of the medium (Lopes, 2012). This phenomenon, known as self-focusing, is a classic example of how light intensity can induce physical modifications in a nonlinear medium.

The study of light propagation in light-induced media has significant implications in various areas of optics and photonics. The ability to manipulate light trajectory and modify medium characteristics according to light intensity provides a basis for the creation of light modulation devices (Pedrola, 2015), optical routing (Maldonado; Junior, 1991), and even applications in quantum information processing (**??**). In this context, the use of atomic vapors as nonlinear media is particularly interesting.

An approach following this line of thought is the use of atomic vapors as nonlinear media for light propagation (Rodrigues et al., 2022). The nonlinear behavior of these vapors, such as those that exhibit Raman-Nath transitions (**??**), has been exploited to create light-induced refractive index modulations. Kash and Boyd (Paul et al., 2002) conducted pioneering studies on nonlinear refractive resonance in atomic vapors, highlighting the ability to control light propagation through interaction with these media. Additionally, Boyd and Gauthier (Boyd; Gauthier, 2010) also explored methods to control the speed of light pulses using nonlinear media, demonstrating the possibilities of precisely manipulating the properties of light in photonic systems.

In the second part of this work, we will explore spectroscopy in volumetric and nanometric cesium vapor cells, focusing on the study of the velocity redistribution of excited atoms. We will use the Rydberg absorption spectroscopy technique to observe with high resolution the excited states in the D1 line of cesium atoms, $6S_{1/2} \rightarrow 6P_{1/2}$, where through the D1 line we go to the Rydberg states $16S_{1/2}$ and $15D_{3/2}$.

In such atoms, the valence electron is mainly influenced by the positive charge of the ionic core rather than its structure. The excited states of these hydrogen-like atoms are called "Rydberg states"(NADA, a). Rydberg states are interesting for two reasons.

First, they are large and weakly bound, leading to peculiar properties. Second, much of their atomic structure and behavior in external fields can be understood based on direct extensions of hydrogenic theory.

The study of Rydberg atoms has seen significant experimental advances and renewed interest in recent years. This is because laser light provides a simple and precise method to produce relatively large populations in specific Rydberg states (Beterov et al., 2008). A central aspect of this investigation is the collisional broadening and shift of spectral lines, resulting from interactions between atoms and between atoms and the cell walls. These phenomena are crucial for understanding how collisions affect the velocity redistribution of excited atoms (Haverkort; Woerdman, 1990), influencing spectroscopic measurements.

Additionally, we will analyze the cesium atomic systems and levels, providing a detailed view of the electronic transitions leading to the formation of Rydberg states (NADA, a). Our focus will be on the effects of cesium pressure, which can modify spectral characteristics due to variations in the density of atoms in the vapor. To investigate the Rydberg states and their spectroscopic schemes, we will use an experimental setup designed to accommodate both volumetric and nanometric cell experiments. This setup, described in chapter 4, includes 894 nm and 512-513 nm lasers to excite the atoms, sensitive detectors to capture spectroscopic signals, and a data acquisition system to monitor and record variations in the frequencies and intensities of spectral lines.

Data will be acquired under different experimental conditions presented in chapter 6 of this work, where we have results varying the pump beam power, atomic density, and excitation frequency. In volumetric cells, we will study how these variables affect the velocity redistribution and the shape of spectral lines. In nanometric cells, we will investigate how cell thickness influences these same parameters, offering results on the behavior of cesium atoms in extremely small confinements. The expected results include the observation of significant changes in the velocity redistribution of excited atoms (Kolchenko et al., 1973), depending on cell thickness and experimental conditions. These results will contribute to a deeper understanding of the fundamental processes governing Rydberg spectroscopy in different environments and provide valuable data for future research and technological applications.

2 REVIEW OF MAXWELL'S EQUATIONS AND INTERACTION WITH MATERIAL MEDIA

In this chapter, we will explore Maxwell's equations in detail regarding their interaction with material media. We will focus on the dielectric and magnetic properties of materials, introducing the necessary concepts to address wave propagation based on Maxwell's equations formulated by James Clerk Maxwell in the 19th century. Additionally, we'll discuss a semi-classical model for atom-light interaction (Jackson, 2021).The nonlinear response to electromagnetic waves is characterized by the susceptibility (χ_n) of the medium, where "n"can take values such as 2 for second-order nonlinear effects (e.g., second harmonic generation (Kleinman, 1962) and 3 for third-order effects (e.g., four-wave mixing (Silva, 2023)), and so on.

2.1 INTRODUCTION TO MAXWELL'S EQUATIONS

To begin describing wave propagation, we need to discuss light propagation in a nonlinear medium. Electromagnetic phenomena are described by Maxwell's equations, which consist of four partial differential equations that underpin the fundamental principles of electromagnetism. In the absence of sources, free currents, and magnetization, these equations are given by:

$$\nabla \times \mathbf{E} = -\frac{\partial \mathbf{B}}{\partial t} \tag{1}$$

$$\nabla \times \mathbf{B} = \mu_0 \frac{\partial \mathbf{D}}{\partial t} \tag{2}$$

$$\nabla \cdot \mathbf{B} = 0 \tag{3}$$

$$\nabla \cdot \mathbf{D} = 0 \tag{4}$$

The interaction between electromagnetic fields and material media is crucial for a deeper understanding of electromagnetic phenomena. As these fields pass through materials, they influence the electrical and magnetic properties of the material. Dielectric materials are electrical insulators that, when subjected to electric fields, experience electrical polarization. The relationship between electric fields $(\mathbf{E})$ and electric displacement fields $(\mathbf{D})$ is expressed through the electric susceptibility ε:

$$\mathbf{D} = \varepsilon \mathbf{E} \tag{5}$$

Here, ε represents the electric permittivity of the medium. Magnetic materials respond to magnetic fields with magnetization, The relationship between magnetic fields ($\mathbf{B}$) and magnetic field intensity ($\mathbf{H}$) is influenced by the magnetic susceptibility χ_m:

$$\mathbf{B} = \mu\mathbf{H} \tag{6}$$

Here, μ denotes the magnetic permeability of the medium, and $\mu_r = 1 + \chi_m$ is the relative permeability of the material. The introduction of electric and magnetic susceptibilities modifies Maxwell's equations, turning them into powerful tools for understanding the interaction between electromagnetic fields and material media. These modifications reflect how materials respond to electric and magnetic fields, leading to electrical polarization and magnetization.

2.2 HELMHOTZ EQUATION

To derive the wave equation for the electric field, we take the curl of Equation 1. Using the fact that $\nabla \cdot \mathbf{E} = 0$, we obtain:

$$\nabla \times (\nabla \times \mathbf{E}) = -\nabla \times \frac{\partial \mathbf{B}}{\partial t} \tag{7}$$

Applying the vector identity $\nabla \times (\nabla \times \mathbf{E}) = \nabla(\nabla \cdot \mathbf{E}) - \nabla^2\mathbf{E}$ and knowing that $\nabla \cdot \mathbf{E} = 0$, we have:

$$-\nabla^2\mathbf{E} = -\frac{\partial}{\partial t}(\nabla \times \mathbf{B}) \tag{8}$$

Substituting Equation 2 into the above equation, we obtain:

$$-\nabla^2\mathbf{E} = -\mu_0\frac{\partial^2\mathbf{D}}{\partial t^2} \tag{9}$$

Since $\mathbf{D} = \varepsilon\mathbf{E}$, the equation becomes:

$$\nabla^2\mathbf{E} = \mu_0\varepsilon\frac{\partial^2\mathbf{E}}{\partial t^2} \tag{10}$$

Defining the speed of light in a vacuum as $c = \frac{1}{\sqrt{\mu_0\varepsilon}}$, we obtain the wave equation for the electric field:

$$\nabla^2\mathbf{E} - \frac{1}{c^2}\frac{\partial^2\mathbf{E}}{\partial t^2} = 0 \tag{11}$$

For the magnetic fields, a similar derivation shows that they also satisfy the same wave equation:

$$\nabla^2\mathbf{B} - \frac{1}{c^2}\frac{\partial^2\mathbf{B}}{\partial t^2} = 0 \tag{12}$$

Therefore, both the electric and magnetic fields satisfy the same wave equation, reflecting the intertwined nature of electromagnetic wave propagation in space. However, in terms of magnitude, the electric field dominates over the magnetic field, as $\mathbf{E} = c\mathbf{B}$. For this reason, it is common to represent a light field solely by $\mathbf{E}(\mathbf{r}, t)$.A conventional approach to analyzing light is to start with single-frequency (monochromatic) and linearly polarized wave fields. Thus, the electric field can be expressed as:

$$\mathbf{E}(\mathbf{r}, t) = \mathbf{E}_0 \cos(\omega t - \mathbf{k} \cdot \mathbf{r} + \phi) \tag{13}$$

In Equation 13, ω is the oscillation frequency, $\mathbf{E}_0$ is the amplitude of the electric field, $\mathbf{k}$ is the wave vector, and ϕ is the initial phase. Substituting Equation 13 into Equation 11, we obtain the equation describing the propagation of monochromatic light, known as the vector Helmholtz equation:

$$\nabla^2 \mathbf{E} + k^2 \mathbf{E} = 0 \tag{14}$$

where $k = \frac{\omega}{c}$ is the magnitude of the wave vector. For reasons that will become evident later, we consider linearly polarized light fields. This implies that we can represent the complex field from Equation 13 as follows:

$$\mathbf{E}(\mathbf{r}, t) = \mathbf{a} \cdot \text{Re}\{E(\mathbf{r})e^{-i\omega t}\} \tag{15}$$

Here, $\mathbf{a}$ is a constant vector defining the polarization direction of light, and $E(\mathbf{r})$ is the complex amplitude of the electric field. Therefore, despite the vector nature of light, we can treat it in a scalar manner. In general, $E(\mathbf{r})$ can be expressed in terms of two real functions: the amplitude $u(\mathbf{r})$ and the phase $\phi(\mathbf{r})$, as follows:

$$E(\mathbf{r}) = u(\mathbf{r})e^{i\phi(\mathbf{r})} \tag{16}$$

Here, $u(\mathbf{r})$ represents the real amplitude, and $\phi(\mathbf{r})$ represents the real phase angle of the complex amplitude $E(\mathbf{r})$. It's important to note that the magnitude of the electric field is given by $|E(\mathbf{r})| = u(\mathbf{r})$. The optical intensity $I(\mathbf{r}, t)$, defined as the optical power per unit area, is proportional to the temporal average of the square of the wave function:

$$I(\mathbf{r}, t) = \langle |E(\mathbf{r}, t)|^2 \rangle \propto |E(\mathbf{r})|^2 = u^2(\mathbf{r}) \tag{17}$$

This temporal average is calculated over a significantly longer time interval than the optical period but relatively short compared to other relevant timescales. For a monochromatic plane wave propagating in vacuum, it can be shown that the optical intensity $I(\mathbf{r}, t)$ is related to the electric field as follows:

$$I(\mathbf{r}, t) = c\epsilon_0 E(\mathbf{r}, t)^2 \tag{18}$$

where c is the speed of light in vacuum and ϵ_0 is the vacuum permittivity. This relation holds for a plane wave in vacuum, where the temporal dependence of the electric field is sinusoidal. For the time-averaged optical intensity, considering the oscillatory nature of the electric field and assuming a monochromatic wave, we can express the intensity in terms of the complex amplitude of the electric field:

$$I(\mathbf{r}) = \frac{1}{2} c\epsilon_0 |E(\mathbf{r})|^2 \tag{19}$$

Here, the factor $\frac{1}{2}$ arises from the time averaging of the square of the sinusoidal electric field. This result shows that the optical intensity is proportional to the square of the electric field amplitude for a monochromatic plane wave in vacuum. Therefore, we recognize that the modulus of the complex amplitude is directly related to the optical intensity, a physically measurable quantity. Although the Helmholtz equation can be separated into 11 coordinate systems, separability into transverse and longitudinal parts is possible only in Cartesian, circular cylindrical, parabolic cylindrical, and elliptical cylindrical coordinates (Conway; Cohl, 2010). The variation of the envelope $U(\mathbf{r})$ and its derivative with respect to z must be smooth over the extent of a wavelength $\lambda = 2\pi/k$, allowing the slowly varying envelope approximation to hold. Thus, the paraxial Helmholtz equation can be written as:

$$\nabla_\perp^2 U + 2k \frac{\partial U}{\partial z}(i-1) = 0 \tag{20}$$

Here, $\nabla_\perp^2$ is the transverse Laplacian operator. Assuming a smooth variation of $U(\mathbf{r})$ with respect to z, over a distance $\Delta z = \lambda$, the variation $\Delta U(\mathbf{r})$ along z is much smaller compared to $U(\mathbf{r})$ itself, that is:

$$\frac{\partial U}{\partial z} \ll kU \tag{21}$$

and, consequently:

$$\frac{\partial^2 U}{\partial z^2} \ll k \frac{\partial U}{\partial z} \tag{22}$$

Thus, the second term in the original equation can be neglected, resulting in the correct paraxial Helmholtz equation:

$$\nabla_\perp^2 U - 2ik \frac{\partial U}{\partial z} = 0 \tag{23}$$

This equation is recognized as the paraxial Helmholtz equation. In the following sections, we will address the first four types of beams mentioned in this section. Solutions leading to Gaussian, Hermite-Gaussian, and Laguerre-Gaussian beams stem from this equation, while Bessel, elliptical, and parabolic beams are exact solutions of the full Helmholtz equation without the paraxial approximation.

2.3 ATOM-FIELD INTERACTION AND BLOCH EQUATIONS

Let's consider a two-level atom as shown in figure 1, where $|a\rangle$ is the ground state and $|b\rangle$ is the excited state, and ω_0 is the atomic transition frequency to the ground state to excited state, ω is the laser frequency,Δ is the detuning and Γ is the decay rate between levels. The dynamic behavior of the system is governed by the Hamiltonian H (Boyd; Gauthier, 2010), composed of an atomic part H_A and an interaction term V. For this system, we have:

Figure 1 – Two level system scheme

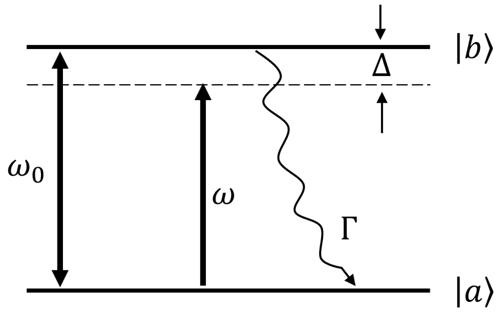

Soucer: The Author, 2024.

$$H_A = \hbar\omega_0 |b\rangle\langle b| \tag{24}$$

where $\hbar\omega_0$ represents the energy difference between states $|a\rangle$ and $|b\rangle$. The atom interacts with a monochromatic field of frequency ω_0, represented by:

$$\vec{E(t)} = \frac{1}{\sqrt{2}}(Ee^{i\omega t} + E^{*}e^{-i\omega t}) \tag{25}$$

The dipole moment $\vec{D}$ is an operator with odd parity, so for atomic states with well-defined parity, all diagonal elements are zero. Thus, we have:

$$\vec{D} = \vec{D}_{ab} |a\rangle \langle b| + \vec{D}_{ba} |b\rangle \langle a| \tag{26}$$

We must make a new approximation, because when considering the fields oscillating around the resonance frequency, we must disregard terms that appear in the Hamiltonian whose frequencies oscillate rapidly with a dependence given by $\pm(\omega + \omega_0)$ and keep only the terms that oscillate slowly $\pm(\omega - \omega_0)$. This approximation is known as the rotating wave approximation (RWA). Therefore the total Hamiltonian for this system will be given by:

$$H_{total} = \hbar\omega_0 |b\rangle \langle b| + \hbar\Omega |a\rangle \langle b| e^{i\omega t} + \hbar\Omega^{*} |b\rangle \langle a| e^{-i\omega t} \tag{27}$$

Where $\Omega = -\vec{D_{ab}}\vec{E}/2\hbar$ is called the Rabi frequency. Using the Liouville equation and considering a closed system, that is, the population is conserved, we can write the Bloch equations for the populations (ρ_{ii}) and coherences (ρ_{ij}).

$$\dot{\rho}_{aa} = -i\Omega\rho_{ab}e^{i\omega t} + i\Omega^{*}\rho_{ba}e^{-i\omega t} + \Gamma\rho_{bb} \tag{28}$$

$$\dot{\rho}_{bb} = -i\Omega^* \rho_{ab} e^{-i\omega t} + i\Omega \rho_{ba} e^{i\omega t} - \Gamma \rho_{bb} \tag{29}$$

$$\dot{\rho}_{ab} = i\omega_0 \rho_{ab} + i\Omega(\rho_{aa} - \rho_{bb}) e^{i\omega t} - \frac{\Gamma}{2}\rho_{ab} \tag{30}$$

$$\dot{\rho}_{ab} = -i\omega_0 \rho_{ba} + i\Omega(\rho_{aa} - \rho_{bb}) e^{-i\omega t} - \frac{\Gamma}{2}\rho_{ba} \tag{31}$$

Where Γ is the natural width of the excited state. Now, we introduce new variables called slow variables, we can rewrite this set of equations. So it follows:

$$\rho_{ii} = \sigma ii \tag{32}$$

$$\rho_{ab} = \sigma ab e^{i\omega t} \tag{33}$$

$$\rho_{ba} = \sigma ba e^{-i\omega t} \tag{34}$$

Leads to the following equations:

$$\dot{\sigma}_{aa} = -\Omega \sigma_{ba} + i\Omega^* \sigma_{ab} + \Gamma \sigma_{bb} \tag{35}$$

$$\dot{\sigma}_{bb} = -\Omega \sigma_{ab} + i\Omega^* \sigma_{ba} - \Gamma \sigma_{bb} \tag{36}$$

$$\dot{\sigma}_{ab} = i\Delta \sigma_{ab} + i\Omega(\sigma_{aa} - \sigma_{bb}) - \frac{\Gamma}{2}\sigma_{ab} \tag{37}$$

$$\dot{\sigma}_{ba} = -i\Delta \sigma_{ba} - i\Omega(\sigma_{aa} - \sigma_{bb}) - \frac{\Gamma}{2}\sigma_{ba} \tag{38}$$

Where $\Delta = \omega_0 - \omega$ represents the detuning of the atomic resonance frequency. Under normal conditions, when a resonant field interacts with an atomic system we have a strong absorption and scattering. Due to the interaction of the medium with a field a polarization arises, this polarization here is introduced as the complex amplitude P of the polarization through the relation:

$$P(t) = Ntr(\vec{D}\rho) = ND(\sigma_{ab} e^{i\omega t} + \sigma_{ba} e^{-i\omega t}) \tag{39}$$

Where N is the density of atoms. In most experiments, we are interested in calculating the absorption or refractive index of the atomic medium; these quantities are related to the average dissipated power. Therefore, the component that is in phase with the field does not dissipate energy, and consequently, the component responsible for absorption is the one that is in quadrature with the field. Therefore, absorption will be proportional to dispersion. To solve this system, and later other more complex ones, we must look for solutions in the steady state, that is, $\sigma_{ij} = 0$. So, after some calculations, we find the coherence σ_{ab} as:

$$\sigma_{ab} = \frac{\Omega(\Delta - i\Gamma/2)}{\Delta^2 + \Gamma^2/4 + 2|\Omega|^2} \tag{40}$$

Within Polarization we can introduce a variable called susceptibility of the medium χ, as the constant of proportionality relating P and E according to:

$$P = \varepsilon_0 \chi \cdot E(t) \tag{41}$$

Therefore, we find it that susceptibility is given by:

$$\chi = \frac{2ND}{\epsilon_0 E}\sigma_{ba} \tag{42}$$

The equation X can be rewritten as:

$$\chi = \chi^I + \chi^{II} \tag{43}$$

Where χ^I is associated with the real part of 42 and χ^{II} with the imaginary part of 42. In this way, with equation 42 we can find the absorption coefficient, because it is given by the real part of equation 42, as shown in equation 44 below:

$$\alpha = \frac{2\omega}{c}\Im(n) = \frac{2\omega}{c}\Im(1+\chi)^{\frac{1}{2}} \tag{44}$$

The complex index of refraction in the medium is $n = (1+\chi)^{1/2}$ which for $\chi << 1$, and knowing $k_0 = \frac{\omega}{c}$, we can find the absorption coefficient “α”. We can therefore write:

$$\alpha = k_0\Im(\chi) \tag{45}$$

On the other hand, the real part of susceptibility gives us the dispersion of the system:

$$n = 1 + \frac{1}{2}\Re(\chi) \tag{46}$$

Figure 2 shows the dispersion and absorption in function of the frequency ω.

Figure 2 – Dependence of (a) the absorption coefficient and (b) the index of refraction with the frequency ω in arbitrary units.

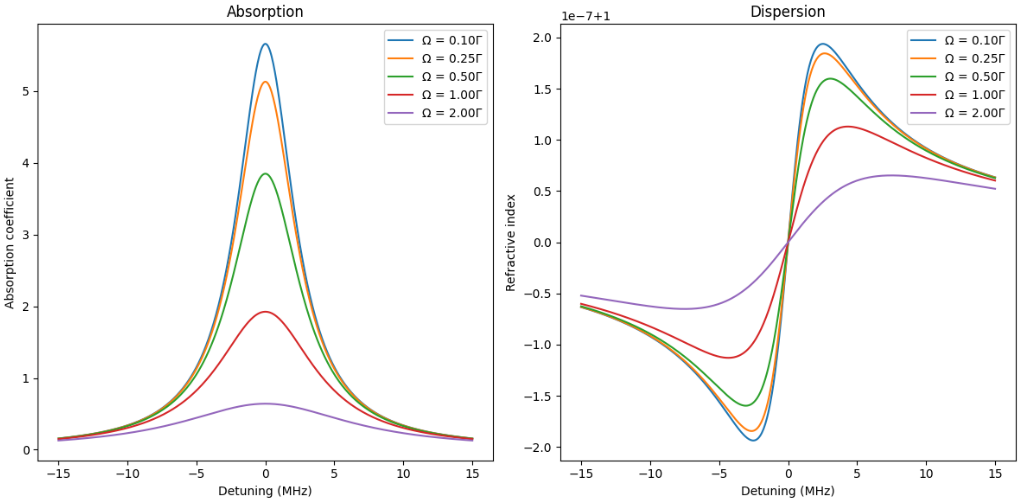

Soucer: The Author, 2024.

3 PROPAGATION OF LIGHT BEAMS IN NONLINEAR MEDIA

Previously, the propagation equation for the electric field and for the magnetic field was presented. However, in the previous chapter, only propagation in homogeneous media was considered. To work with the propagation of light in nonlinear media, we will need to consider instead of the electric field E, we will consider a generic wave function ψ, and with some modifications and calculations presented in (Poon; Kim, 2006) we arrive at the Nonlinear Schrödinger Equation (NLSE) (Fibich, 2015), which describes the evolution of the complex envelope $\phi(x, y, z)$ of a beam propagating in the z direction. The NLSE is a partial differential equation that incorporates diffraction and phase modulation effects due to variations in the refractive index within the medium.

$$\frac{\partial \phi}{\partial z} = \frac{1}{2jk_0}\nabla_t^2\phi - j\Delta n k_0 \phi \tag{47}$$

Here, k_0 represents the wave number, ∇_t^2 is the Laplacian operator in the transverse plane, j is the imaginare unit, ϕ represents the electric field of the beam and Δn denotes the variation of the refractive index, after all, we are considering a non-linear medium, this non-linearity will be related to a variation in the refractive index.

3.1 SPLIT STEP BEAM PROPAGATION METHOD

The Split Step Beam Propagation Method (SSBPM) is widely used in optics to study the propagation of light beams in nonlinear medias. It combines the resolution of linear and nonlinear effects alternately, simplifying the numerical integration process by dividing the wave evolution into small steps along the propagation path (Poon; Kim, 2006). To understand this method, we can introduce the operators S and D into the paraxial propagation equation:

$$\frac{\partial \phi}{\partial z} = \frac{1}{2jk}\nabla_t^2\phi - j\delta n k_0 \phi_e \tag{48}$$

which becomes:

$$\frac{\delta \phi}{\delta z} = (\hat{D} + \hat{S})\phi \tag{49}$$

The diffraction operator D accounts for diffraction effects and is expressed in terms of the Laplacian operator:

$$\hat{D} = -ik_0\nabla^2 \tag{50}$$

The space-dependent or inhomogeneous operator $\hat{S}$ represents phase changes due to variations in the refractive index within the medium and can take various forms depending on the specific refractive index distribution:

$$\hat{S} = -j\Delta n k \tag{51}$$

The SSBPM accurately models beam propagation by considering diffraction, dispersion, and nonlinearity. In the first step, the wave function ϕ is propagated considering only the linear terms of the equation, which usually involve scattering or diffraction. This is done through the Fourier transform, which allows to treat diffraction efficiently. In the second step, the nonlinear effect (usually dependent on the beam intensity) is considered, while maintaining the wave function ψ in the original space. This is done by multiplying by the corresponding nonlinear factor. The algorithm for a single step in Δz can be written as:

$$\begin{aligned}\psi(x,y,z+\Delta z) &= \exp(\vec{S}\Delta z)\exp(\vec{D}\Delta z)\psi(x,y,z) = \\ &= \exp\left(-j\Delta_n k_0 \Delta z\right) F^{-1}\ \exp\left(\frac{j(k_x^2+k_y^2)\Delta z}{2k_0}\right) F[\psi(x,y,z)]\end{aligned} \tag{52}$$

The SSBPM repeats this process until the field has traveled the desired distance. Figure 3 illustrates the popagation of the light beam along small distances Δz. For each Δz step, the method is applied over and over again until the distance is reached.

Figure 3 – Transverse profile of a Gaussian beam over small propagation distances Δz.

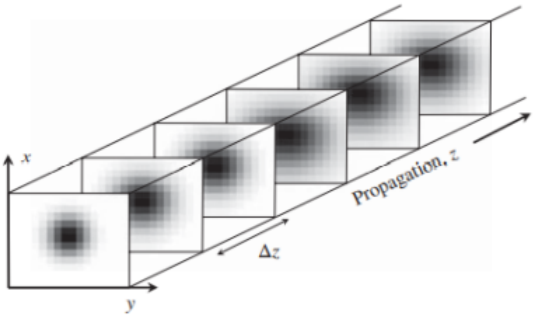

Soucer: Pedrola, 2015.

A schematic flow diagram of the SSBPM in its simplest form is shown in Figure 4, which illustrates a recursive loop iterated until the final distance is reached.

Figure 4 – Flow diagram for the beam propagation method.

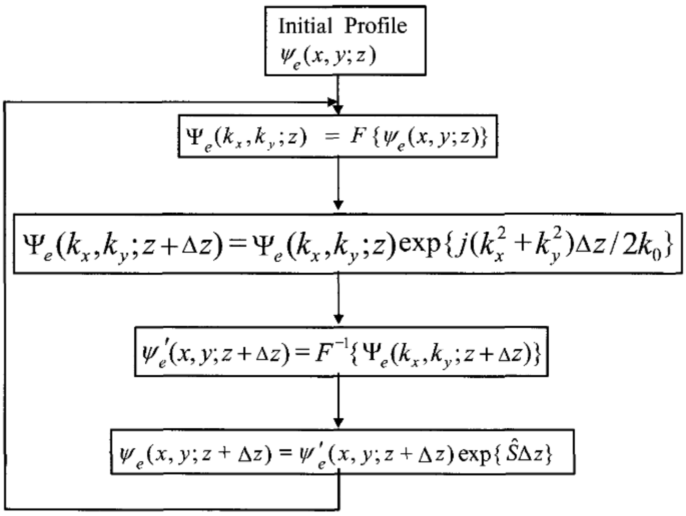

Soucer: Poon; kim, 2015.

3.2 KERR MEDIA

In the previous section, we presented the equation describing the SSBPM. However, we can treat diffraction and the effects of inhomogeneity separately using the SSBPM. Specifically, we have two independent equations represented by Equation 50 and Equation 51. These equations provide solutions for Fresnel diffraction and phase modulation independently. The solution to Equation 51 corresponds to phase modulation, as evident from the expression $\psi(x,y,z) = \exp(-j\Delta n k_0 z)$. When we talk about a non-linear medium, such as the Kerr type medium, we can introduce the nonlinear operator $\hat{N}$, which describes nonlinear effects in the propagating beam. The general equation for propagation in a nonlinear medium can be written as:

$$\frac{\partial \psi}{\partial z} = \hat{N}\psi \tag{53}$$

The expression for the operator N in a Kerr medium can be written as:

$$\hat{N} = -j\frac{n_{2E}}{n_0}k_0||^2 \tag{54}$$

Here, n_{2E} is the nonlinear susceptibility of the medium, n_0 is the refractive index of the medium in the absence of the light field, and k_0 is the wave number. The equation for propagation in a nonlinear medium is simply found by constructing an equation such that the appropriate operators on the right-hand side of equation 50 and 54:

$$\frac{\delta \psi}{\delta z} = (\hat{D} + \hat{N})\psi \tag{55}$$

In this section, we discuss an important nonlinear effect called the Kerr effect and demonstrate the use of SSBPM to solve this type of problem. The Kerr effect can be described by the following nonlinear dependence of the refractive index on the electric field of the light beam:

$$n = n_0 + n_{2E}|\psi|^2 \tag{56}$$

where $n_{2E}|\psi|^2$ is the nonlinear variation of the index, n_{2E} here is the kerr constant and has a unit of (m/V²). The medium can produce such an effect is called the kerr medium (Smith; Ashkin; Tomlinson, 1981). We will do a derivation of the $\hat{N}$ operator to find the expression:

$$\hat{N} = -j\Delta n k_0 = -j\frac{n^2 E}{n_0^2}k_0|\phi_e|^2 \tag{57}$$

and substituting the equation 57 in the equation 55, we obtain the NLSE for the Kerr-type medium:

$$\frac{\partial \psi_e}{\partial z} = \frac{1}{2ik_0}\nabla_t^2\psi_e - j\frac{n^2 E}{n_0^2 k_0}|\psi_e|^2\psi_e \tag{58}$$

We cannot solve the equation 58 using the Fourier transform techniques, because of the non linear term on the right-side of the equation. However, analytical solutions do exist in one transverse dimension, including a well-known stable solution called spatial soliton (Chen; Segev; Christodoulides, 2012). Solitons have a special property that they can propagate without changing their shape.

In the context of intense light beams in nonlinear media, solitons play a crucial role in the phenomenon of self-trapping. When $k < 0$ and $n_2 > 0$, solitons can maintain their shape as they propagate, balancing the effects of propagation due to diffraction and Kerr nonlinearity. Speaking specifically about a Kerr-type medium, it's essential to discuss autofocusing and self-defocusing (Liu et al., 2024).

We can understand this phenomenon using Huygens' principle, which states that each point on a wavefront acts as an independent source of secondary waves, all in phase with each other. Considering a medium with a positive nonlinear refractive index ($n_2 > 0$), the beam profile induces a radial distribution of refractive indices within the medium. This distribution is higher at the center and decreases toward the edges. As a result, the central region of the beam experiences a delay, leading to self-convergence. On the other hand, in a medium with $n_2 < 0$, the refractive index is lower at the center and higher toward the edges, causing the beam to experience a delay at the edges and, consequently, diverge. Figure 5 illustrates both of these effects.

To illustrate this principle, let us consider an incident laser beam with a Gaussian distribution, as described by the following equation:

$$\psi_a(x,y) = \psi_0 e^{-\frac{x^2+y^2}{\omega_0^2}} \tag{59}$$

Figure 5 – Auto-focus and auto-defocus effects.

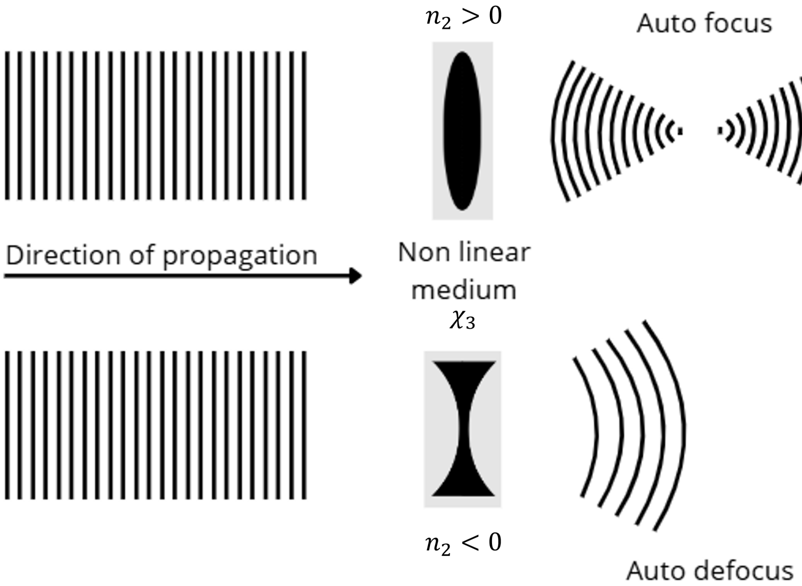

Soucer: Boni; Zílio, 2000.

Where ω_0 is the width of the Gaussian beam at the focal plane or at the point of least divergence of the beam. For $N_{2E} > 0$, from Equation 56, we have:

$$n = n_0 + n_{2E}|\psi_0|^2 \exp\left[-\frac{2(x^2+y^2)}{\omega_0^2}\right] \tag{60}$$

Which clearly means that intensity distribution creats a refractive index profile within the beam having a maximum value on the center and gradually deacreasing away from the center. Expanding the exponent and retaining the first two terms, Equation 60 becomes:

$$n(x,y) = (n_0 + n_{2E}\psi_0^2) - n_{2E}\psi_0^2 2(x^2+y^2)/\omega_0^2 \approx n_0 - \frac{2n_{2E}\psi_0^2}{w_0^2}(x^2+y^2) \tag{61}$$

Now we want to square $n(x,y)$, resulting in:

$$n^2(x,y) \approx n_0^2 - \frac{4n_0 n_{2E}\psi_0^2}{\omega_0^2}(x^2+y^2) \tag{62}$$

This Kerr-induced effect can be compared with the quadratic medium given by:

$$n^2(x,y) = n_0^2 + n_2(x^2+y^2) \tag{63}$$

By comparing Equations 62 and 63, we can identify n_2. Note that the quadratic medium exhibits periodic focusing properties with a modulation period given by:

$$z_m = \frac{\pi n_0}{\sqrt{n_2}} \tag{64}$$

However, Equation 62 implies that the value of n_2 is given by $\frac{4n_0 n_2 e^2 \psi_e}{\omega_0}$. Therefore, we can predict that the Kerr medium will have a focusing length approximately given by:

$$f_{NL} = \frac{z_m}{2} \approx \frac{\pi n_0}{2\sqrt{n_2}} = \frac{\pi}{4}\sqrt{\frac{n_0 u_0}{n_2 E \psi_o}} \tag{65}$$

We can consider that the Gaussian beam focusing produces converging rays with a convergence angle θ_{NL} given by:

$$\theta_{NL} \approx \frac{u_0}{f_{NL}} = \frac{4}{\pi}\sqrt{\frac{n_{2,i}}{n_0}}\psi_0 \tag{66}$$

However, in the absence of any nonlinear effects, the optical beam will spread due to diffraction and the propagation angle of a Gaussian beam. The propagation angle in the medium with an index is then given by:

$$\theta_{sp} = \frac{\lambda_0}{\pi \omega_0 n_0} \tag{67}$$

Therefore, the fact that these two angles are related leads us to expect that self-focusing can compete with diffraction. When $\theta_{NL} = \theta_{sp}$, the effects of self-focusing and diffraction cancel out, and the beam propagates without any focusing or defocusing. The power density equation for a plane wave with amplitude E_o immediately gives the power density for a Gaussian beam propagating along the z direction:

$$(S) = \frac{|\psi_0|^2}{2\eta} \exp\left(-\frac{2(x^2 + y2)}{\omega_0 2}\right) a_z \tag{68}$$

For a Gaussian profile, Equation 68 can be simplified as follows:

$$(S) = \frac{|\psi_0|^2}{2\eta} \exp\left[-\frac{2r^2}{\omega_0^2}\right] a_z \tag{69}$$

where η represents the characteristic impedance of the medium with refractive index n_0. Therefore, the total power of the beam is given by:

$$P_0 = \int_0^\infty (S) \cdot 2\pi r \, dr \, dz \tag{70}$$

Equation 70 defines the total power of the beam:

$$P_0 = \frac{n_0 \varepsilon_0 c \pi |\Psi_0|^2 \omega_0^2}{4} \tag{71}$$

To find the critical power, we calculate the required field amplitude by equating $\theta_{NL} = \theta_{sp}$, i.e., setting Equations 66 and 67 equal to each other:

$$\psi_{0,\alpha T} = \frac{\lambda_0}{4 w_0 \sqrt{n_0 n_{2E}}} \tag{72}$$

Substituting Equation 72 into Equation 71, we obtain the critical power: 5

$$P_{cr} = \frac{\pi c \epsilon_0 \lambda_0^2}{64 n_2 E} \tag{73}$$

Therefore, when $P_0 = P_{cr}$, self-trapping occurs. For $P_0 < P_{cr}$, diffraction dominates, and the beam diverges, resulting in the effect known as self-defocusing. When $P_0 > P_{cr}$, nonlinear effects prevail, and the beam self-focuses, potentially becoming abnormally large in the focused region and causing material breakdown.We conducted Python simulations using the Split Step Beam Propagation Method (SSBPM) to model an atomic vapor medium exhibiting Kerr-like behavior. In these simulations, we can define the refractive index values and beam powers. The figure 6illustrates the effect of self-focusing and self-defocusing.

These images are from our simulation using SSBPM in python for the Kerr media, where (a) is the initial field profile, and after propagation we can get the autofocus effect (b) for positive n_2 values and (c) with the auto defocus for negative n_2 values. For $n_2 > 0$, the refractive index is higher where the beam amplitude is greater. This behavior leads to the central part of the beam having a higher refractive index than the outer region, influencing the light rays' behavior within the beam.

Figure 6 – (a) is the initial field profile, and after propagation we can get the autofocus effect (b) for positive n_2 values and (c) with the auto defocus for negative n_2 values.

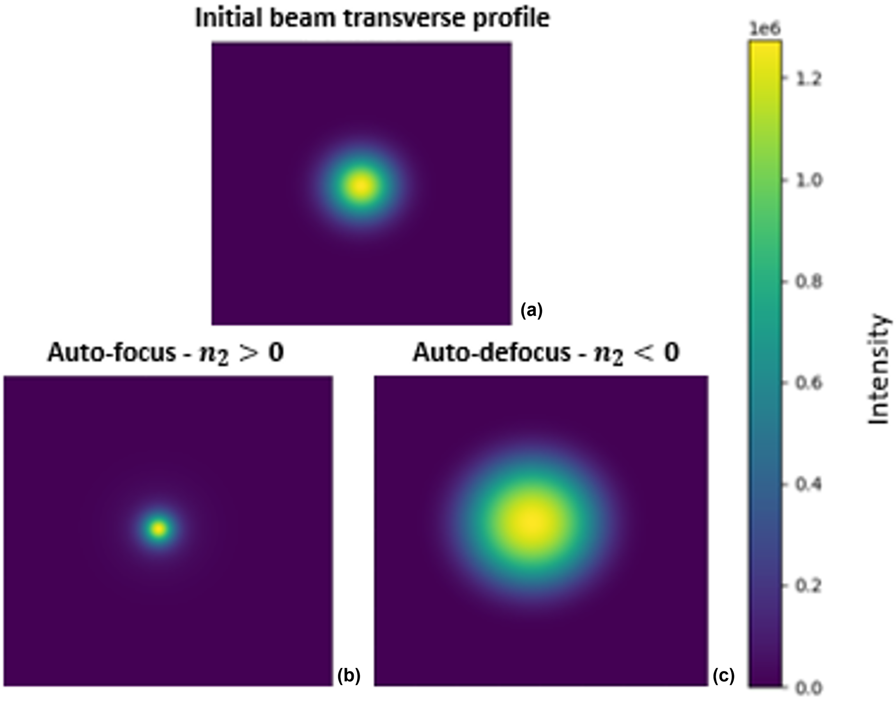

Source: The Author, 2024.

Light rays at the beam's edge, where the refractive index is lower, bend toward the beam's center due to the Kerr effect, which is described by the second term on the right-hand side of the NLSE. This nonlinear-induced inhomogeneity allows the beam to maintain its shape by balancing the effects of diffraction and Kerr nonlinearity. Sech beams belong to a family of "nonspreading"or "diffraction-free"beams in a nonlinear cubic medium, as they retain their shape during propagation. In one transverse dimension, when n_2 is positive and the nonlinear focusing slightly exceeds the diffraction effect, a periodic phenomenon known as "periodic self-focusing"can occur. Through the Kerr effect, light rays from the beam's edge bend toward the center, leading to the nonlinear optical phenomenon of self-focusing (or, in some cases, self-defocusing).

3.3 PHOTONIC CRYSTALS

Crystals are materials that exhibit periodicity in their composition, which can extend in one, two, or three dimensions. The repeating pattern of the crystal's constituents in space is referred to as the crystal lattice. This lattice structure was first observed by mineralogists in the late 19th century and later confirmed by the phenomenon of X-ray diffraction when X-rays are scattered by the crystals (**??**).

It was also discovered that electrons propagate through crystals as waves, and depending on their energy, certain electron waves are unable to propagate, resulting in the formation of an energy gap known as the forbidden band (John et al., 2008). The study of crystals gained even more importance with the formulation of the diffraction theory by physicist Max Von Laue, which explained how X-rays diffract when interacting with a crystalline material (Eckert, 2012).

Shortly after, William Henry Bragg (1862-1942) and his son William Lawrence Bragg (1890-1971) formulated a mathematical relationship, known as **Bragg's law**, which establishes the condition for constructive interference of waves scattered by the points of a crystal lattice (Bragg; Bragg, 1913). This law is fundamental for studying crystal structures through X-ray diffraction, and its mathematical form is:

$$2d\sin(\theta) = n\lambda \tag{74}$$

where d is the distance between lattice planes, θ is the angle of the incident ray (as shown in Figure 7), and n is an integer representing the number of wavelengths λ. Figure 7 illustrates the case where Bragg's law applies. The path difference between rays reflected from adjacent planes is $2d\sin(\theta)$, leading to constructive interference under specific conditions.

Bragg's law is valid only for wavelengths $\lambda < 2d$. Although the reflections from individual planes are specular, only at certain angles θ do the reflections from all planes add up in phase, resulting in an intense diffracted beam. This diffraction phenomenon is a direct consequence of the periodic arrangement of the crystal lattice, which also governs the propagation of electrons. The crystal's periodic potential restricts the movement of electrons in certain energy ranges, leading to the formation of energy band gaps. The geometry of the lattice and the crystal's composition thus determine its electrical conduction properties.

This concept of periodicity also applies to waves other than electrons. In the 1980s, researchers began to explore how materials with periodic structures on the scale of optical wavelengths could manipulate light in ways similar to how crystals influence electron waves. These materials are known as **photonic crystals**, and they function by creating periodic variations in the refractive index of the material, analogous to the periodic potential in a solid-state crystal. Just as electronic band gaps prevent the

Figure 7 – Bragg's Law Illustration

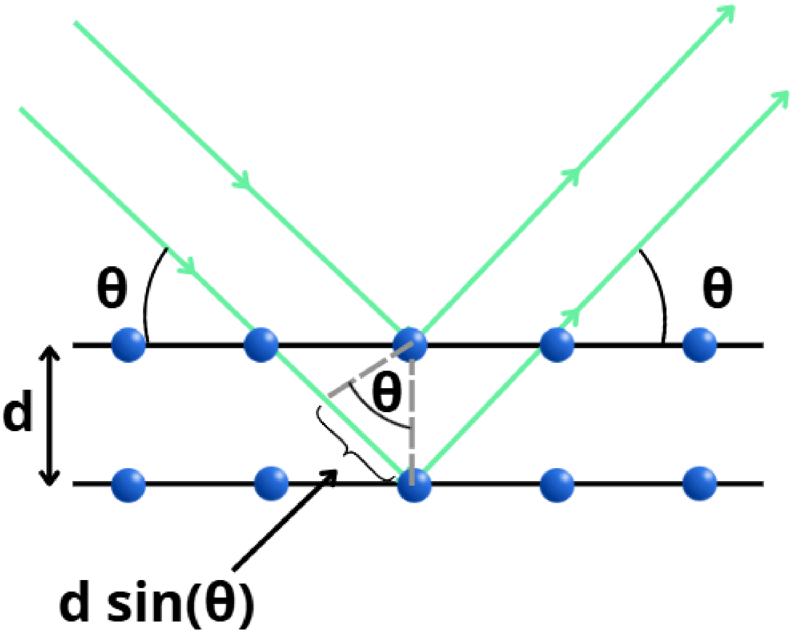

Source: The Author, 2024.

propagation of electrons at certain energies, photonic crystals can create photonic band gaps, where light of specific wavelengths is prohibited from propagating through the material.

Photonic crystals are not only artificially engineered but also exist in nature. For instance, the vibrant colors of certain butterflies and insects result from natural photonic structures in their wings, which act as multilayered, stratified media. These natural photonic crystals were studied using electron microscopy by Pete Vukusic and Ian Hooper, revealing intricate nanometric structures responsible for the optical effects (Vukusic; Hooper, 2005). Similar structures are found in other biological systems, such as in birds and fish, highlighting the widespread occurrence of photonic crystals in nature (Preble; Lipson; Lipson, 2005), as illustrated in Figure 8.

In summary, photonic crystals offer a new way to control the flow of light, just as traditional crystals control electron motion. They are key components in the development of advanced optical devices, including filters, waveguides, and resonators, and hold the potential for numerous future applications in photonics.

These structures were initially proposed, under this name, by the works of (Yablonovitch, 1987) and (John, 1987), which led to a significant increase in the study of this type of material. However, the study of these structures began much earlier, more precisely in 1887, when (Rayleigh, 1887) observed the propagation of waves in periodic structures. It was only in 1972 that significant progress was made in the study of these

Figure 8 – Examples of Photonic Crystals Found in Nature

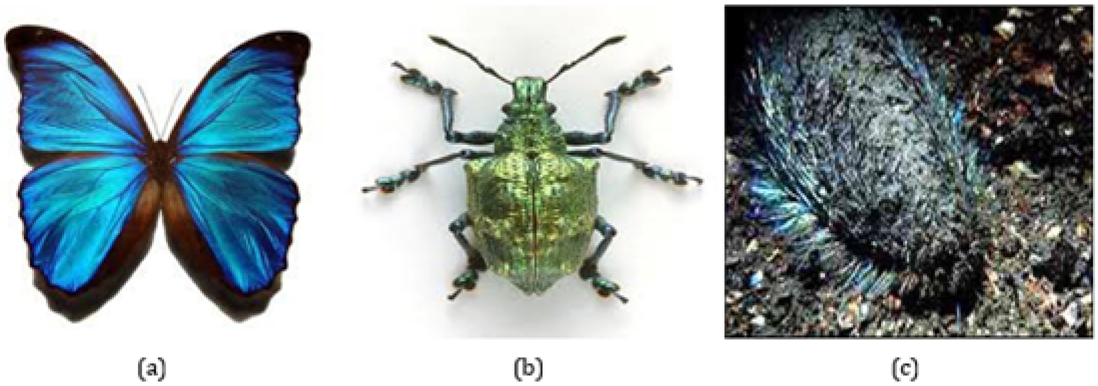

Source: Araújo, 2012.

structures, with the work of (Bykov, 1972), which raised the possibility of using periodic structures to control spontaneous emissions.

Photonic crystals represent a new class of optical media, composed of natural and artificial structures with periodic modulation of the refractive index. These optical media have peculiar properties that offer numerous technological applications. According to the number of axes along which photonic crystals have periodicity in their refractive indices, these materials can be divided into three types: one-dimensional, two-dimensional, and three-dimensional, as shown in Figure 9.

Figure 9 – Photonic crystal (a) one-dimensional, (b) two-dimensional, (c) three-dimensional.

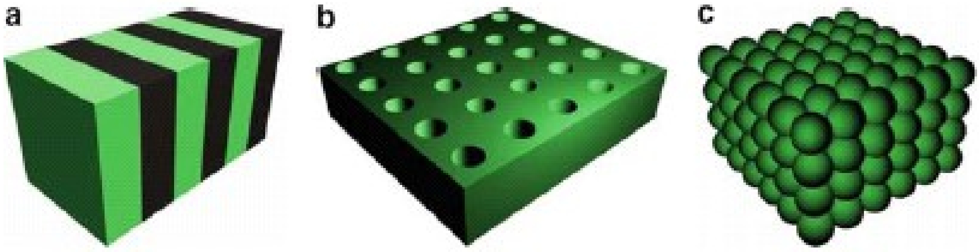

Source: Araújo, 2012.

One-dimensional periodic structures consist of stacks of identical parallel multilayer segments. These are often used as gratings that reflect optical waves incident at certain angles, or as filters that selectively reflect waves of specific frequencies. Two-dimensional periodic structures include sets of parallel rods, as well as sets of parallel cylindrical holes, such as those used to modify the characteristics of optical fibers known as hollow fibers. Three-dimensional periodic structures comprise arrays of cubes, spheres, or holes of various shapes, organized in lattice structures very similar to those found in natural crystals.

In one-dimensional photonic crystals, the electric permittivity is periodically modulated in only one direction, while in the other two directions of the structure it remains uniform. An example of this type of photonic crystal is the Bragg grating (Figure 10), which is widely used to modulate the refractive index along the length of an optical fiber (Ball; Morey, 1994). When light within the fiber interacts with the Bragg grating, part of the radiation is reflected and another part is transmitted.

Figure 10 – Opical fibre with a Bragg grating.

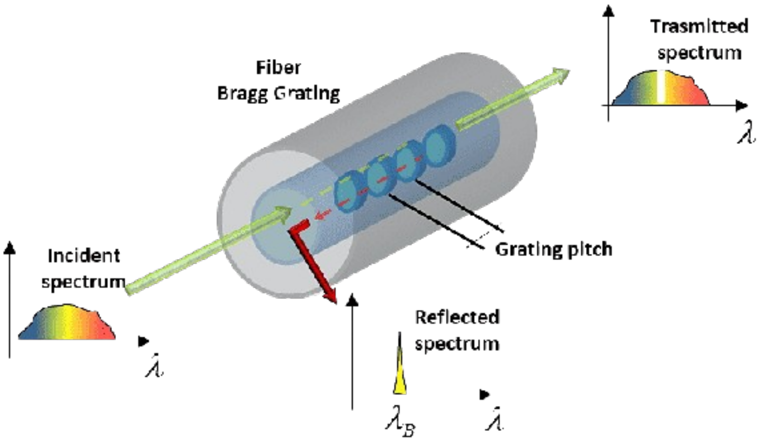

Source: Nannipieri et al, 2017.

Two-dimensional photonic crystals can exhibit a wide variety of configurations compared to one-dimensional ones, as they have periodicity of permittivity along two directions, while the third direction of the medium remains uniform. An example of this type of photonic crystal is porous silicon (Pacholski, 2013), with periodically organized pores, represented by a perforated silicon substrate. Another example is a system of periodically organized dielectric rods in the air. An example of a two-dimensional photonic crystals in nature is the pattern on butterfly wings and their rainbow effect are caused by the reflection of light on the two-dimensional microstructure of the wings.

Three-dimensional photonic structures have modulation of permittivity along all three directions. In these crystals, the number of possible configurations is greater than in the previous structures. Many scientific studies are dedicated to designing new geometric configurations to expand possible applications. The most well-known naturally formed three-dimensional photonic crystal is the precious stone opal (Rue et al., 2001). This stone has unique optical properties. When we rotate the opal in the presence of light, it displays a variety of colors. Due to this behavior, ancient peoples believed that the opal possessed magical powers.

However, it is known that all these peculiarities are caused by the microstructure of the opal, which is composed of a series of microspheres positioned at the vertices of a face-centered cubic lattice. The reflectance in this structure strongly depends on the angle of incidence of the radiation. The optical properties of photonic crystals are determined by the existence of periodic modulation of the permittivity or refractive index of the medium.

Therefore, the observed effects have a strong analogy with those of solid-state physics, that is, the periodically arranged photonic structure resembles that of atoms in a crystal lattice. This similarity makes it possible to use the properties and calculation methods applied in solid-state physics. Among the similarities between the physics of photonic crystals and solid-state physics, the following stand out:

- The periodic modulation of the refractive index in a photonic crystal forms a lattice similar to the atomic lattice in solid-state physics.
- The behavior of photons in photonic crystals is similar to the behavior of electron-hole pairs in an atomic lattice.
- The periodicity of both lattices causes the appearance of a gap in the band structure (band gaps), i.e., an energy interval inaccessible to the particle within the structure.
- From a theoretical point of view, determining the eigenfunctions in a photonic crystal is very similar to calculating the wave function of a particle in solid-state physics. This similarity is used to obtain the photonic band structure.

Despite the strong similarity, there are some essential differences. One of the main differences is the distribution of particle energy. Electrons follow the Fermi-Dirac distribution, while photons follow the Bose-Einstein distribution. Additionally, electrons are influenced by the intra-crystalline field, which must be considered in calculations. The form of this intra-crystalline field is unknown, so approximate methods such as the k-p method are used. Photons are not affected by the intra-crystalline field, which simplifies the calculation of the optical field distribution or photonic band structure.

The most important characteristic that determines the practical application of photonic crystals is the presence of the photonic band gap. This gap refers to an energy range or frequency interval forbidden for light propagation within the structure. When radiation with a frequency belonging to the forbidden interval of the structure is incident, it is completely reflected. However, if a defect is introduced into the periodic photonic structure, an effect similar to that observed in semiconductors with defects in their crystalline structure occurs. This means that new states appear within the forbidden region, with energies corresponding to the defect frequencies.

Thus, the radiation will propagate within the defect frequency, allowing its propagation in a previously forbidden region. When multiple defects are introduced into the structure, the radiation propagation is guided as in a waveguide. Here we propose the creation of a photonic crystal through simulation, where we will work with an atomic vapor medium, as described in Chapter 2. The idea is to explore the optical properties of this medium to develop a functional photonic crystal. To create the crystal, we will focus on controlling the refractive index of this atomic medium.

The refractive index is a crucial property that determines how light propagates through a material. In the case of an atomic vapor medium, we can adjust the refractive index through specific techniques, such as applying electric or magnetic fields, or manipulating the vapor density. This control capability allows us to create a periodic structure for the formation of a photonic crystal.

An electromagnetic-optical analysis is usually required to describe the optical properties of inhomogeneous media, such as multilayer and periodic media. For inhomogeneous dielectric media, as we know in chapter 3, the permittivity $\epsilon(r)$ varies spatially and the wave equation takes on the general forms 11. For a harmonic wave of angular frequency (ω), this leads to generalized Helmholtz equations 14. We can draw an analogy between an atomic vapor medium and a Kerr-type medium through the relationship between light intensity and refractive index variation. In a Kerr medium, the refractive index n is dependent on the intensity I of the light propagating through it, described by:

$$n = n_0 + n_2 I \tag{75}$$

where n_0 is the linear refractive index, and n_2 represents the nonlinear coefficient that quantifies the intensity-induced change in the refractive index. Similarly, in an atomic vapor medium, the refractive index can also be modified by controlling external parameters such as vapor density, external fields, or laser detuning. This behavior can be described by the following equation for the refractive index in an atomic vapor:

$$n = 1 + \frac{Nd^2}{2\hbar\varepsilon_0} \cdot \frac{\delta}{\Omega^2 + 2\delta^2 + \frac{\Gamma}{2}} \tag{76}$$

Here N is the atomic density, d is the dipole matrix element, δ represents the detuning from resonance, Ω is the Rabi frequency, and Γ is the linewidth of the atomic transition. By examining the intensity-dependent behavior, we can relate this expression to the Kerr effect. If we assume that the intensity of the incident field I is proportional to $|\psi_e|^2$, we can rewrite the refractive index in a form analogous to the Kerr medium, as:

$$n = n_0(\delta) + n_2 I \tag{77}$$

where $n_0(\delta)$ is the detuning-dependent refractive index, and n_2 represents the nonlinear component that varies with intensity. For further clarity, if we substitute the expression for n_2 from the atomic vapor equation, we obtain:

$$n = n_0(\delta) - \frac{Nd^2}{2\hbar\epsilon_0} \cdot \frac{\delta}{(2\delta^2 + \frac{\Gamma}{2})^2} \cdot \left(\frac{2d}{\hbar}\right)^2 \tag{78}$$

This final form highlights the dependence of the refractive index on both the atomic parameters (such as detuning δ) and the intensity of the field, demonstrating how atomic vapor media can be treated similarly to Kerr media in terms of intensity-driven refractive index modulation. Considering a standing wave within the medium, we create a periodic intensity pattern that can be used to induce a periodic pattern in the atomic vapor, similar to a Bragg grating. This periodic intensity pattern can be mathematically described by the equation:

$$I = 2I_0 \cos^2(kz) \tag{79}$$

where I_0 is the initial intensity and k is the wave number. The resulting periodic variation in intensity can modulate the refractive index of the medium, described by:

$$n = n_0 + 2n_1 n_2 \cos^2(kz) \tag{80}$$

where n_0 is the base refractive index and n_1 and n_2 are modulation coefficients. To better understand the behavior of the standing wave, we can consider the electric field E of the wave, which can be expressed as:

$$E(z,t) = E_0 \cos(kz - \omega t) \tag{81}$$

where E_0 is the amplitude of the electric field, ω is the angular frequency, and t is time. The intensity I is related to the square of the electric field:

$$I = \frac{1}{2}\epsilon c E_0^2 \cos^2(kz) \tag{82}$$

where ϵ is the permittivity of the medium and c is the speed of light in the medium. Photonic devices often comprise multiple layers of different materials arranged in a specific order to achieve desired optical properties. A multilayer medium can also be periodic, consisting of identical dielectric structures replicated in a one-dimensional, two-dimensional, or three-dimensional periodic arrangement.

These periodic structures can manipulate light in various ways, such as reflecting specific wavelengths, guiding light through waveguides, or creating photonic band gaps that prohibit the propagation of certain wavelengths. The reflection and transmission of light in such periodic structures can be analyzed using the transfer matrix method.

To analyze how an incident electromagnetic field interacts with a periodic structure, we apply the transfer matrix M to calculate the behavior of the light as it passes through each layer. For a single layer of thickness d and refractive index n, the transfer matrix is given by:

$$M = \begin{pmatrix} \cos(kd) & \frac{i}{n}\sin(kd) \\ in\sin(kd) & \cos(kd) \end{pmatrix} \tag{83}$$

where $k = \frac{2\pi}{\lambda}n$ is the wave number in the medium and λ is the wavelength of light.

To analyze the reflection and transmission of an incident field, we proceed as follows:

- 1. Incident Field: The incident electromagnetic wave can be represented as a combination of forward and backward traveling waves. At the boundary of the structure, we define the incoming and reflected fields in terms of their electric field amplitudes.

- 2. Propagation Through Layers: For multi-layered structures, we compute the overall transfer matrix by multiplying the individual matrices of each layer. This cumulative matrix relates the input and output fields after passing through the entire structure.

- 3. Reflection and Transmission: With the total transfer matrix, we can determine the reflection coefficient r and transmission coefficient t by solving the equations that describe the boundary conditions for the electric field at the first and last interfaces. These coefficients provide information on how much of the incident light is reflected or transmitted through the structure.

In practical applications, this method is utilized in devices such as distributed Bragg reflectors (DBRs), photonic crystals, and optical filters. For instance, DBRs reflect specific wavelengths of light by constructive interference due to alternating layers of different refractive indices. The transfer matrix method allows for precise calculations of the reflection and transmission spectra, which are crucial for designing efficient optical devices.

The transfer matrix method provides essential information about the interaction of light with periodic structures, enabling the development of devices that control light propagation, such as reflectors, filters, and waveguides.

The band structure of the photonic crystal is the characteristic that most reveals its properties. It is represented by a set of eigenstates or eigenfrequencies of an infinite periodic structure. The eigenfrequency is also known as the resonance frequency of the structure. Since the photonic crystal is an infinite periodic structure, a series of Fresnel reflections occur at the interfaces. The constructive and destructive interference of the waves results in the transmission or reflection of the radiation.

Each set of eigenstates corresponds to a specific value of the radiation wave vector. Regardless of the dimensionality of the photonic crystal, the band structure is represented by a two-dimensional graph. An example of a band structure for a one-dimensional photonic crystal is shown in Figure 11. The physical significance of the band

Figure 11 – Band structure of the one-dimensional photonic crystal.

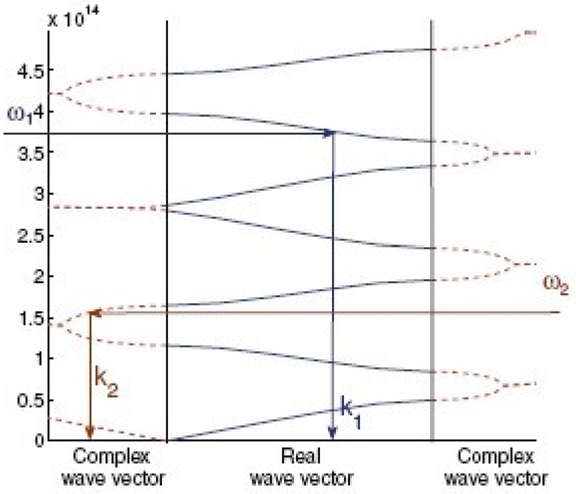

Source: Araújo, 2012.

structure is to relate the properties of the radiation to the characteristics of the optical medium through which it propagates. In Figure 2.11, the horizontal axis represents the radiation wave vector, while the vertical axis shows the resonance frequencies of the medium. Let's consider the case where radiation with frequency ω_1 is incident on the photonic crystal. After penetrating the structure, the radiation acquires a wave vector value allowed by the structure. This value can be easily determined from the band structure. Figure 11 shows that the wave vector with value k_1 corresponds to the radiation frequency ω_1. With this wave vector, the radiation propagates within the structure.

Now, we will analyze another case. If the radiation has a frequency ω_2, the corresponding wave vector does not fall within the range of real values; instead, it has a non-zero imaginary component. The imaginary part of the wave vector indicates either attenuation of the radiation or amplification in the case of material gain. In 11, k represents attenuation. Radiation with a frequency within the interval of k is either attenuated or amplified by the structure. However, since the radiation has a finite value, before undergoing reflection, it penetrates slightly into the structure.

These two cases contain basic principles of photonic band structure analysis, that is, the periodic medium propagates within the allowed frequency intervals and is prohibited in the intervals where purely imaginary wave vectors, known as photonic gaps, are present. If the radiation has a frequency belonging to the allowed interval, the photonic gaps are reflected. The forbidden frequency ranges are usually referred to as photonic gaps. If the radiation has an allowed frequency, it assumes the wave vector value that can be found from the band structure.

In Figure 12, we present three-dimensional photonic crystals. These crystals were generated through simulations conducted in Python, taking into account the periodicity and refractive indices of the atomic medium. In these simulations, we modeled the crystal structures with periodic functions, ensuring that the optical properties were correctly represented.

Figure 12 – Photonic crystals in 3 dimensions created in Python simulations

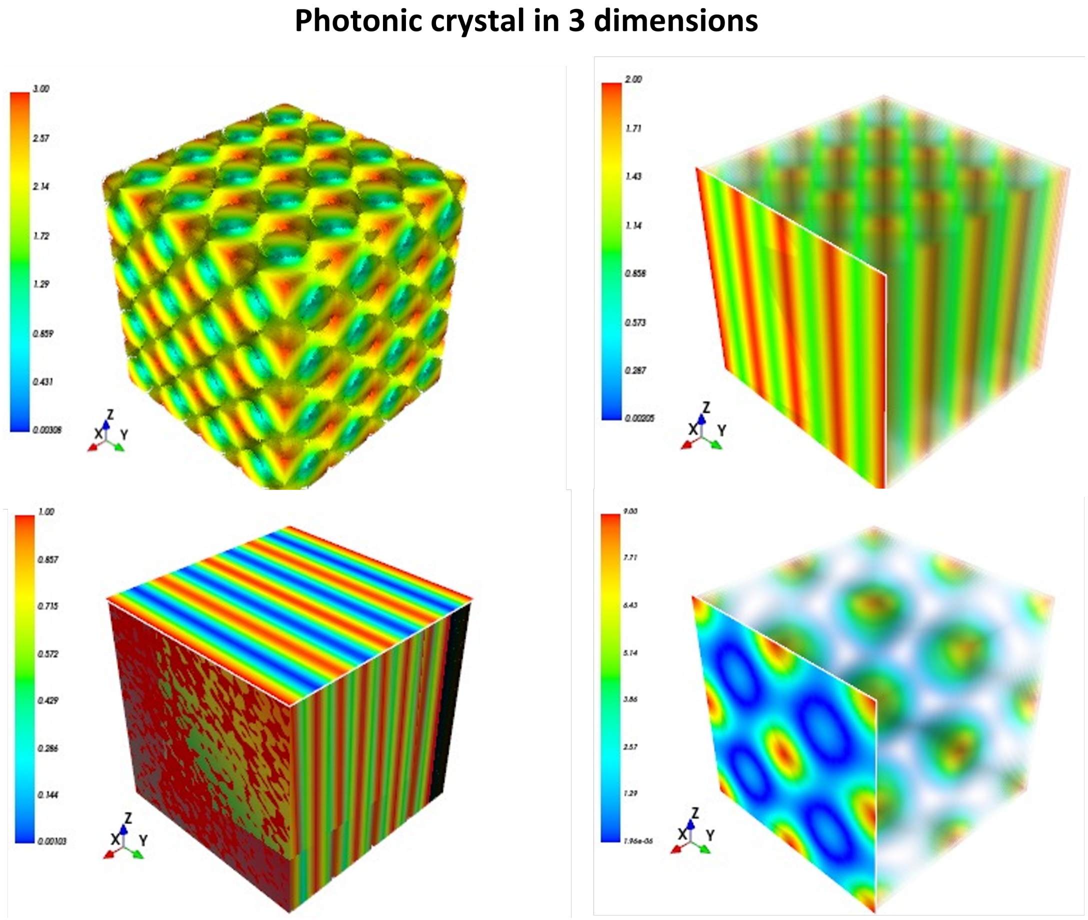

Source: The author, 2024.

For the simulation, we considered different parameters, such as the density of the atomic vapor and the application of external fields, which directly influence the refractive index of the medium. The periodicity of the structure was carefully adjusted to create the necessary conditions for the formation of forbidden bands (photonic gaps), which are essential for controlling the propagation of light through the crystal.

The simulation results showed that by adjusting the mentioned parameters, it is possible to obtain photonic crystals with desired optical properties, such as selective reflection and transmission of specific light frequencies through refractive index control. In Figure 12, the blue regions represent areas with a higher refractive index, while the red regions represent areas with a lower refractive index. These crystals have potential for various technological applications, including optical communication devices, sensors, and lasers.

Furthermore, the use of Python for the simulation allowed significant flexibility in modeling the crystals, enabling the exploration of different geometric configurations and materials. This paves the way for future research and the development of new types of photonic crystals with customized properties.

3.4 SIMULATIONS RESULTS

In the previous session, we explored the structure and dynamics of photonic crystals, highlighting the importance of photonic band gaps and the periodicity of the refractive index in controlling light propagation. Now, we will focus on how these concepts are implemented and visualized through simulations performed in Python. We conducted Python simulations aimed at replicating the formation of photonic crystals using an atomic vapor medium. To achieve this, we modeled the refractive index of the medium according to equations 76 and 77, which describe the dependence of the refractive index on the intensity of the incident electric field. The code was designed to generate a one-dimensional periodic structure, where the periodicity occurs in the refractive index, similar to the phenomenon observed in Bragg crystals, where a standing wave creates a periodic intensity pattern.

These periodic variations in the refractive index simulate the formation of a photonic crystal within the atomic vapor medium. As previously discussed, a photonic crystal can create a bandgap for certain light frequencies, preventing the propagation of radiation within these specific frequencies. In the code, this is represented by the periodic modulation of the refractive index, resulting in gaps in the simulated photonic band structure.The simulations demonstrate how light interacts with these structures, either being reflected or transmitted, depending on the radiation frequency and the geometry of the crystal structure. This is directly observed in the photonic band structure, where the relationship between the wavevector of the radiation and the resonant frequencies of the medium determines whether the light will be transmitted or blocked.

Through these simulations, it is possible to visualize the creation of photonic gaps and observe how the behavior of light is influenced by the periodicity of the medium. Additionally, the code allows for adjusting parameters, such as vapor density or the intensity of the applied field, to explore different configurations of photonic crystals and better understand how these factors affect the optical properties of the system. In Figure 13, we observe the distribution of the electric field intensity along the z axis. The graph reveals the formation of intensity peaks where peak (a) represents the reflected beam and peak (b) represents the transmitted light intensity, suggesting possible focusing and phase shift phenomena as the beam propagates through the grid. The formation of these peaks indicates regions where the electric field is amplified, which is related to the modulation of the refractive index of the medium.

Figure 13 – The distribution of the electric field intensity $||E||$ along the z-axis in arbitrary units, showing the spatial evolution of the Gaussian beam through the atomic vapor medium.

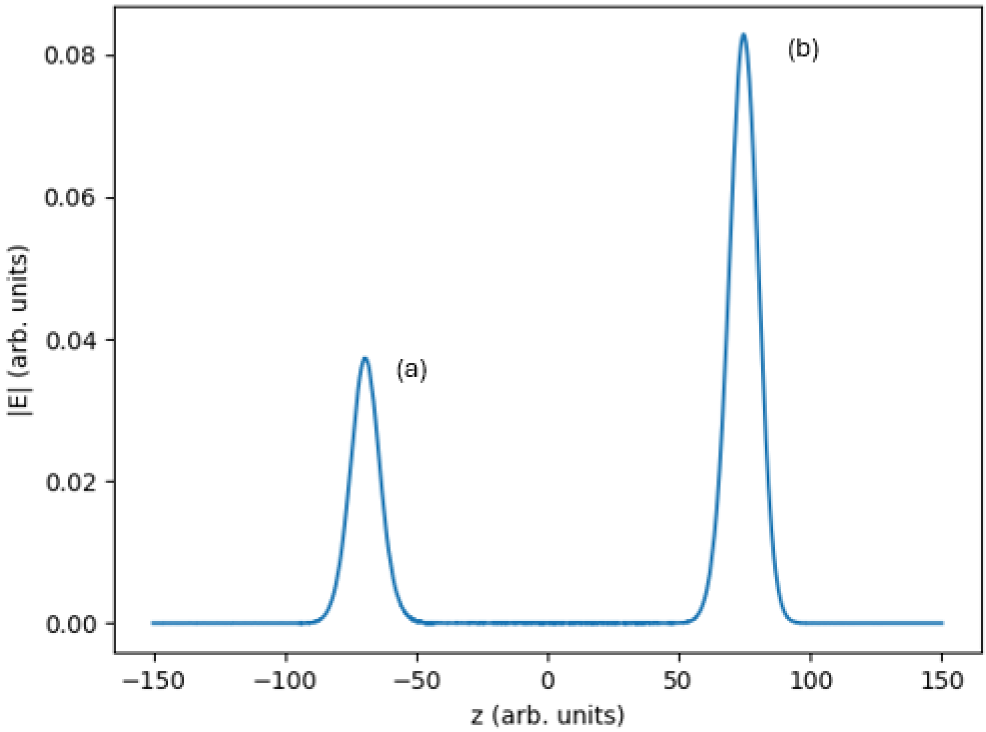

Source: The author, 2024.

In Figure 13, the beam encounters a Bragg grating with a periodic pattern as shown in Figure 14, where we illustrate the variation of the refractive index (n(z)) along the (z)-axis induced in a Kerr medium. The sinusoidal oscillation of the refractive index suggests that the medium has a periodic modulation, which may be caused by variations in the atomic vapor density. This modulation of the refractive index is crucial for understanding how the beam is guided or scattered along its trajectory.

Figure 14 – Variation of the refractive index $n(z)$ along the z-axis in arbitrary units. The oscillation of the refractive index indicates the presence of a spatial modulation that influences the beam propagation.

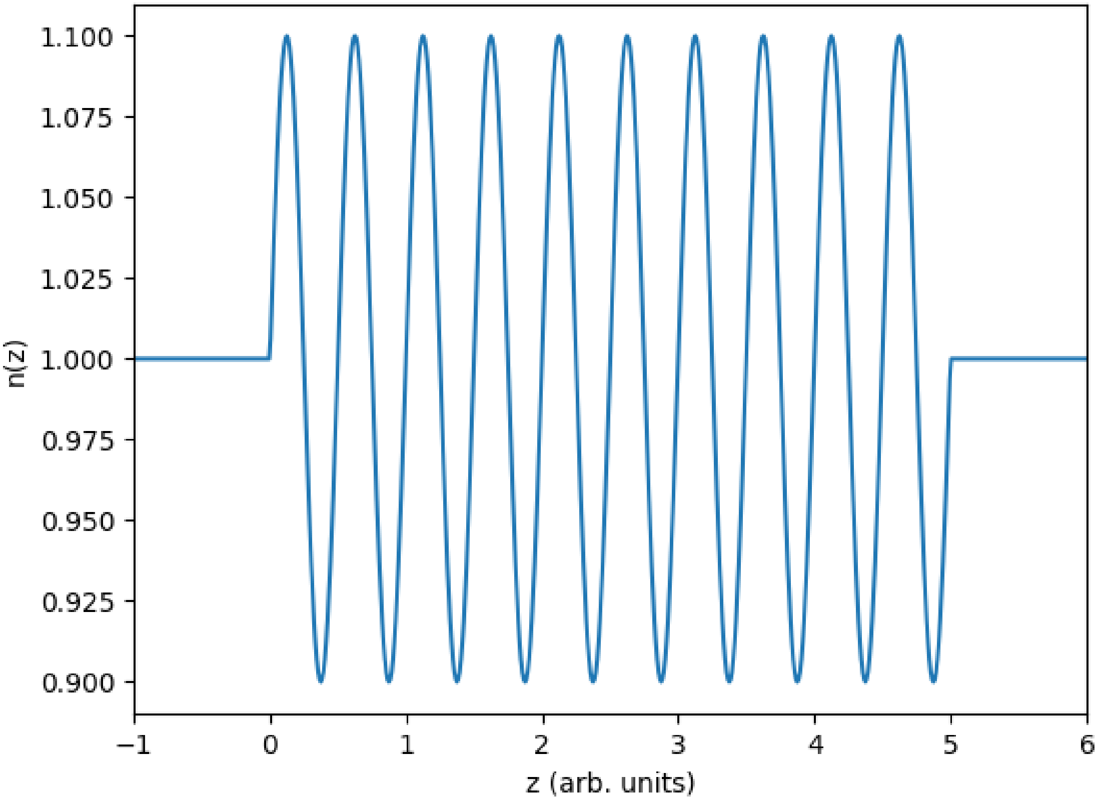

Source: The author, 2024.

Figure 15 shows the temporal and spatial evolution of our Gaussian beam. The more intense beam, which appears brighter, is the transmitted beam, while the less intense beam is the reflected beam. These beams are the same as in Figure 13; here, the objective is to analyze from the perspective of the intensity pattern in a 2D format. After the beam encounters the Bragg grating, part of its intensity is transmitted, and the other part is reflected. The interaction between these beams over time and space creates the observed pattern, which can be used to study phenomena of interference and wave propagation, as in this simulation we can modify the parameters of the grating and the beam.

Figure 15 – Temporal and Spatial Evolution of a Gaussian Beam through a Bragg Grating The two bright diagonal lines indicate the presence of two light beams. The more intense beam, which appears brighter, is the transmitted beam, while the less intense beam is the reflected beam.

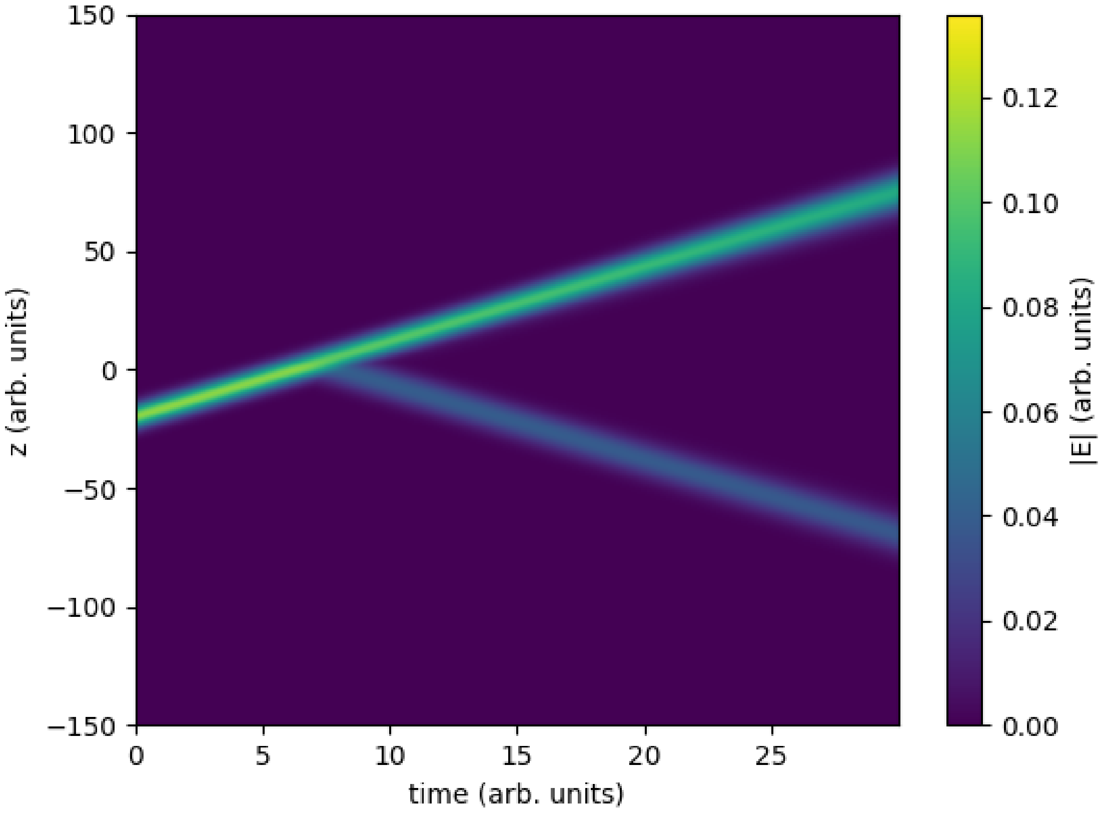

Source: The author, 2024.

Finally, Figure 16 presents a 3D view of the evolution of the electric field E as a function of time and position along the z-axis. This representation visualizes the beam's dynamics as it propagates over time, highlighting the continuous interaction between the beam and the medium's variations. The depicted peaks and valleys indicate how the beam's intensity evolves and suggest regions of strong coupling between the electric field and the modulated refractive index.

Figure 16 – 3D visualization of Gaussian beam propagation transmitted and reflected within an atomic vapor containing a Bragg grating. The two bright diagonal lines indicate the presence of two beams of light. The most intense beam, which appears brightest, is the transmitted beam, while the least intense beam is the reflected beam.

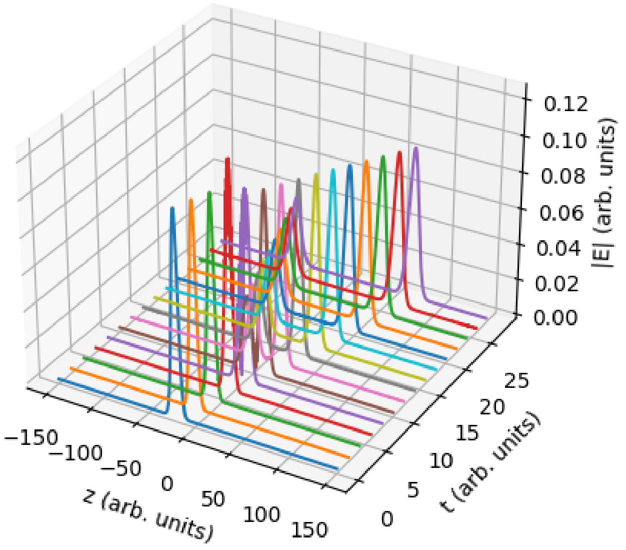

Source: The author, 2024.

4 STUDY OF THE VELOCITY REDISTRIBUTION OF EXCITED ATOMS IN CESIUM RYDBERG ATOM SPECTROSCOPY

This chapter focuses on the study of velocity redistribution of excited atoms and cesium Rydberg atom spectroscopy, addressing fundamental and advanced aspects of atomic physics. Rydberg atoms, with their extremely high energy levels, are explored in Section 4.1, alongside their unique properties such as enlarged atomic size and sensitivity to electric and magnetic fields.

While the study of Rydberg atoms and velocity redistribution has been addressed in numerous theoretical works, the objective of this research is to advance these studies through experimental methods. Specifically, this work will employ Rydberg atom spectroscopy on cesium atoms, focusing on velocity redistribution processes. By investigating these processes experimentally, we aim to contribute to a deeper understanding of the behavior of excited atoms, with potential applications in fields such as light-matter interaction and atomic-scale technologies. This chapter provides an in-depth exploration of these techniques, emphasizing their importance in understanding the outcomes of this study.

4.1 RYDBERG ATOMS AND THEIR PROPERTIES

The study of Rydberg atoms has become a cornerstone in understanding the fundamental interactions in atomic and quantum physics. Rydberg atoms, named after the Swedish physicist Johannes Rydberg, are characterized by one or more electrons excited to high principal quantum numbers (n). These atoms exhibit unique properties: they can be more than ten thousand times larger than their ground state counterparts, possess lifetimes that can exceed 1 ms, and demonstrate almost classical behavior with high magnetic susceptibility and low binding energy (Gallagher, 1994). Moreover, the exaggerated radiation effects of Rydberg atoms make them invaluable in various applications including studies in quantum electrodynamics, the classical limits of quantum mechanics, multiphoton transitions, and atomic interactions with electromagnetic fields due to their substantial dipole moments (Demtröder, 2008).

The history of Rydberg atoms dates back to the late 19th century when Liveing and Dewar documented the spectral lines in alkali elements. Johannes Rydberg furthered this work by proposing that the wavenumbers of these spectral series were interrelated and could be expressed with the now-famous Rydberg formula. This early interest in high principal quantum number transitions led to the first laboratory experiments with Rydberg atoms. However, due to the challenges in producing Rydberg atoms, which have low binding energy and large cross-sections, significant progress in their study was not made until the mid-20th century with the advent of tunable dye lasers. These lasers enabled precise investigations into the properties of Rydberg atoms, marking a significant milestone in atomic physics research.

Rydberg atoms have garnered attention for their large size and extended lifetimes, allowing them to be used in applications ranging from quantum computing to the exploration of fundamental physical constants. Understanding the properties and behaviors of Rydberg atoms, including their interactions and spectroscopic signatures, is essential for harnessing their full potential in scientific research and technological applications. The exploration of Rydberg atoms began with the observation of spectral lines in alkali metals. Liveing and Dewar's work in the late 19th century on these long series of spectral lines laid the groundwork for Johannes Rydberg's subsequent contributions. Rydberg proposed a formula that interrelated the wavenumbers of these spectral lines, suggesting they could be expressed as:

$$v_n = v_0 - \frac{R}{(n-\delta)^2} \tag{84}$$

Where (v_0) and (δ) are constants characteristic of the atom of the series, (R) is a universal constant (known as the Rydberg constant) and (n) is an integer. In 1906, R. W. Wood observed the absorption lines in sodium gas for transitions to states of ($n = 60$) (Wood, 1906). From the beginning, there was interest in transitions involving large (n), and these were the first laboratory experiments with Rydberg atoms.

Although the first laboratory experiments with Rydberg atoms occurred in the early 20th century, after this beginning, due to the difficulty in producing Rydberg atoms, which have low binding energy and large cross-section, studies focused on the development of quantum theory. In 1913, Bohr incorporated two important postulates into the ideas of classical physics: the first states that angular momentum is quantized in units of (h), and the second that the electron does not radiate continuously, but only during transitions between defined energy states.

In the mid-20th century, astronomers B. Höblund and P.G. Mezger revitalized the study of Rydberg atoms by observing transitions (n) close to 100 in hydrogen clouds in interstellar space (SCHMIDT, 2012). This interest also received a new and significant boost with the advent of tunable dye lasers. With these lasers and suitable experimental apparatus, it became possible to study the properties of Rydberg atoms with greater precision. This relatively simple method allowed access to specific states of Rydberg atoms and detailed investigation of their properties in the laboratory (Oliveira, 2001). To this day, laser excitation is the main means of producing Rydberg atoms.

To determine the properties of Rydberg atoms, it is necessary to define their wave functions. We will use the quantum defect theory to describe the wave functions of an electron in a Coulomb potential. In this approximation, we apply the method to an atom with a single valence electron in a Rydberg state, including the hydrogen atom as a special case. By analyzing the average radius of the orbit of an electron in a hydrogen atom, we can write the expression:

$$r = a_0 n^2 \tag{85}$$

where (a_0) is the Bohr radius igual ($a_0 = 5 \cdot 10^{-11} m$) (Demtröder, 2008). Thus, the excited electron in this state interacts with the atomic nucleus as if it were a nucleus with ($Z = n_e$), where (n_e) is the number of electrons in the Rydberg state. Since the electron in the Rydberg state has a high principal quantum number, according to Bohr's semi-classical model, it is very far from the nucleus. Therefore, it "sees"the nucleus with charge (Z) shielded by ($Z - 1$) electrons.

Consequently, we will have a potential similar to that of a hydrogen atom. The energy of a hydrogen-like Rydberg state depends only on (n), so states with the same (n), but different (ℓ), are degenerate. By analyzing the expression that defines the energy for alkali atoms and the one that defines the energy for hydrogen, we find that they differ in two aspects: in the expression for the energy of alkali atoms, the Rydberg constant takes into account the reduced mass of the electron and we use the effective quantum number (n^*), which corresponds to the quantum defect subtracted from (n).

$$E_{n,l} = -\frac{R_y}{(n - \delta_{n,l})^2} \tag{86}$$

The quantum defect $\delta_{n,l}$ arises from the interaction of the electron with the nucleus (other electrons and the nucleus) when, during its trajectory, it passes close to the nucleus. For highly excited states, the behavior in the quantum regime approaches the behavior in the classical regime, and we can use this orbit to understand its dynamics and describe states in terms of the electron's orbit.

The classical Bohr-Sommerfeld theory describes the motion of the electron around the nucleus, predicting that for low values of orbital angular momentum (l), the orbits are highly elliptical, allowing the electron to both penetrate and polarize the nucleus, generating the quantum defect. For high values of (l), the orbits become circular, making the atoms more hydrogen-like and the quantum defects smaller. Thus, for hydrogen-like excited states, in a first approximation, we consider the point nucleus; for low (l), the valence electron penetrates the nucleus with each revolution.

Therefore, it is necessary to distinguish between penetrating orbits (low values of l) and non-penetrating orbits (high values of l), for which the point core model is applicable. In the specific case of penetrating orbits, where the point core model is not valid, the consideration of the quantum defect is essential due to the interaction between the valence electron and the nuclear core with radius (r_0). This consideration fits the Rydberg series.

In general, the properties of Rydberg atoms follow a scaling law that varies with the effective quantum number ($n^* = n - \delta$). Basically, this will depend on the angular momentum (l), since (δ) also depends on it. After this brief introduction to the properties of Rydberg atoms, we will describe an overview of collisonal broadening and collisional shift.

4.2 COLLISIONAL BROADENING AND COLLISIONAL SHIFT

Collisional broadening is a phenomenon that occurs when atoms or molecules in a gas collide with each other, resulting in a change in the width of spectral lines. This effect is caused by the interaction between the particles during collisions, which temporarily alters the energy levels of the involved atoms or molecules. Collisional broadening is one of several mechanisms that can affect the shape of spectral lines, being particularly important under high-pressure conditions where collisions are more frequent.

To explain this phenomenon, let's consider an atom A, with energy levels E_i and E_k, approaching another atom B. The interaction between A and B alters the energies of both levels. This energy change depends on the electron shell structure of both partners A and B, the specific energy levels, and the energy between two atoms A and B varies with the distance $R(A, B)$, which we define as the distance between the centers of mass of A and B. The energy change generally differs for the different levels, and it can be positive (for repulsive potentials between A and B) or negative (for attractive potentials).

The comment raises a valid point—probabilities should not be negative, as probability values are bounded between 0 and 1. In the context of atomic interactions, what you are likely referring to is the sign of the interaction potential or the energy difference between states, not the probability itself. For repulsive interactions, the potential is positive, and for attractive interactions, it is negative, but the probability of interaction should always be positive. The interaction potential between two atoms depends on their relative velocity and the nature of their interaction. If the interaction between A and B is repulsive, the potential energy is positive, whereas for attractive interactions, the potential energy is negative. By plotting the energies $E_i(R)$ and $E_R(R)$ of atom A as a function of the distance R, we obtain potential curves, as schematically shown in Fig. 17.

The approach of two particles to a distance R_c, where the interaction energy between them becomes significant (i.e., the potential curves deviate noticeably from the value $E(R = \infty)$), is referred to as a two-body collision. The resulting system, $AB(R)$, from this interaction is called a collision pair. If the densities of particles A and B are not very high, the probability of three particles simultaneously approaching within a distance $R < R_2$ (which would constitute a three-body collision) is extremely small and

Figure 17 – Potential curves of the collision pair AB and A^*B.

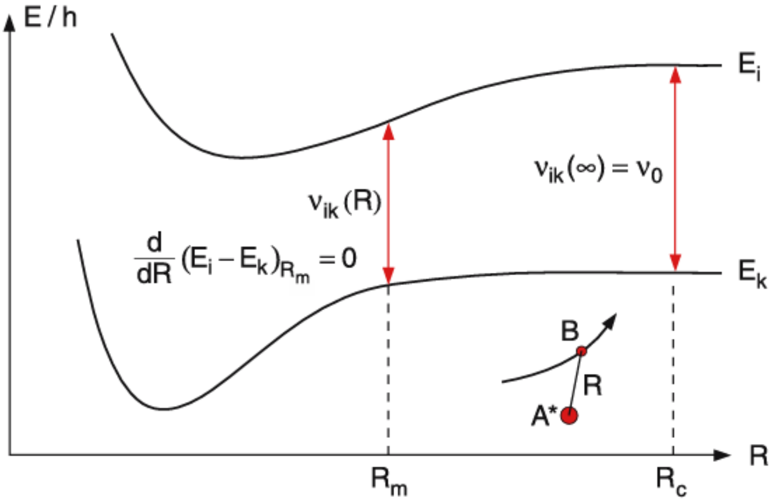

Source: Demtrõder, 2008.

can be neglected. The distance R_c, where the interaction becomes significant, is known as the collision radius. Therefore, if the relative speed of A and B is v, the duration of the collision, also referred to as the collision time, can be defined as:

$$\tau_{coll} = \frac{R_c}{v} \tag{87}$$

The frequency of the radiation ν_{ik} emitted or absorbed in the electron transition depends on the distance R at which the transition occurs (we assume here that during a collision, radiative transitions are of short duration) is:

$$\nu_{ik} = \frac{E_i(R) - E_k(R)}{\hbar} \tag{88}$$

The duration of the transitions, which is short compared to the mixing time, ensures an average distance R_m, with a distribution around R_m, as illustrated in Fig 17. In contrast to pure atomic wave functions, which predict constant distances and random thermal collisions, the collision broadening process leads to a broadening of the spectral lines in the gas. This broadening reflects a distribution of radiation frequencies ν_{ik}, centered around the most probable value $\nu_{ik}R_m$. These frequencies can shift relative to those predicted by the pure electronic wave function for an atomic temperature T_0.

Figure 18 also shows us the shift $\Delta\nu = \nu_0 - \nu_k(R_m)$, that depends on how the two energy levels $E_i(R_m)$ and $E_k(R_m)$ are altered at the distance $R(m)$. The intensity profile $I(\omega)$ of the collision-broadened emission line can be described by the following expression:

$$I(\omega) \propto \int A_{ik}(R) P_{coll}(R) \times \frac{d}{dR}(E_i(R) - E_k(R)) \tag{89}$$

where $A_{ik}(R)$ represents the probability of spontaneous transition, which varies with "R" due to the distortion of electronic wave functions caused by the interaction between the

Figure 18 – Shift and broadening of a spectral line by collisions.

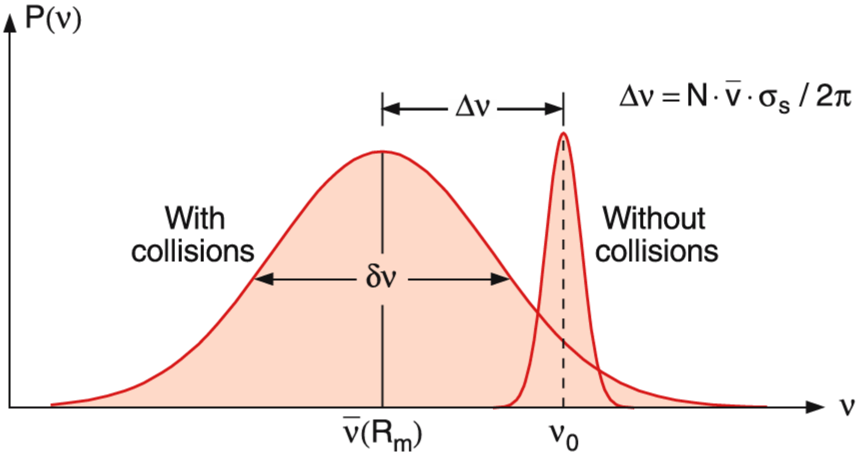

Source: Demtrõder, 2008.

particles. The shape of the intensity function $I(\omega)$ in equation 89 is determined by the convolution of these dependencies, resulting in a profile that can be analyzed to obtain information about the properties of the gas and the interactions between the particles.

The functions of the collision pair (AB) also depend on the distance (R). The probability $P_{coll}(R)$ that the distance (R) is between R and $R + dR$ is influenced by the interaction potential, the density, and the temperature of the gas. This probability $P_{coll}(R)$ can be derived by taking into account the probability distribution of collision distances and the dependence of transition energy on the system's temperature. The number of particles B in a spherical shell with radius R around atom A is given by:

$$N_B(R) = n_B 4\pi R^2 dR \exp\left(-\frac{E_{pot}(R)}{kT}\right) \tag{90}$$

where n_B is the average density of atoms B. The Boltzmann factor $\exp\left(-\frac{E_{pot}(R)}{kT}\right)$ takes into account that the energy of the collision pair depends on the potential interaction energy $E_{pot}(R)$ (Demtröder, 2008). Because te intensity of an absorption line is proportional to the density of absorbing atoms while they are forming collision pairs, the intensity profile of the absorption line can be writen as:

$$I(\omega)d(\omega) = C^* \left[R^2 \exp\left(-\frac{E^i_{pot}(R)}{kT}\right) \frac{d}{dT}\left(E_i(R) - E_k(R)\right)\right] dR \tag{91}$$

From equation 91, it is possible to determine the interaction potential. Often, spherical model potentials are substituted into eq. 91 such as the Lennard-Jones potential (Hindmarsh; Petford; Smith, 1967):

$$E_{pot}(R) = \frac{a}{R^{12}} - \frac{b}{R^6} \tag{92}$$

The discussions presented so far were only about elastic collisions, where the energy level of atom A is only shifted during the collision but returns to its initial value after the collision unless the atom has emitted a photon during the collision. The shift of absorption or emission lines caused by elastic collisions corresponds to an energy shift $\Delta E = \hbar\Delta\omega$. This energy difference is provided by the kinetic energy of the collision partners. In the case of positive shifts $\Delta\omega > 0$, the kinetic energy is lower after the collision than before.

Besides these elastic collisions, inelastic collisions can also occur in which the excitation energy of atom A is partially or completely transferred to the internal energy of the collision partner B, or to the translational energy of both partners A and B. Such inelastic collisions are called quenching collisions because they decrease the number of excited atoms A in level B; thus, they quench the fluorescence intensity. The total transition probability A_j for the depopulation of level B is the sum of the radiative and collision-induced probabilities (Hindmarsh; Farr, 1973):

$$A_i = A_{rad} + A_{col} \quad \text{with} \quad A_{col} = n_B \sigma_j v \sigma \nu \tag{93}$$

Inserting the relations:

$$\nu = \sqrt{\frac{8kT}{\pi\mu}} \quad , \mu = \frac{M_A M_B}{M_A + M_B} \quad \text{and} \quad p_B = n_B kT \tag{94}$$

into equation 93 we can obtain the total transition probability.

$$A_i = \frac{1}{\tau_{spont}} + apB \quad \text{with} \quad a = 2\delta_{ik}\sqrt{\frac{2}{\pi\mu kT}} \tag{95}$$

which is similar to the pressure dependence of the lifetime. From the pressure-dependent transition probability, a corresponding pressure-dependent line width $\delta\omega$ is caused, as it shortens the effective lifetime of the excited level (Demtröder, 2008). It can be written as the sum of two damping terms.

$$\delta\omega = \delta\omega_n + \delta\omega_{coll} = \gamma_n + \gamma_{coll} = \gamma_n + apB \tag{96}$$

In equation 96, the additional collision-induced line broadening a_{pB} is, therefore, often called pressure broadening. The energy difference between the corresponding states of atom (A) changes during the elastic collision time, the frequency ω of the emitted or absorbed radiation changes by $\delta\omega(R)$, this change depends on the interaction potential between (A) and (B). Although the frequency returns to its initial value after the collision, the phase shift is

$$\Delta\phi = \int_0^\infty \Delta\omega(t)dt \tag{97}$$

Elastic collisions are, therefore, called phase-changing collisions. As the frequency differences $\Delta\omega$ vary for collisions with different distances $R(AB)$, the set of atoms (A) undergoes random phase changes. The Fourier transform of the radiation provides a Lorentzian line profile, which is broadened and shows a shift of the line center. The line profile caused by elastic and inelastic collisions is obtained after a somewhat lengthy calculation.

$$I(\omega) = \frac{\left(\frac{\gamma_n+\gamma_{inel}}{2} + N\nu\sigma_b\right)^2}{(\omega - \omega_0 - N\nu\sigma_s)^2 + \left(\frac{\gamma_n+\gamma_{inel}}{2} + N\nu\sigma_b\right)^2} \tag{98}$$

Just like in collision broadening, the interactions between atoms or molecules during collisions can perturb the transitions between quantum states. This perturbation can result in a shift to higher or lower frequencies in the central position of the spectral lines. To better understand the physical meaning of the line broadening cross-section σ_b and the line shift cross-section σ_s, it is necessary to determine the relationship between the phase shift $\eta(R)$ and the potential $V(R)$. We consider potentials of the form:

$$V_i(R) = \frac{C_i}{R^n}, \quad V_k(R) = \frac{C_k}{R^n}, \tag{99}$$

between the atom in the level E_i or E_k and the perturbing atom B. The frequency shift $\Delta\omega$ for the transition $E_i \to E_k$ is then

$$\hbar\Delta\omega(R) = \frac{C_i - C_k}{R^n} \tag{100}$$

Line broadening can result from two main causes: the phase shift, which occurs due to the frequency change of the oscillator during the collision, and the extinction collisions, which reduce the effective lifetime of the excited level of A. The corresponding phase shift of oscillator A, caused by a collision with impact parameter R_0, where the dispersion of B is neglected, implies that the path of B is not deflected but follows a straight tangent line.

$$\Delta\phi(R_0) = \int_{-\infty}^{+\infty} \Delta\omega dt = \frac{1}{\hbar}\int_{-\infty}^{+\infty} \frac{(C_i - C_k)dt}{[R_0^2 + v^2(t-t_0)^2]^{n/2}} = \frac{\alpha_n(C_i - C_k)}{vR_0^{n-1}} \tag{101}$$

Equation 101 establishes the relationship between the phase shift $\Delta\phi(R_0)$ and the difference 100 of the interaction potentials, where α_n is a numerical constant that varies according to the exponent n in equation 100. Phase shifts can be positive $C_i > C_k$ or negative, depending on the relative orientation of the spin and angular momenta. The main contribution to the line broadening cross-section σ_b comes from collisions with small impact parameters, while the line shift cross-section σ_s has large values for large impact parameters. This indicates that elastic collisions at large distances do not cause noticeable line broadening but can still significantly shift the line center.

The influence of speed-changing collisions and the correlation between Doppler and collision broadening on the spectral line profiles is considered in a unified manner using the classical phase shift theory of Anderson-Talman for collision broadening and the Galatry diffusion model for the motion of radiating particles. A general formula for the correlation function is derived from the impact limit, which produces the well-known speed-dependent Voigt profile in the case where speed-changing collisions are neglected, but Doppler-collision correlations are taken into account. In the opposite case, when Doppler collision correlations are omitted, but speed-changing collisions are included, this formula becomes identical to the one derived by Galatry (Ciuryło; Szudy, 1997).

4.3 VELOCITY REDISTRIBUTION

In this chapter, we address the analysis of velocity redistribution in excited atoms, is a complex phenomenon, influenced by various factors such as collisions and interactions with external fields. To achieve a detailed understanding, we explore two complementary approaches: the relaxation rate and the Keilson-Storer kernel. Firstly, the transverse relaxation rate (Γ_T) is examined as a fundamental parameter describing the system's dynamics under different pressures and collision conditions.

Equation 120 provides a standard interpolation between the Knudsen and high-pressure limits, allowing for precise analysis of the experimental conditions where velocity redistribution occurs. The importance of this parameter is highlighted by comparing the effects of velocity-changing collisions and transit relaxation, offering a critical view of the validity of simplifications made in different pressure regimes. Additionally, the Keilson-Storer kernel is introduced as an essential tool for modeling velocity redistribution. The use of this model is justified by its ability to accurately represent both strong and weak collisions, providing a robust method for describing interactions between atoms and buffer gas atoms.

The choice of the Keilson-Storer kernel is particularly relevant due to its correct physical properties and adherence to detailed balance, allowing for a rigorous interpretation of experimental data. Although the main focus of the work is on cesium atoms, the use of sodium atoms for theoretical description is justified for several reasons. Sodium is often used as a representative model due to its simplicity, and many of the fundamental concepts applied to sodium atoms are also relevant to cesium atoms. The comparable properties and similar redistribution mechanisms between these atoms enable the successful transposition of results obtained for sodium to the cesium system, facilitating the application of the theories and models developed in this work. By integrating these approaches, this chapter provides a comprehensive and detailed understanding of the velocity redistribution processes, addressing both theoretical contributions and practical implications of these phenomena.

4.3.1 GENERALIZED BLOCH EQUATIONS

To explain this phenomenon we will base ourselves on the Bloch equations, using sodium atoms, (Haverkort; Woerdman, 1990) worked with Bloch equations in an arbitrarily strong laser field and with the Boltzmann equation, describing the evolution due to collisions between Na atoms and buffer gas atoms. We will restrict ourselves to a simplification of the four-level scheme of Na atomic levels, as shown schematically in Fig. 19. Levels 1 and 2 represent the hyperfine levels of the ground state $3S_{1/2}F = 1$ and $F = 2$, respectively.

Figure 19 – The simplified energy level diagram of Na. Levels 1 and 2 are the $3S_{1/2}, F = 1$ and $F = 2$ ground-state levels, respectively. Levels 0 and 3 are the resonant and the nonresonant $3P$ excited-state fine-structure levels, respectively. The 3^2P hyperfine splitting has been neglected. The level numbering is chosen in such a way that level 0 is the $3P_{1/2}$ level for D_1 excitation and the $3P_{3/2}$ level for D_2 excitation.

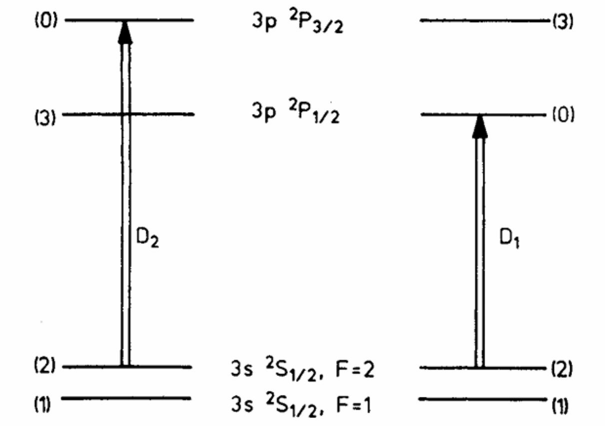

Source: Haverkort; Woerdman, 1990.

The excited state directly populated by the pumping laser can be either the fine structure level $3P_{1/2}$ or $3P_{3/2}$. Finally, level 3 is the non-resonant fine structure level of the electronic state $3P$, which is not directly populated by the pumping laser since the fine structure separation (510 GHz) is much larger than the Doppler width (1.6 GHz). The hyperfine and Zeeman structures in the electronic $3P$ state are neglected in our model. This simplification is justified by the fact that, under most experimental conditions (Werij et al., 1987a), the collisional linewidth, power-broadened linewidth, and the collisional mixing rate are comparable to or greater than the hyperfine separations of the excited state.

To simplify the discussion, we start with an evolution equation for the general case of non-degenerate four-level absorbers. Throughout this section, these four-level absorbers will be specified as Na atoms, introducing degeneracies. The set of absorbers is described in terms of the density matrix elements $\rho_{ij}(r, v, t)$ which, in the case of $i = j$, simply represent the velocity distribution at level i, and in the case of $i \neq j$, represent the coherences between levels i and j. The evolution of ρ_{ij} is determined by a generalized Bloch equation. This equation derives from the optical Bloch equation, which is essentially the Liouville equation, and the quantum mechanical version of the Boltzmann equation (Berman, 1978).

$$\left(\frac{\partial}{\partial t} + v \cdot \frac{\partial}{\partial r}\right) \varrho_{ii} = \frac{-i}{\hbar}[\mathfrak{H}, \varrho]_{ii} - A_i\varrho_{ii} + \sum_j \alpha_{ji} A_i \varrho_{jj} + \mathcal{L}_{ii}\varrho_{ii} + \sum_{j \neq i}(\mathcal{L}^{+}_{ji}\varrho_{jj} + \mathcal{L}^{-}_{ij}\varrho_{ii}) \quad (102)$$

Here, the left side represents the flux term from the Boltzmann equation. On the right side, the commutator of the Hamiltonian $\mathcal{H}$ and the density matrix $\varrho(r, v, t)$ describes absorption and emission induced by the pumping laser radiation; spontaneous decay is included by a loss term $-A_i\varrho_{ii}$ and a gain term $\alpha_{ji}A_i\varrho_{jj}$, where α_{ji} represents the branching ratio of spontaneous decay from level j to level i. The collision operator $\mathcal{L}_{ii}$ describes the effect of collisions that alter the velocity (vcc) within a single level. The collision operator $\mathcal{L}^{+}_{ji}$ is a gain term describing transfer from level j to level i.

The operator $\mathcal{L}^{-}_{ji}$ describes loss in the transfer from level i to level j. These operators are used to include the effect of collisions that change fine structure (fsc) between levels 0 and 3. The Hamiltonian $\mathcal{H}$ has matrix elements:

$$\mathcal{H}_{ij} = \hbar\omega_i - \mu_{ij} \cdot \delta_{ij} \quad (103)$$

where ω_i is the energy of level i, μ_{ij} is the transition dipole moment, and $E_{ij}(t)$ is the oscillating electric field due to the pumping laser, tuned close to the transition $i \to j$:

$$\delta_{ij}(r, t) = \delta_{ij} \cos(kz - \omega_L t) e_x \quad (104)$$

Here, e_x is a unit vector indicating the polarization of the laser field and $k = \omega_L / c$. The temporal evolution of the off-diagonal elements of the density matrix is governed by a generalized Bloch equation:

$$\frac{\partial \varrho_{ij}}{\partial t} + v \cdot \frac{\partial \varrho_{ij}}{\partial r} = \frac{-i}{\hbar}[\mathcal{H}, \varrho]_{ij} - \left(\frac{A_i}{2} + \frac{A_j}{2} + \Gamma^{Ph}_{ij} + iS^{Ph}_{ij}\right) \varrho_{ij} \quad (105)$$

For Na, we assume that the perturbing density is much higher than the Na density, and the perturbing distribution remains Maxwellian. The rotating wave approximation (RWA) and field interaction notation are used for the off-diagonal elements ρ_{ij}:

$$\varrho_{ij}(r, v, t) = \widetilde{\varrho_{ij}}(r, v, t) \exp(-i(kz - \omega_L t)) \quad (106)$$

Temporal derivatives are set to zero, and the flux term is replaced by a relaxation term describing an ad hoc diffusive coupling between the illuminated volume and an infinite reservoir of atoms in equilibrium. The generalized Bloch equations for Na are simplified by considering that transfer collisions occur only between levels 0 and 3, and the laser only couples level 1 to 0 and level 2 to 0 with Rabi frequencies:

$$Q = \frac{\mu_0 g_0}{2\hbar}\sigma_{10} - \frac{\mu_0 g_0}{2\hbar}\sigma_{20} \quad (107)$$

The steady-state equations for the relevant elements of the density matrix are:

$$\frac{\partial \widetilde{\varrho_{00}}}{\partial t} = i\Omega(\widetilde{\varrho_{10}} - \widetilde{\varrho_{01}}) + i\Omega(\widetilde{\varrho_{20}} - \widetilde{\varrho_{02}}) - A_0\widetilde{\varrho_{00}} + \mathcal{L}_{00}\widetilde{\varrho_{00}} + \mathcal{L}_{03}^{-}\widetilde{\varrho_{00}} + \mathcal{L}_{30}^{+}\widetilde{\varrho_{33}} + \Gamma_T(n_0^{(0)}W(v)) = 0 \tag{108}$$

$$\frac{\partial \widetilde{\varrho_{11}}}{\partial t} = i\Omega(\widetilde{\varrho_{01}} - \widetilde{\varrho_{10}}) + \alpha_{01}A_0\widetilde{\varrho_{00}} + \alpha_{31}A_3\widetilde{\varrho_{33}} + \mathcal{L}_{11}\widetilde{\varrho_{11}} + \Gamma_T(n_1^{(0)}W(v) - \widetilde{\varrho_{11}}) = 0 \tag{109}$$

The detunings of the laser field from the centers of the transitions $1 \to 0$ and $2 \to 0$ are given by:

$$\Delta_{10} = \omega_L - (\omega_0 - \omega_1) + S_{10}^{Ph}, \tag{110}$$

$$\Delta_{20} = \omega_L - (\omega_0 - \omega_2) + S_{20}^{Ph}, \tag{111}$$

The Bloch equations for Na assume that the atoms remain in the laser beam long enough to reach a steady state. The effects of transients and the terms $\Gamma_T\varrho_{ij}(i \neq j)$ are neglected. The diagonal elements of the matrix $\widetilde{\varrho_{21}}(v)$ are identified with the velocity distribution functions $f_i(v)$ through:

$$f(v) = \varrho_{ii}(v) \tag{112}$$

4.3.2 RATE EQUATIONS FOR VELOCITY DISTRIBUTIONS

In the analysis of the equations of motion for the sodium atom system, it is possible to eliminate the coherences $\widetilde{\varrho_{10}}$ and $\widetilde{\varrho_{20}}$ from Bloch Equations. However, it is generally not possible to eliminate the coherence $\widetilde{\varrho_{21}}$. Nonetheless, in a strong collision model, where a Maxwellian velocity distribution is established in a single collision, $\widetilde{\varrho_{21}}$ can also be eliminated. Direct calculations (Haverkort; Woerdman, 1990) show that the coherence $\widetilde{\varrho_{10}}$ in such a strong collision model can not only be eliminated from the system of equations but actually goes to zero in the limit $\Omega^2 \ll \Omega \cdot \Delta\omega_{HFS}$, where Ω is the Rabi frequency, $\Gamma = \Gamma_{10}^{Ph} + A_0$ is the homogeneous linewidth, and Δ is the angular frequency separation between levels 1 and 2.

Physically, the coherence $\widetilde{\varrho_{21}}$ can be neglected because the pumping laser interacts with two distinct velocity classes in levels 1 and 2, which do not overlap spectrally, provided that the Rabi frequency is sufficiently small. Effectively, for each of these two velocity classes, only two levels are coupled by the laser field, allowing for the elimination of the inter-level coherences $\widetilde{\varrho_{10}}$ or $\widetilde{\varrho_{20}}$. In the current treatment, the coherence $\widetilde{\varrho_{21}}$ will be neglected. The resulting set of linear equations is:

$$\frac{\partial f_0}{\partial t} = 0 = R_{10}\left(f_1\frac{g_1}{g_0}f_0\right) + R_{20}\left(f_2\frac{g_2}{g_0}f_0\right) - A_0f_0 + \mathcal{L}_{21}f_0 + \mathcal{L}_{03}^{-}f_0 + \mathcal{L}_{03}^{+}f_3 + \Gamma_T(n_0^0W(v) - f_0) \tag{113}$$

$$\frac{\partial f_1}{\partial t} = 0 = -R_{10}\left(f_1\frac{g_1}{g_0}f_0\right) + \alpha_{01}A_0f_0 + \alpha_{31}A_3f_3 + \mathcal{L}_{11}f_1 + \Gamma_T(n_1^0W(v) - f_1) \tag{114}$$

$$\frac{\partial f_2}{\partial t} = 0 = -R_{20}\left(f_2\frac{g_2}{g_0}f_0\right) + \alpha_{02}A_0f_0 + \alpha_{32}A_3f_3 + \mathcal{L}_{22}f_2 + \Gamma_T(n_2^0W(v) - f_2) \tag{115}$$

$$\frac{\partial f_3}{\partial t} = -A_3 f_3 + \mathcal{L}_{33} f_3 + \mathcal{L}_{30}^{-} f_3 + \mathcal{L}_{03}^{+} f_0 + \Gamma_T (n_3^0 W(v) - f_3) \tag{116}$$

where $R_{ij}(v_z)$ are velocity-selective excitation rates:

$$R_{ij}(v) = \frac{2\Omega^2}{\Gamma} L_{ij}(v_z) = \frac{\delta_H I}{\hbar\omega_L} \frac{g_0}{g_1 + g_2} L_{ij}(v_z) = \frac{1}{2} A_i \left(\frac{I}{I_0}\right) L_{ij}(v_z) \tag{117}$$

$$L_{ij}(v_z) = \frac{\Gamma^2}{(\Delta_{ij} - k v_z)^2 + \Gamma^2} \tag{118}$$

$$\Gamma = \Gamma_{10}^{Ph} + \frac{1}{2} A_0 = \Gamma_{20}^{Ph} + \frac{1}{2} A_0 \tag{119}$$

where $L_{ij}(v_z)$ is a Lorentzian function, δ_H is the homogeneous absorption cross-section, and I_s is the saturation intensity for a two-level system without velocity-changing collisions. These quantities are explicitly defined by Eqs. 117, 118, and 119. Degeneracies of the levels are neglected in our treatment, focusing on the case of sodium. The factors $\frac{g_0}{g_1}$ and $\frac{g_0}{g_2}$ denote the ratio of the degeneracy of level g_1 and g_2 to the resonant ground level.

It should be noted that the set of Eqs. 113 to 116 can be interpreted as a set of rate equations; indeed, each term in these equations has a simple heuristic interpretation. Due to the fact that time derivatives are defined as zero, coherences are not explicitly displayed in the set of equations.

4.3.3 RATE OF RELAXATION

The transverse relaxation rate Γ_T, present in the rate equations, can be obtained by interpolating between the Knudsen limit and the high-pressure limit (Tomasi et al., 1993) in a standard manner (Hermans et al., 1970).

$$\Gamma_T = \frac{2.405^2 D_g}{R^2} + \left(\frac{1}{1 + \frac{K}{p}}\right) \tag{120}$$

where R is the radius of the pumping laser beam, D_g is the diffusion coefficient of Na atoms in the ground state under the prevailing perturbing pressure, 2.405 is the smallest zero of the Bessel function of order zero, and K is the Knudsen coefficient defined as:

$$K = c \cdot \frac{\bar{l} p}{R} \tag{121}$$

Here, $\bar{l}$ is the mean free path and c is a numerical constant equal to 6.8 for a hard sphere interaction. Equation 120 is valid across the entire pressure range, including the Knudsen limit. In this latter limit, the relaxation rate reduces to $\Gamma = \frac{\bar{v}}{2R}$, which is simply the reciprocal flight time of a Na atom within the pumping beam.

In the rate equations, transit relaxation has a similar effect to strong velocity-changing collisions, i.e., collisions that thermalize the velocity distribution. However, transit relaxation is inversely proportional (through D_g) to the buffer gas pressure p, as long as $p \ll K$, while the collision rate is linearly proportional to p. For example, in the case of Xe as the buffer gas, velocity-changing collisions are strong, and using Eq. 120 with collision rate data (which will be presented in Section 4), we have:

$$\frac{\Gamma_T}{\Gamma_g^{ccc}} = \frac{6.10^{-3}}{(PR)^2} \text{ (in Torr, R in mm)}, \tag{122}$$

where Γ_g^{ccc} is the relaxation rate for velocity-changing collisions in the ground state. In the limit where the pressure becomes small $(pR < 0.1\,\text{mm Torr})$, transit relaxation cannot be neglected. All authors who have calculated drift velocity often neglected transit relaxation and obtained an expression for drift velocity that is independent of p in this low-pressure limit, such as (Ho; Wang; Chu, 1986), leading to predicted drift velocities as quite large (e.g., $v_{drift} \gg 10\,\text{m/s}$). Furthermore, the expression for the drift velocity obtained in these theories is proportional to $\frac{\Gamma_e^{ccc}-\Gamma_g^{ccc}}{\Gamma_g^{ccc}}$ even in the zero-pressure limit.

These results correspond to a rather unrealistic situation where the laser beam diameter R must increase proportionally with $1/p$ to keep the mean free path small compared to R. In all practical situations, R is kept constant, and transit relaxation should be considered by substituting into the theoretical expressions of Nienhuis (Nienhuis, 1986) and Gel'mukhanov (Werij et al., 1987b):

$$\Gamma_i^{ccc} \rightarrow \frac{\Gamma_i^{ccc}}{\Gamma_T} \tag{123}$$

The corrected expression for the drift velocity in the case of 2-level optical absorbers experiencing strong velocity-changing collisions then becomes proportional to:

$$v_{dr} \propto \frac{\Gamma_e^{ccc} - \Gamma_g^{ccc}}{\Gamma_e^{ccc} - \Gamma_T} \tag{124}$$

resulting in a zero drift velocity in the limit as p approaches zero.

4.3.4 THE KEILSON-STORER KERNEL

The collision operator $\mathcal{L}$ can be rewritten in terms of a collision rate $\gamma(v)$ and a kernel $K(v' \rightarrow v)$ such that:

$$\mathcal{L}_{ii} f(v) = -\gamma_i(v) f(v) + \int dv' K_i(v' \rightarrow v) f(v'), \tag{125}$$

$$\Gamma_i(v') = \int dv K_i(v' \rightarrow v) \tag{126}$$

$K(v' \rightarrow v)$ is a gain term for the velocity range around v and is defined as the probability density in velocity space that a Na atom has its velocity changed from v' to v as a result of collisions with buffer gas atoms. Since the Na-perturbator interaction potential is known, one can, in principle, calculate exactly the collision rate and kernel through the differential cross-section (Saxon; Olson; Liu, 1977). However, such calculations are extremely complicated. It is more useful, at the current stage of LID research, to connect the drift velocity in LID to a kernel model that contains some parameters which can be related to the interatomic potential. We chose a Keilson-Storer (**??**) kernel model of the form:

$$K^{KS}(v' \to v) = \Gamma^{ccc} \frac{1}{\pi(\Delta u^2)^{3/2}} \exp\left(-\frac{(v-\alpha^{KS}v')^2}{\Delta u^2}\right) \tag{127}$$

where:

$$\Delta u = \bar{v}\sqrt{1-(\alpha^{KS})^2} \tag{128}$$

Here, the velocity before the collision is v', the average velocity after the collision is $v = \alpha^{KS}v'$, and Δu is the rms average rate of velocity dispersion after the collision. The choice (Haverkort; Woerdman, 1990) to use the Keilson-Storer model is motivated by the following reasons:

- The Keilson-Storer kernel is physically correct in both limits of a Maxwellian velocity distribution.
- The Keilson-Storer kernel obeys detailed balance and therefore conserves strong collisional invariants (and weak collisions for Maxwellians). In the first limit, the K-S kernel approaches the classical limit of the δ function.
- In the weak limit, the K-S kernel has been used by various authors (Kolchenko et al., 1973) from the Fokker-Planck equation; this equation is the exact solution of the Green's function to describe weak collisions.

$$K(v,\Delta t; v_0) = \frac{1}{\left(\frac{2\pi q}{\beta}(1-e^{-2\beta\Delta t})\right)^2} \exp\left(-\frac{\beta(v-v_0 e^{\beta\Delta t})^2}{2\pi q(1-e^{-2\beta\Delta t})}\right) \tag{129}$$

where $K(v,\Delta t; v_0)$ is the velocity distribution at time Δt, assuming it is a delta function $\delta(v-v_0)$ at time $t=0$, and $2q/\beta = \bar{v}^2$ is the damping rate. Although the Fokker-Planck equation typically applies to the motion of Brownian particles in a fluid, where a large number of collisions occur in the observation time Δt, a connection with weak collisions between Na atoms and perturbators can be easily made by identifying:

$$\alpha^{KS} = e^{-\beta\Delta t}, (\alpha^{KS} \approx 1), \tag{130}$$

and considering the case where a large number of very weak Fokker-Planck type collisions occur in a time interval Δt. A large number of very weak collisions can be considered analogous to the random force in the Langevin equation. Such a large number of very soft collisions is equivalent to a single kinetic collision producing δv and occurring at a rate $\Gamma = 1/\Delta t$. The eigenfunctions of the Keilson-Storer kernel are identical to the exact eigenfunctions of the kernel for Maxwell molecules; these are molecules with a repulsive r^{-4} interaction. In turn, the eigenfunctions for Maxwell molecules are often used in kinetic theory to expand the distribution function, as they are known to be a good approximation to the true eigenfunctions in many cases (McCourt; Liu, 1982). The eigenvalues (Snider, 2023) of the Keilson-Storer kernel are $\Gamma^{ccc}(\alpha^{KS}n)$; the eigenvalue $n = 1$ describes diffusion. This results in:

$$\Gamma_i^{ccc} = N_p v_r \delta_i^{ccc} \tag{131}$$

$$\sigma_i^{Dif} = (1 - \alpha^{KS})\delta_i^{ccc} \tag{132}$$

$$D_i = \frac{k_B T}{m}(N_p v_r \delta_i^{Dif})^{-1} \tag{133}$$

$$v_r = \left(\frac{8kT}{\pi\mu}\right)^{\frac{1}{2}} \tag{134}$$

where σ_i^{ccc} is the cross section for velocity-changing collisions, σ_i^{Dif} is the diffusion cross section, and D is the diffusion coefficient. A generalization of this procedure for an arbitrary kernel and for higher eigenfunctions was presented separately (Berman; Haverkort; Woerdman, 1986); here, two different sets of relations between the collision kernel and the transport coefficients were established. These published relations are identical for a kernel that correctly obeys collisional dynamics, while they need not be identical for a phenomenological kernel unrelated to a potential. It has been found that both sets of relations are equivalent for a Keilson-Storer kernel. This fact does not contradict viscosity when using a Keilson-Storer kernel, provided that some justification for using this kernel is adopted.

We address the velocity redistribution of excited atoms through the application of theoretical models and established computational methods. The choice to use the rate equation model and the Keilson-Storer kernel was motivated by the need for an accurate and adaptable description of the velocity redistribution phenomena in complex atomic systems. The relaxation rate model and the Keilson-Storer kernel provide a solid foundation for analyzing and interpreting velocity redistribution phenomena. The transverse relaxation rate Γ_T was described in terms of the Knudsen and high-pressure limits, offering a detailed understanding of the conditions under which transit relaxation becomes relevant. Additionally, the Keilson-Storer kernel was selected for its ability to correctly capture collisional dynamics across various pressure regimes and its properties compatible with kinetic theory.

These models not only guide the interpretation of experimental data but are also fundamental to the computational simulation we perform. We use Python to model and simulate the velocity redistribution, allowing for detailed analysis and visualization of the physical processes involved. The results of these simulations will be crucial for validating our theoretical models and for a deeper understanding of the behavior of cesium atoms under experimental conditions. With this, we hope to make a significant contribution to the understanding and manipulation of excited atoms in future experiments.

5 DESCRIPTION OF THE ATOMIC SYSTEM AND EXPERIMENTAL SETUP

This chapter provides a detailed exploration of the atomic system and experimental setup used in the study of velocity redistribution of excited atoms and cesium Rydberg atom spectroscopy. Understanding the complexities of the cesium atomic system and its energy levels (Section 5.1), as well as examining the influence of pressure effects on cesium atomic behavior (Section 5.2).

Rydberg states, characterized by their high principal quantum numbers and unique spectroscopic schemes (Section 5.3), are the central focus for studying atomic interactions and sub-Doppler level transitions. The experimental setup (Section 5.4), meticulously designed and detailed, is essential for conducting precise measurements and maintaining controlled data acquisition environments. Specific aspects such as thickness measurement techniques (Section 5.4.1) and frequency scale calibration methods (Section 5.5) are discussed to ensure the reproducibility of experimental results. This chapter establishes a solid foundation for subsequent analyses, emphasizing the importance of each component in advancing our understanding of atomic dynamics and spectroscopic techniques in Rydberg atoms.

5.1 CESIUM ATOMIC SISTEM AND LEVELS

Alkali metals in their ground state have a closed shell, with only one valence electron in the outermost electron shell. Although alkali metals are multi-electron atoms, with appropriate approximations, we can treat the Hamiltonian in an approximate manner, as if they were single-electron atoms. Since the nucleus is composed of closed shells, it does not contribute to the orbital angular momentum of the atom, leaving only the orbital angular momentum of the single outer electron. The state of this electron is determined by its orbital angular momentum l and its spin angular momentum s, which couple to form the total angular momentum of the electron j.

Thus, the contribution to the total electronic angular momentum comes from the atom's outermost shell; the total orbital and spin angular momenta are given by $L = l$ and $S = s$, and the total angular momentum for all electrons is given by $J = j$. The orientation of S with respect to L defines the spin-orbit interaction $V_{so} = AL \cdot S$, and the different energy states correspond to different values of J. This state splitting caused by the spin-orbit interaction results in the fine structure of the atom. The LS coupling is valid if the spin-orbit interaction is small compared to the separation of the energy levels.

The structure of alkali metals becomes a bit more complex when we consider the interaction of the nuclear spin, denoted by I, with the total angular momentum of the electron J. The coupling of these angular momenta gives rise to a new energy level splitting, called hyperfine coupling. The total angular momentum of the atom is $F = I + J$, with values $|J - I| \leq F \leq J + I$. Different values of F for the same values of I and J are shifted by the interaction $AI \cdot J$ between the nuclear spin and the electronic angular momentum. The resulting energy structure is known as hyperfine structure (hfs), and is generally smaller than the fine structure due to the smaller nuclear magnetic moment. Cesium is an alkali metal that has 55 electrons, of which only one is in its outermost shell (Steck, 2003). According to Pauli's rule, these electrons are distributed as follows:

$$1s^2\, 2s^2\, 2p^6\, 3s^2\, 3p^6\, 4s^2\, 3d^{10}\, 4p^6\, 5s^2\, 4d^{10}\, 5p^6\, 6s^1 \tag{135}$$

In the ground state, we have $l = 0$, which together with the spin angular momentum $s = 1/2$, according to the addition of angular momentum, results in the quantum number $j = 1/2$, identifying the $6^2S_{1/2}$ level. For the first excited state, we have $l = 1$ and $s = 1/2$, corresponding to $j = 1/2$ and $j = 3/2$. Thus, the first excited $6p$ state of cesium is composed of the states $6^2P_{1/2}$ and $6^2P_{3/2}$, forming two lines for optical excitation that define the fine structure of cesium:

$$\textbf{D1 Line} : 6^2S_{1/2} \to 6^2P_{1/2} \tag{136}$$

$$\textbf{D2 Line} : 6^2S_{1/2} \to 6^2P_{3/2} \tag{137}$$

Each of these lines has its own hyperfine structure. In the case of cesium, the D1 line corresponds to a wavelength of approximately 894 nm and the D2 line to approximately 852 nm (Steck, 2003). In this work, the experiment is performed on the D1 line, which has a hyperfine structure with closed transitions due to electric dipole selection rules. In figure 20, we schematically show the D1 line of cesium along with its hyperfine structure.

Figure 20 – Cesium D1 transition hyperfine structure, with frequency splittings between the hyperfine energy levels.

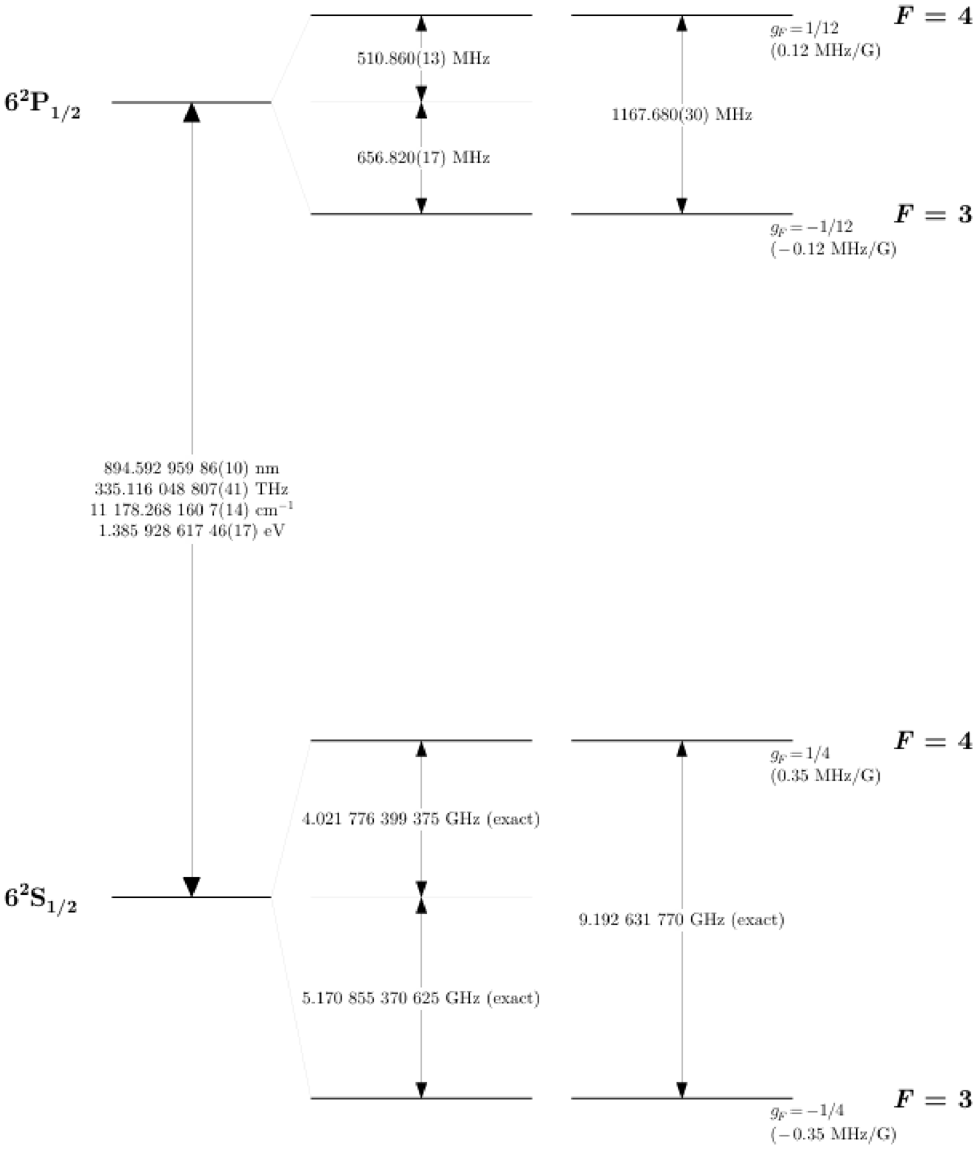

Soucer: Steck, 2003.

5.2 PRESSURE EFFECTS

Cesium vapor is typically used in atomic spectroscopy experiments in low-pressure cells, where a small portion of cesium under the given conditions results from the evaporation of a small piece of cesium. Under the above-mentioned conditions, less than 1 mTorr, cesium vapor can be considered a nearly ideal gas, meaning the thermodynamic equation $PV = nRT$ is valid, where n is the number of moles of gas. However, in the cells, there is some non-evaporated cesium, meaning it remains in the liquid or solid state (Stone et al., 1966). Thus, the number of atoms is also a function of temperature so that the vapor pressure balances the surface pressure of the non-evaporated cesium. For cesium atoms, the pressure is a function of temperature, given empirically by (Steck, 2003):

$$\log_{10} P_v = 2.881 + 4.711 - \frac{3999}{T} \quad \text{(liquid phase)} \tag{138}$$

$$\log_{10} P_v = 2.881 + 4.165 - \frac{3830}{T} \quad \text{(solid phase)} \tag{139}$$

where the pressure P is given in mTorr and the temperature T in Kelvin, with the phase change occurring at 28.44℃ as observed in figure 21.

Figure 21 – Vapor pressure of cesium from equations 138 and 139.

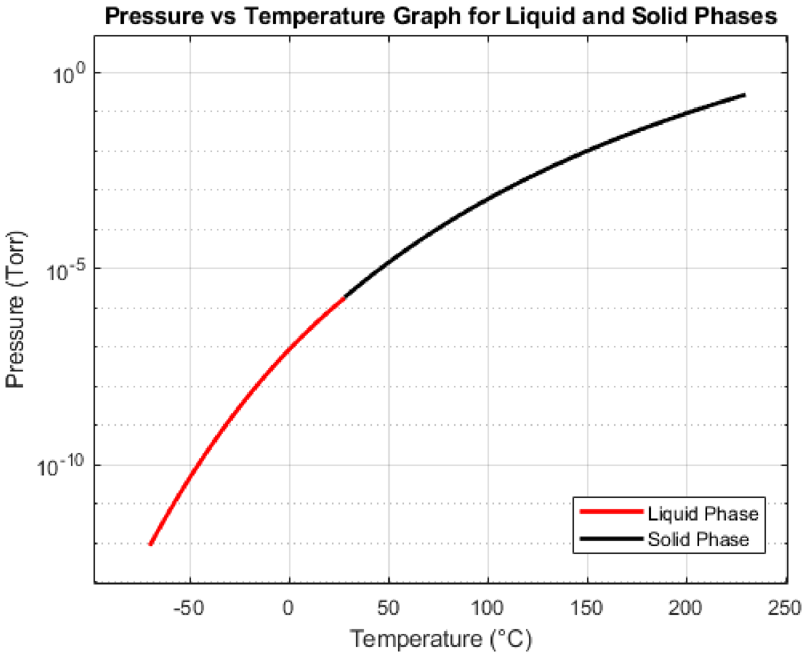

Soucer: The Author, 2024.

In addition, in figure 22 we also plot from the equations 138 and 139 the density in units of $atom/cm^{-3}$, as a function of the temperature in $^{\circ}C$ for the liquid and solid phases of cesium.

Figure 22 – Vapor pressure of cesium from equations 138 and 139.

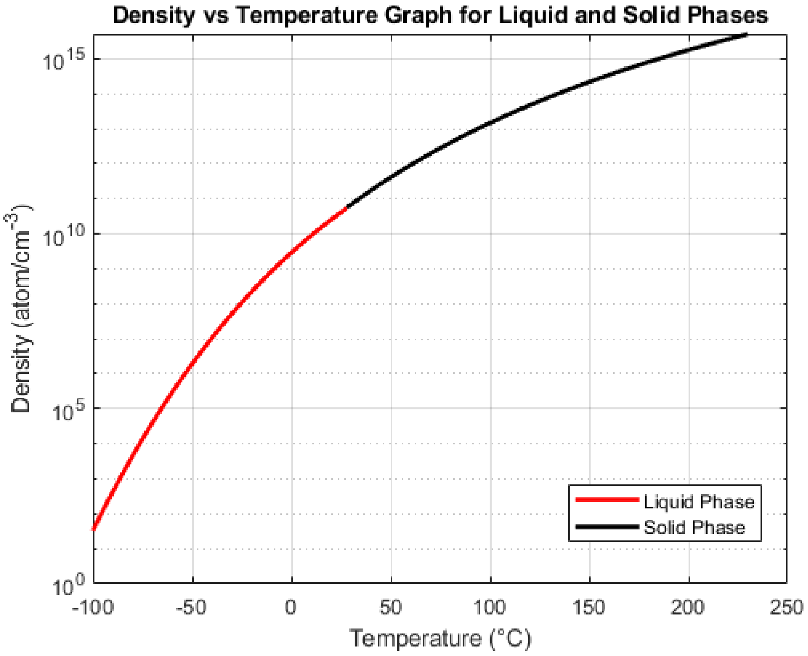

Soucer: The Author, 2024.

5.3 RYDBERG STATES AND SPECTROSCOPIC SCHEME

In cesium atoms, Rydberg states play a pivotal role in advancing our understanding of quantum mechanics and atomic interactions. The figure below delineates the energy levels of cesium that are particularly relevant to our investigations into these intriguing Rydberg states. The figure 23 shows the energy levels of cesium relevant to our experiments: the ground state Cs($6S_{1/2}$), the first excited state Cs($6P_{3/2}$), and all accessible Rydberg states Cs($nS_{1/2}, nD_{3/2}$).

The ground state of cesium, Cs($6S_{1/2}$), has two hyperfine components, $F = 3$ and $F = 4$, which are separated by approximately 9.19 GHz (Steck, 2003). Optical pumping is used to selectively transfer atoms from one hyperfine component, typically $F = 3$, to an excited state, Cs($6P_{1/2}$), by driving the transition $6S_{1/2}(F = 3) \rightarrow 6P_{1/2}(F = 4)$. This process involves using resonant light to preferentially populate certain atomic states, making optical pumping a key technique for preparing atoms in specific quantum states. Once in the excited state, collisions can redistribute the population among the hyperfine components of the $6P_{1/2}$ state, which are separated by 1.17 GHz.

Consequently, when probing Rydberg states from $6P_{1/2}$, resonances for both hyperfine components (F=3 and F=4) are observed, and the separation between the hyperfine components of $nS_{1/2}$ and $nD_{3/2}$ levels is within a few MHz (Steck, 2003). To achieve Rydberg states, it is necessary to use a pumping beam (894 nm) and a probe beam (507 - 513 nm). In our study, we used the probe beam at 512 nm for the state $15D_{3/2}$ and 513 nm for $16S_{1/2}$.

Figure 23 – Step-wise excitation scheme for probing Rydberg state. Pumping from $6S_{1/2}(F=3) \rightarrow 6P_{1/2}(F=4)$ at 894 nm and probing $6P_{1/2}(F=4,3)- \rightarrow nS_{1/2}, nD3_{3/2}(n=15-18)$ at 507 - 513 nm.

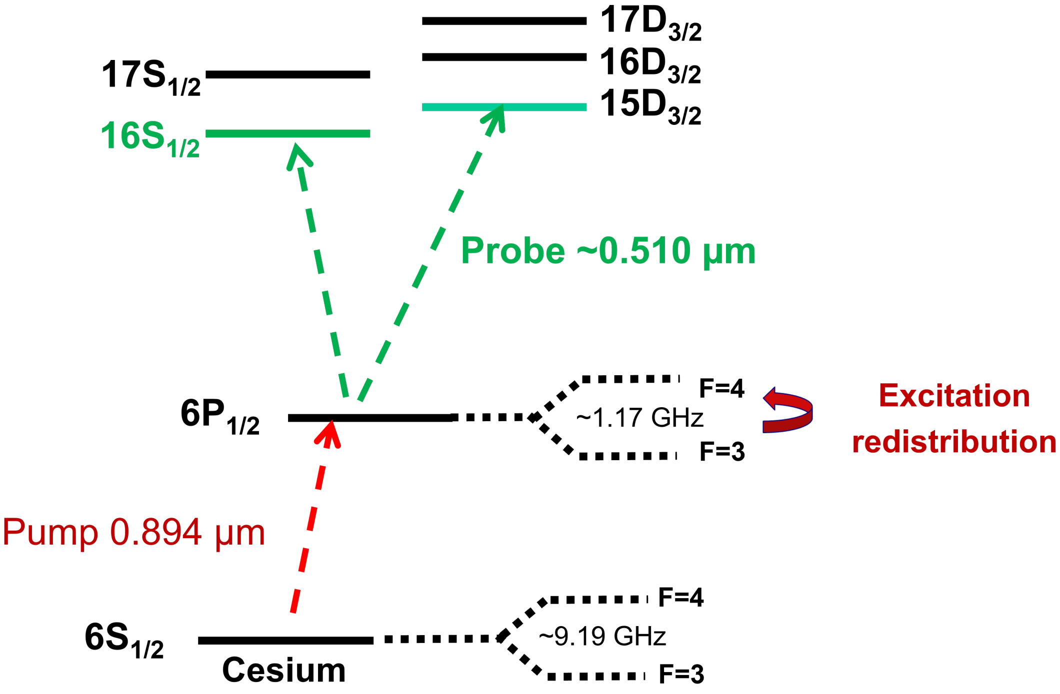

Soucer: The Author, 2024.

Considering the effects of the pumping laser frequency on sequential absorption to the state $6S_{1/2} \rightarrow 15D_{3/2}$, we measured the green laser absorption in the channel $Cs(6P_{1/2}) \rightarrow Cs(15D_{3/2})$ for all four possible pumping configurations (Figure 24). In Figure 24, we observe that when the pumping laser addresses the same hyperfine component for both the ground and excited states of cesium, i.e., for both $6S_{1/2}(F=4) \rightarrow 6P_{1/2}(F=4)$ and $6S_{1/2}(F=3) \rightarrow 6P_{1/2}(F=3)$, the population of the hyperfine component of the excited state that is not directly pumped decreases, showing a dip. Conversely, when the pumping laser addresses different hyperfine components, i.e., for $6S_{1/2}(F=4) \rightarrow 6P_{1/2}(F=3)$ and $6S_{1/2}(F=3) \rightarrow 6P_{1/2}(F=4)$, the population of the excited hyperfine component that is not directly pumped increases, showing a peak.

Figure 24 – Normalized $6P_{1/2} \rightarrow 15D_{3/2}$ absorption spectra. The directly pumped hyperfine component always presents a peak at vz = 0 due to the velocity selection of the pump. The hyperfine component that is not directly pumped presents either a peak (for $6S_{1/2}(F = 4) \rightarrow 6_{P1/2}(F = 4)$ or $6S_{1/2}(F = 3) \rightarrow 6P_{1/2}(F = 3)$ pumping) or a dip (for $6S_{1/2}(F = 4) \rightarrow 6P_{1/2}(F = 3)$ or $6S_{1/2}(F = 3) \rightarrow 6P_{1/2}(F = 4)$ pumping).

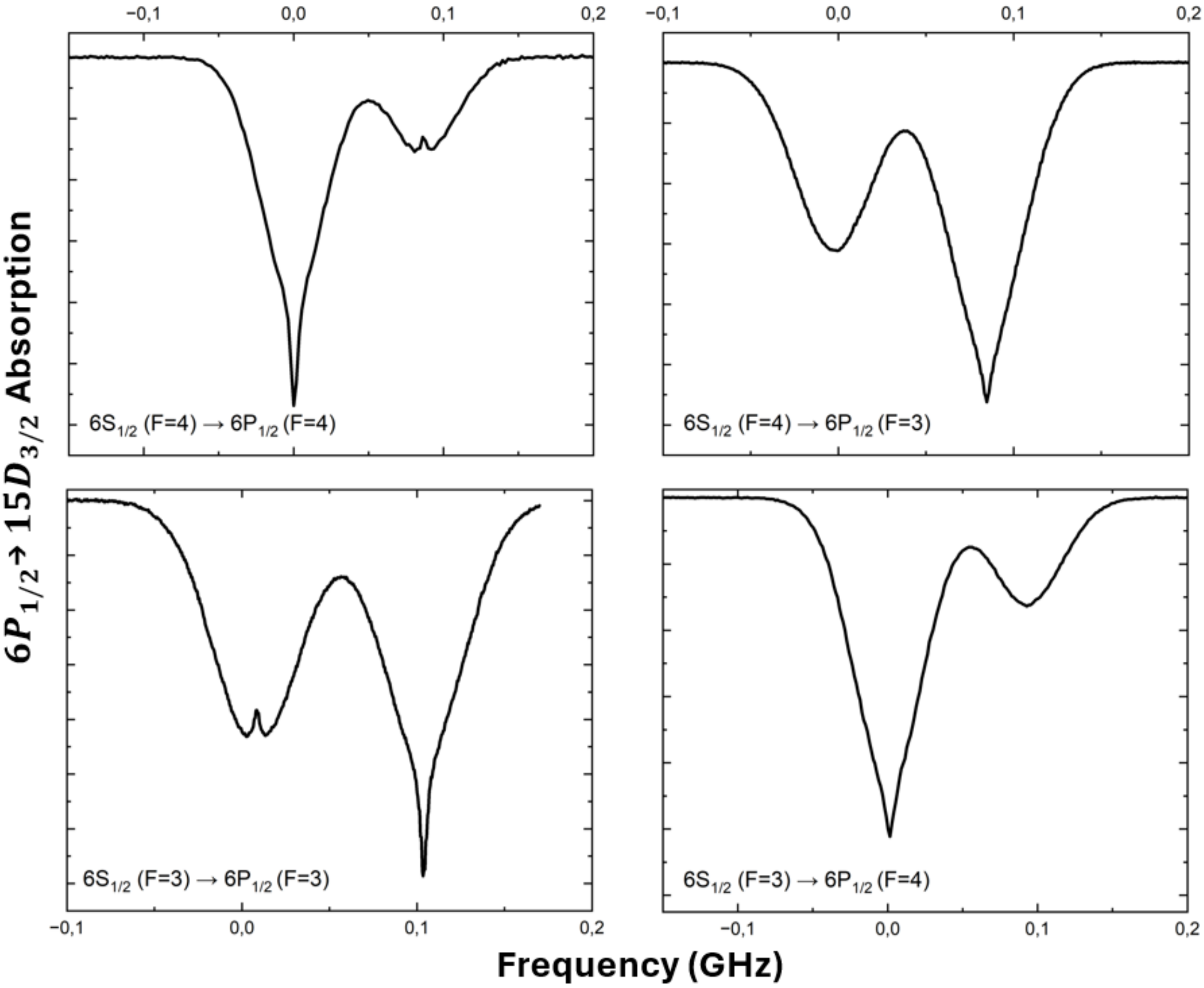

Soucer: The Author, 2024.

5.4 EXPERIMENTAL SETUP

Our experimental setup (figure 25) consists of two diode lasers tuned to the cesium D1 line, with a wavelength of 894 nm. Additionally, we use a green diode laser from TOPTICA as the probe source. This laser has a wavelength range between 507 and 514 nm, with an output power of 25 mW at 512 nm. We employ a green laser tuned to 512 nm for the $15D_{3/2}$ state and 513 nm for the $16S_{1/2}$ state.

The frequency scanning of the probe laser is performed by applying a voltage to the piezoelectric actuator. Furthermore, we use a feed-forward technique (simultaneous scanning of the laser current) to extend the laser's continuous scanning range, avoiding

Figure 25 – Simplified experimental setup with a volumetric cell and thincell

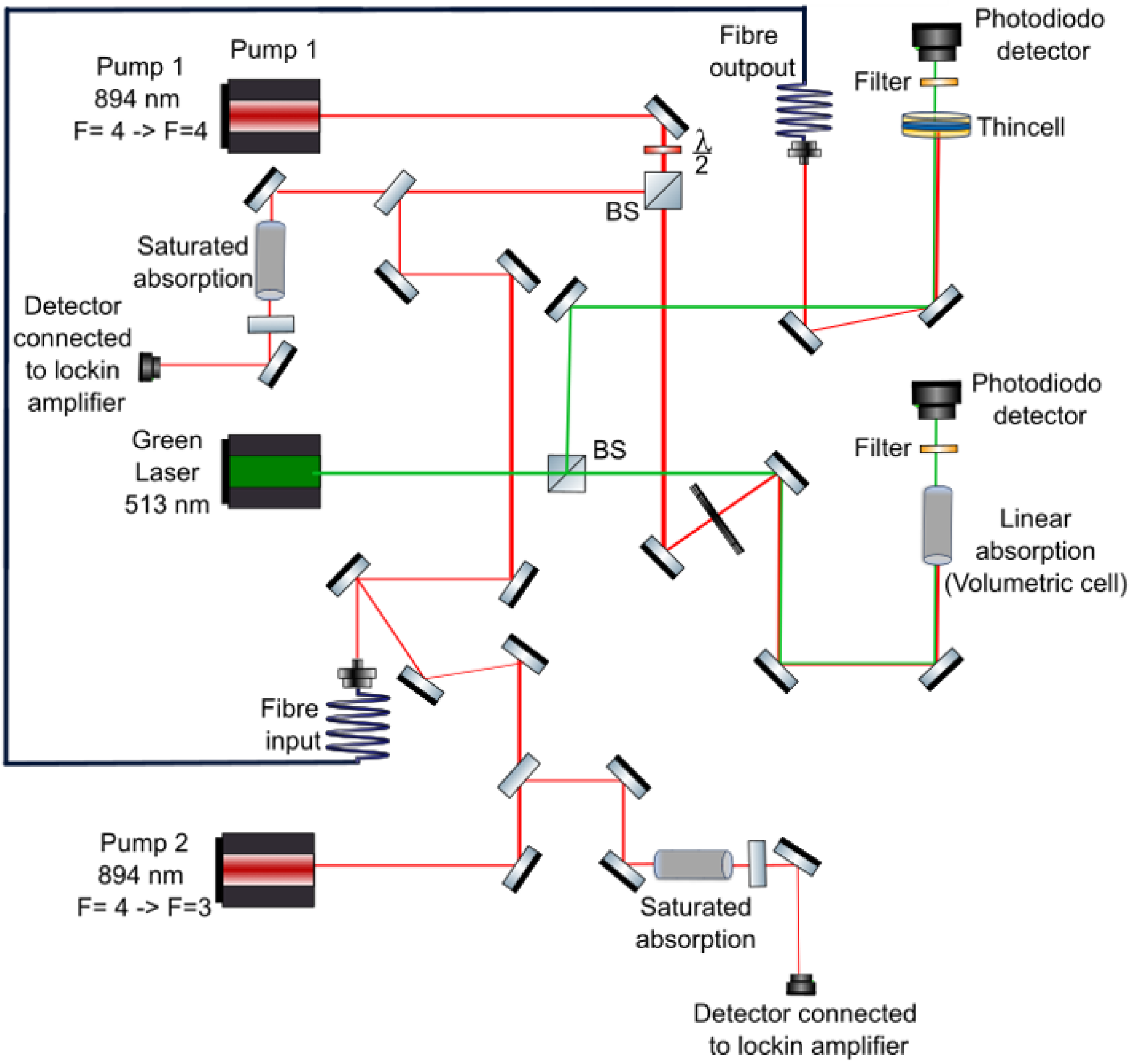

Soucer: The Author, 2024.

jumps, up to approximately 20 GHz. Lock-in amplifiers are used in our experiment, they are equipped with low noise voltage sources and connected to beam controllers.

Figure 26 shows the cesium level scheme and the excitation scheme of the lasers involved in our experiment. The first laser, referred to as "pump 1,"is tuned to the transition $6S_{1/2}$ (F = 4) $\rightarrow 6P_{1/2}$ (F = 4). It is directed into the volumetric cell, where its power of approximately 0.5 mW is applied. Additionally, approximately 4 mW from "pump 1"is used for pumping in the thin cell. The second pumping laser, "pump 2", is tuned to the transition $16S_{1/2}$ (F = 3) $\rightarrow 6P_{1/2}$ (F = 4) and is exclusively used in the thin cell, operating at its full power of around 2 mW.

We utilize the portion of the beam that enters the volumetric cell to obtain a linear absorption spectrum of the transition $6S_{1/2}$ (F = 4) $\rightarrow 6P_{1/2}$ (F = 4). Furthermore, this beam serves as a frequency reference, as it is known from the literature (Rafac; Tanner,

Figure 26 – Excitation scheme of the lasers involved in our experiment. Focusing on pumps lasers that, despite having the same wavelength, are tuned to different transition frequencies.

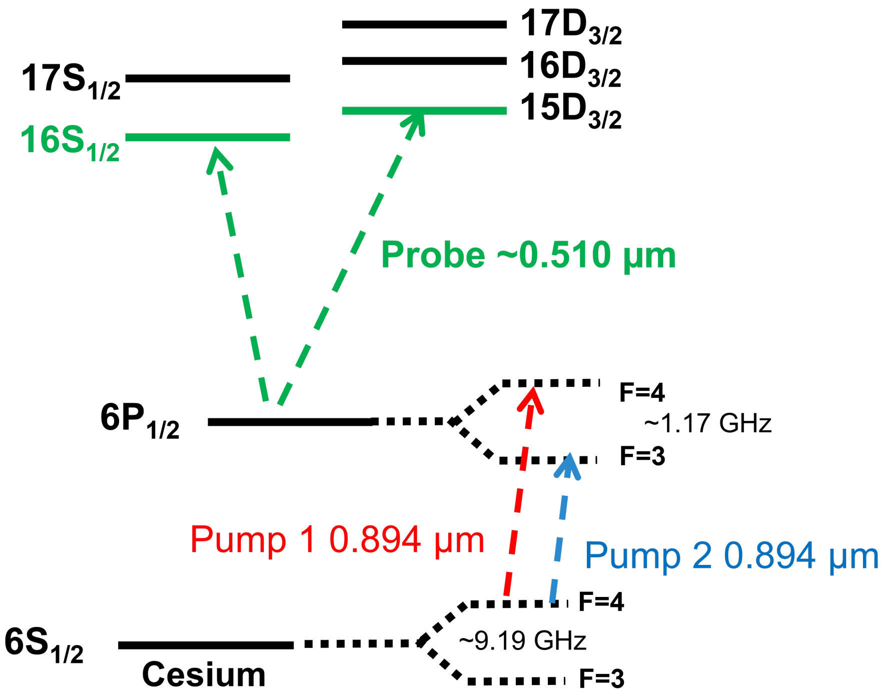

Soucer: The Author, 2024.

1998) that the sub-Doppler components of this transition are spaced by 1.168 GHz (Steck, 2003). To measure the transmission of the green laser, both lasers undergo amplitude modulation before reaching the cells containing cesium vapor. Precise temperature control is achieved using two ovens, maintaining stable temperatures for the cell windows and cesium reservoir.

Figures 27 and 28, respectively illustrate the volumetric cell and the fine cell and they dimensions , shape and temperature control. This configuration allows us to investigate cesium atom properties in optical transitions with precision, while carefully controlling temperature gradients. Specifically, for the volumetric cell, a 50 ℃ temperature difference between the reservoir and windows, whereas for the thin cell, a 100 ℃ gradient between temperatures is necessary.

The cell's heating system is composed of two independent ovens: oven (1) heats the main sapphire window, oven (2) controls the heating of the Cs reservoir and maintains the thermal gradient between the surface and the reservoir.

The cell temperature is measured using two thermocouples: one is touching the side of the sapphire window, the other is in contact with the cesium reservoir. The two furnaces are identical having tungsten filaments as heating elements.

The thin cell (TC) has an biconcave shape as shown in figure 28 with YAG

Figure 27 – Scheme of the cesium volumetric vapour cell. The cell is inside an oven whose temperature we divide between T up and T down, where Tup > Tdown, where Tdown is the temperature that governs the density of Cs.

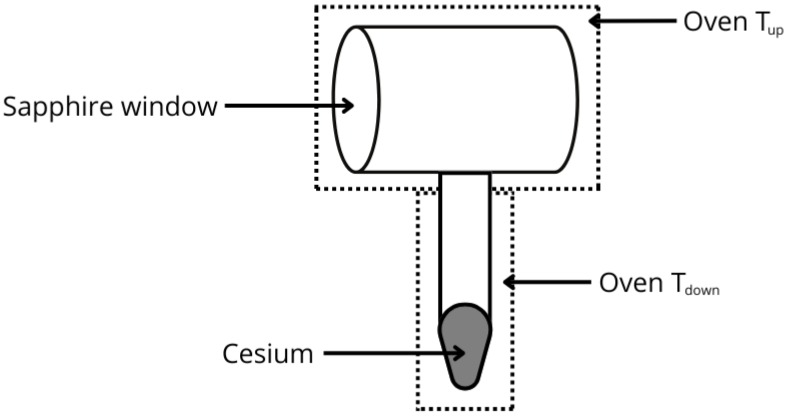

Soucer: The Author, 2024.

windows. After pumping the cell, the YAG windows bend under atmospheric pressure.

Figure 28 – Shape of the cesium vapour thin cell.

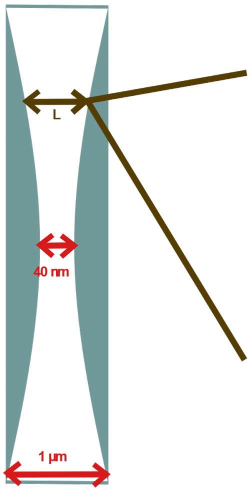

Soucer: The Author, 2024.

This creates a thickness gradient within the cell ranging from $\approx 40nm$ in the center as showed in figure 28, to $\approx 1000nm$ towards the edges of the cell. Different thicknesses can be explored by translation the cell along the X-Y plane.

5.4.1 THICKNESS MEASUREMENT

Thin cell thickness is measured by Fabry-Pérot interferometry. Figure 30 illustrates the path of a laser beam (1) passing through the cell with almost normal incidence. The reflection from the thin cell is denoted as (3) (only one reflection beam is observed

Figure 29 – Scheme of the cesium vapor thin cell.

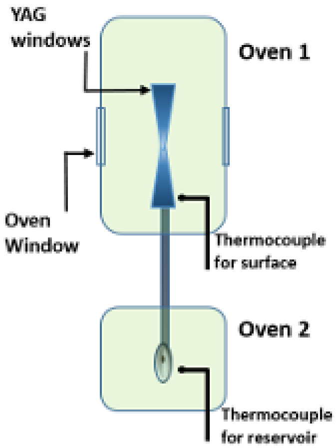

Soucer: Dutta, 2023.

due to the parallelism between the two interfaces forming the cavity of the thin cell), while the reflection from the first window is denoted as (2).

Figure 30 – Transmission path of a near normal incident beam (1) through the thin cell which acts as a low finesse Fabry–Pérot interferometer. Beams indicated by (2) and (3) are the reflected beams from the first window and the thin cell respectively. $\alpha << 1$ is the incident angle which has been deliberately upscaled in the figure for convenience.

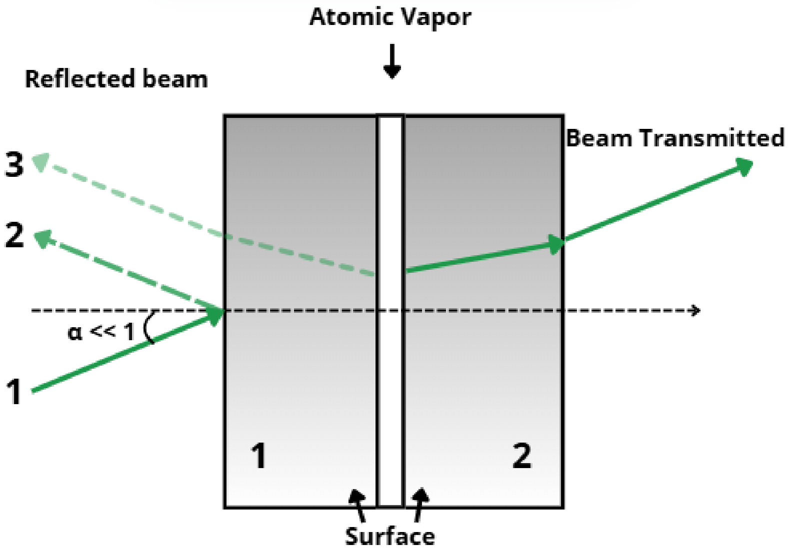

Soucer: The Author, 2024.

An experimental measurement using a single wavelength does not allow us to uniquely determine the cell thickness (Dutier, 2003). To do this, we use 2 lasers of different wavelengths for our thickness measurement (pump outside the resonance and the green test beam). In figure 31 we show a typical measurement of cell thickness using two lasers (894 nm and 512 nm). The two lasers overlap and hit the same point on the cell. Using two different wavelengths in figure 31, we obtain an overlap between the two reflectances for a specific cell thickness of 583 ± 2,5 nm.

Figure 31 – Reflectance R_c as a function of cell thickness (d) (red line: 894 nm, green line: 513 nm). The straight line shows the value of measured reflectance. By using two different wavelengths, we can pinpoint the cell thickness to be 583 ± 2,5 nm.

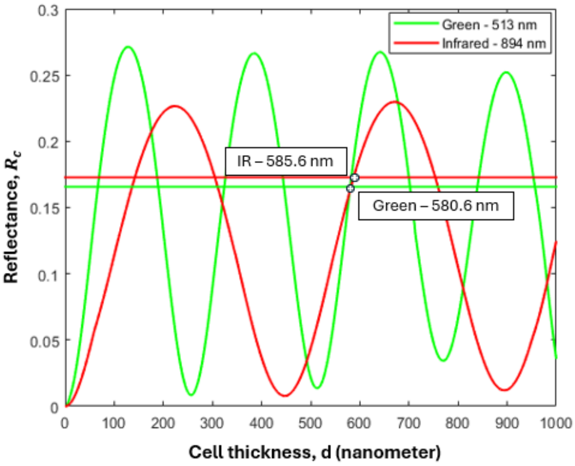

Soucer: The Author, 2024.

5.5 DATA ACQUISITION AND FREQUENCCY SCALE

In our scans, the data acquisition process is controlled by custom software on the laboratory computer. The computer controls a voltage ramp applied to the piezoelectric actuator of the scanning laser to sweep the laser frequency. For each frequency scan point, input signals from photodetectors and lock-in amplifiers are digitized by a DAQ (Data Acquisition) system and recorded on the computer. After a considerable number of scans, these signals are processed in a Matlab program that utilizes the step-by-step absorption signal $6S_{1/2} \rightarrow nS_{1/2}, nD_{3/2}$ to calibrate the frequency scale for each scan. We use the linear absorption peaks of iodine to establish a frequency scale, as the values of these peaks are known from the literature (Gerstenkorn; Luc, 1978). The frequency values are described in the following Table 1 and 2.

Tabela 1 – Green frequency centered on the reference in MHz

16S Iodine absorption peak	Green frequency
153	5.833813974624631e+08
154	5.833835379806132e+08
155	5.833869136436903e+08

Tabela 2 – Green frequency centered on the reference in MHz

15D Iodine absorption peak	Green frequency
434	5.854420389100735e+08
435	5.854492219373672e+08
436	5.854585814579060e+08

The figure 32 shows the linear absorption peaks of iodine for the state $16S_{1/2}$ with the frequency values presented in Table 1. The Matlab program uses an interpolation between voltage and MHz values from (Gerstenkorn; Luc, 1978) to create the frequency scale for the volumetric cell.

Figure 32 – In black, linear absorption of iodine to the wavelength of 512.089 nm to create a frequency scale and in red linear absorption of volumetric cell $6P_{1/2} \to 16S_{1/2}$.

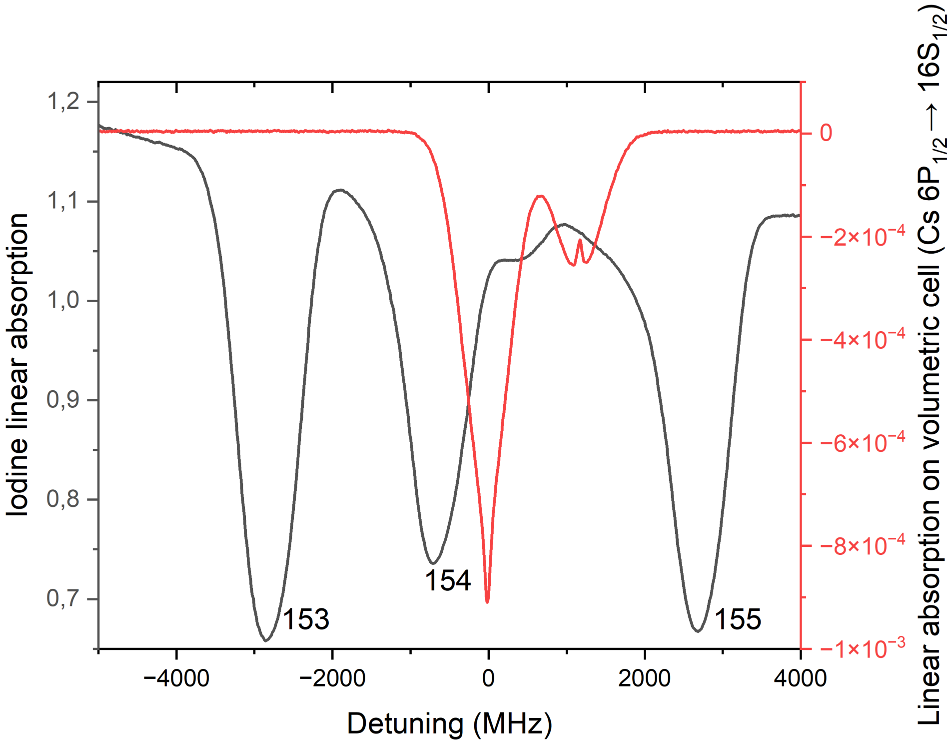

Soucer: The Author, 2024.

However, for the thin cell, in addition to the iodine absorption peak values, a second reference is used—the position of the peaks in the transition $Cs5S_{1/2}$ (F = 4) $\rightarrow$ $Cs6P_{1/2}$ (F = 4). We know that the distance between these two peaks corresponds to 1.168 MHz.During the extended scan time, we verify that the experimental conditions remain unchanged, simultaneously monitoring the stabilization of pump laser frequencies, cell temperature, and probe laser scanning.

5.6 SATURATED ABSORPTION

The analysis of the hyperfine splitting structure in atomic energy levels can be performed without the Doppler broadening effect. This is achieved through saturated absorption spectroscopy. The saturated absorption experiment, illustrated in figure 140, is part of our experimental setup. Besides being crucial in spectroscopy experiments with atomic vapors, it is through this technique that we stabilize our pump lasers at the correct frequency of the transitions. This is a technique of nonlinear interaction of laser light with atoms to achieve spectra of atomic gases free from Doppler broadening and is used in the investigation of sub-Doppler structures. The figure 33 below shows the Doppler effect acting on an atom with a given velocity v:

Figure 33 – Saturated absorption scheme: an atom with velocity ν in a laboratory frame experiences the Doppler Effect, because, when it is in motion, it "perceives"the laser frequency differently.

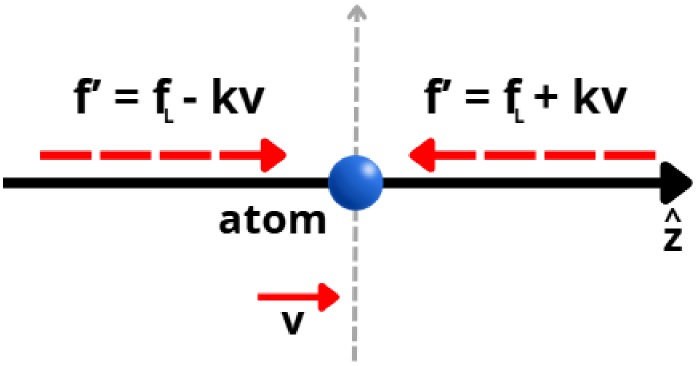

Soucer: The Author, 2024.

For a specific frequency of the incident beam, considering propagation along the "z"direction, the frequency "seen", by each atom varies and depends on the component of its velocity in the direction of the beam:

$$f' = f_L\left(1 \pm \frac{v_z}{c}\right) \tag{140}$$

where f_L is the frequency of the laser, v_z is the component of the atom's velocity in the direction of the beam, the +/- signs are used depending on whether the atom's movement is counter-propagating or co-propagating with the incident beam, respectively, and c is the speed of light in a vacuum. Quantitatively, we can analyze the saturated absorption technique as follows: The Maxwell-Boltzmann distribution for the v_z component of the atom's velocity in the direction of radiation propagation (**??**) is expressed as:

$$f'dv = \left(\frac{1}{u\sqrt{\pi}}\right) \cdot \exp\left(-\frac{1}{2}\nu_z^2 u^2\right) d\nu \tag{141}$$

where,

$$u = \sqrt{\frac{2k_B T}{M}} \tag{142}$$

It is the most probable velocity for atoms in atomic vapors, T is the temperature in kelvin, $k_B = 1.380649 \times 10^{-23}$ is the Boltzmann constant in J/K, and $M = 2.2 \times 10^{-25}$ is the atomic mass of Cs in kg. We use the saturated absorption to tune the LASER frequency to one of the hyperfine transition frequencies of our atom. Basically, the LASER adjusts its frequency around the hyperfine transitions of cesium in the D1 line, with a wavelength of 894 nm. For the LASER to excite the atoms from the ground state to the excited state, it needs to be tuned to the desired transition, which we call being in resonance.

In saturated absorption, two beams are incident in opposite directions in the atomic vapor. One of the beams is called the strong beam (pump) and the other, weaker, is called the probe beam. When the LASER frequency is equal to the atomic transition frequency, both beams interact simultaneously with the same class of atoms with velocity $\nu_z = 0$. The strong beam saturates the atomic transition, reducing the number of atoms with velocity $\nu_z = 0$ in the ground state. Consequently, the absorption of the weak beam decreases because the atoms have already been excited by the strong beam.

The absorption of the probe beam presents a Doppler-broadened profile, from which a Lorentzian peak corresponding to the resonant frequency is subtracted. At this frequency, the atoms absorb the strong beam while the weak beam is transmitted and detected. Figure 34 illustrates the beam arrangement used in saturated absorption.

Figure 34 – Saturated Absorption Setup in our experiment, the arrows inside the cell indicate the different velocities of atoms in atomic vapor. The strong beam is indicated by the letter F and the weak beam indicated by the letter P.

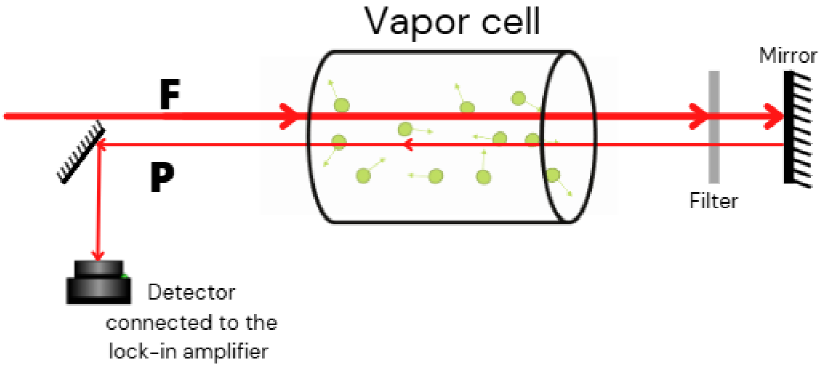

Soucer: The Author, 2024.

We can conclude that Doppler broadening is generally the main contribution to the observed line widths in atomic spectra, especially at room temperature. The integration of all velocity classes results in the absorption coefficient:

$$\kappa(\omega) = \int N(\nu)\sigma(\omega - k\nu)\, d\nu \tag{143}$$

where $\sigma(\omega - k\nu)$ is the absorption cross-section and $N(v)$ is the numerical density of the atoms. At high intensities, the population difference between two levels is reduced as the atoms are excited to the excited state. Thus, we have:

$$\kappa(\omega) = \int_{-\infty}^{+\infty} [N_1(\nu) - N_2(\nu)]V|\sigma_{abs}(\omega - k\nu)|d\nu \tag{144}$$

With $N = N_1 + N_2$ for a two-level system, where N_1 is the atomic density in the ground state and N_2 is the atomic density in the excited state. In saturated absorption spectroscopy, the quantity $N_1(v) - N_2(v)$ is influenced by the interaction with a high-intensity LASER beam. In our experimental setup we have two cells that are performing this saturated absorption experiment. The detection of the weak beam transmission is connected to a lock-in amplifier as shown so that we can lock the laser at the desired transition. Our pump laser 1 is fixed at the transition $6S_{1/2}(F = 4) \rightarrow 6P_{1/2}(F = 4)$ and our pump laser 2 is fixed at the transition $6S_{1/2}(F = 4) \rightarrow 6P_{1/2}(F = 3)$.

6 EXPERIMENTAL STUDY OF VELOCITY REDISTRIBUTION IN EXCITED CESIUM ATOMS VIA COLLISION AND INTERACTION OF RYDBERG ATOMS WITH NANOMETRIC CELLS

Atomic and collision physics explores the interactions between atoms, ions, and electrons (Bader; Essén, 1984), (Bartschat; Kushner, 2016). Among the phenomena of interest in this field, one stands out: the redistribution of velocity for atoms in excited states after collisions (Zielinska, 1985). This work aims to deepen our understanding of this phenomenon by investigating the velocity redistribution of cesium atoms in excited states through collisions (Keramati; Masters; Huennekens, 1988), (Carvalho et al., 2021) and their interaction with cells of varying thickness (Andreeva et al., 2007). In this chapter, we present experimental results obtained in two distinct configurations: volumetric cells and nanometric cells. Our study focuses on cesium atoms and relevant atomic transitions.

6.1 RESULTS VOLUMETRIC CELL

In the volumetric cell, we employed a semiconductor pumping laser with a wavelength of 894 nm, tuned to the cesium D1 line (Steck, 2003). This allowed us to investigate the following transitions:

- Transition between hyperfine states $[F = 4 \rightarrow F = 4]$
- Transition between hyperfine states $[F = 4 \rightarrow F = 3]$
- Transition between hyperfine states $[F = 3 \rightarrow F = 3]$
- Transition between hyperfine states $[F = 3 \rightarrow F = 4]$

The excited state populations were probed using green probe beams with wavelengths of 512 nm for state $(^{15}D_{3/2})$, and 513 nm for state $(^{16}S_{1/2})$. The results revealed a sub-Doppler structure in the mentioned transitions, which varied with laser frequency tuning. In addition, our results also vary according to cell temperature and pumping beam power, as presented below.

6.1.1 PUMP POWER

With a focus on the variation of sub-Doppler structure, previously investigated by (Mikhailov; Boudot; Brazhnikov, 2021), we also studied the hyperfine structure of the D1 line when altering the pump beam power, as shown in Figure 35. The goal of this experiment was to understand how the pump beam power influences the intensity and shape of the sub-Doppler structure. We performed linear absorption measurements of cesium in the transition from $6S_{1/2}$ $(F = 4)$ to $6P_{1/2}$ $(F = 4)$ and $15D_{3/2}$, varying the power of the pump beam at 894 nm, to observe how the intensity of the detected signal varies as the pump power decreases.

Figure 35 – Linear absorption spectrum of cesium for the atomic transition from $6_{1/2}$ (F = 4) to $6P_{1/2}$ (F = 4) and to $15D_{3/2}$, varying the power of the pump beam (894nm).

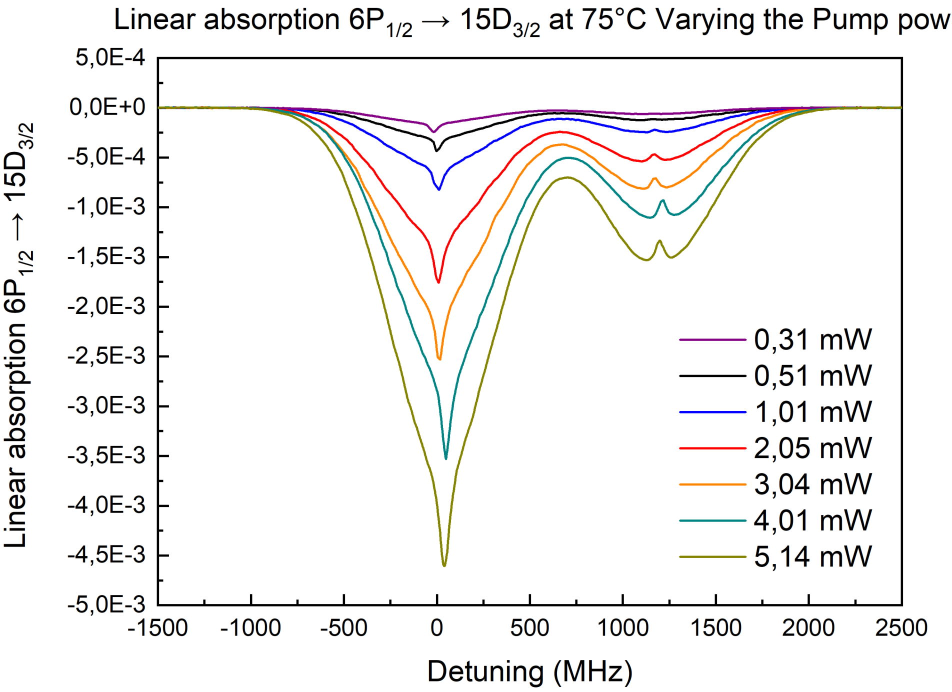

Soucer: The Author, 2024.

We chose to conduct this experiment in the $6S_{1/2}$ $(F = 4)$ to $6P_{1/2}$ $(F = 4)$ configuration because the 4-4 configuration is well-known in the literature (Pitz, 2010) and serves as a reference for frequency scaling in our thin cell experiments. By reducing the pump beam power, we observed a decrease in signal intensity, as well as a reduction in the second (rightmost) sub-Doppler component, shown in figure36.

Figure 36 – Linear absorption spectrum of cesium for the atomic transition from $6_{1/2}$ (F = 3) to $6P_{1/2}$ (F = 4) and to $15D_{3/2}$, varying the power of the pump beam (894nm).

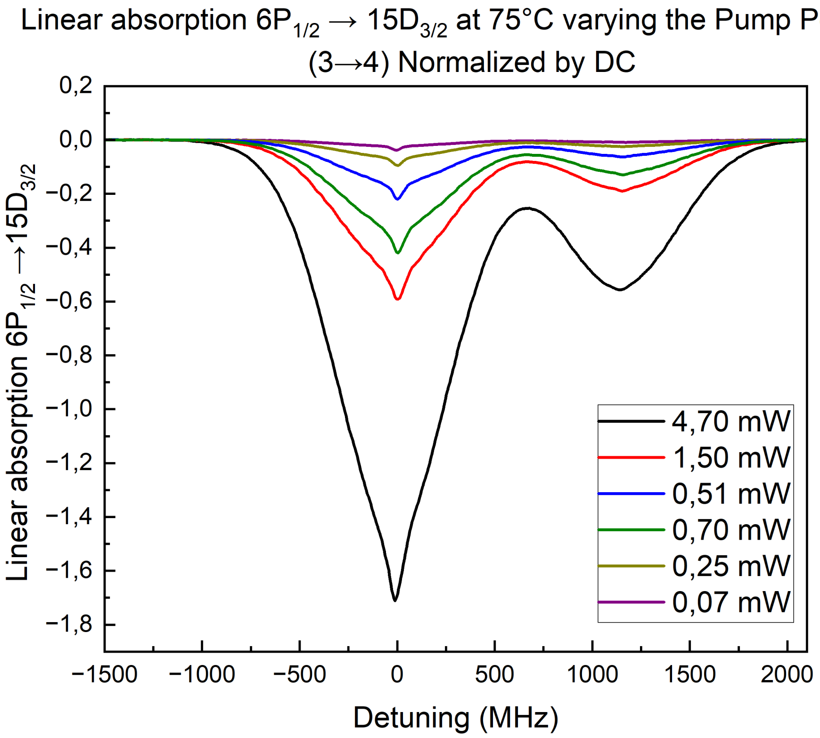

Soucer: The Author, 2024.

Meanwhile, we also performed the same experiment in another configuration, from $6S_{1/2}$ $(F = 3)$ to $6P_{1/2}$ $(F = 4)$ shown in the figure 36. In this case, we noticed not only a decrease in signal intensity at the detector but also a significant change in the first (leftmost) sub-Doppler component when we decreased the pump beam power. Additionally, there was a shift in the Doppler broadening. To illustrate this, we include the following figure 37 showing the normalized signals in the first sub-Doppler component, highlighting the dependence of Doppler broadening on the pump beam intensity.

Figure 37 – Linear absorption spectrum of Cesium for the atomic transition from $6S_{1/2}(F = 3)$ to $6P_{1/2}(F = 4)$ and to $15D_{3/2}$, varying the power of the pump beam and normalized on de 1 ° subdoppler component

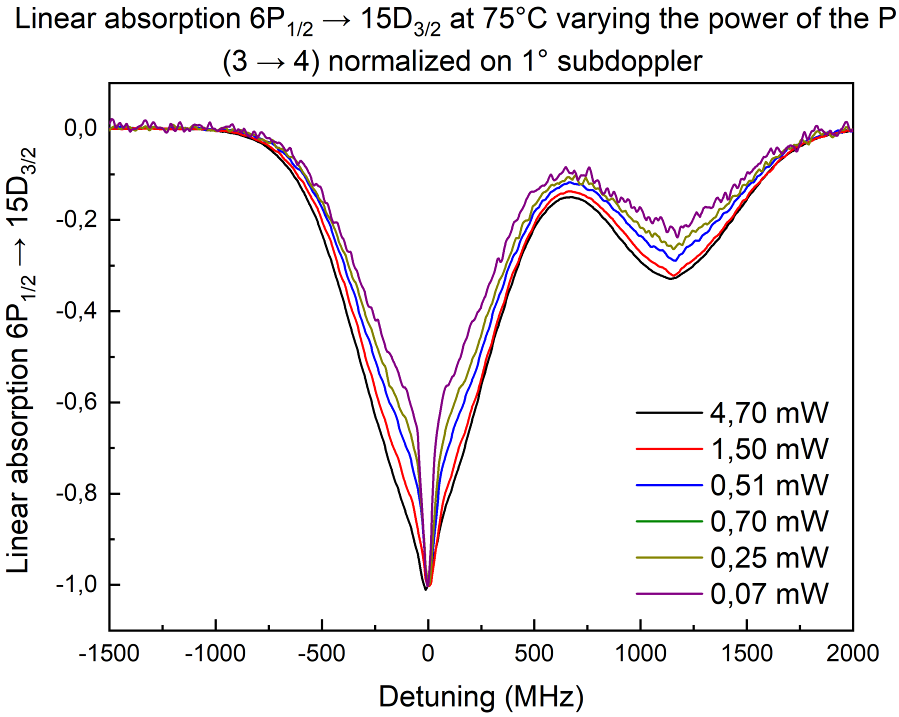

Soucer: The Author, 2024.

It is important to clarify that the signals observed in this work are averages of multiple scans to reduce the amount of noise. When we significantly decreased the pump beam power, the signal became very noisy. Even after adjusting electronic parameters of the experimental system, such as gain, time constant, or phase, it was challenging to separate the signal from the noise. Therefore, our results are limited to a pump power of 0.07 mW.

6.1.2 VARYING THE DENSITY

We also investigated effects related to collisional shift and Doppler broadening in the transition from the state $(6S_{1/2})((F = 4))$ to the state $(6P_{1/2})((F = 4))$, and subsequently to the states $(16S_{1/2})$ and $(15D_{3/2})$. For this investigation, we conducted measurements in the volumetric cell by varying the cell's temperature and, consequently, the density. Our results are given in pressure units (Gallagher, 1994); however, for conversion, the temperature was varied between 423K and 493K, increasing by 10K increments. Similar to previous results, we averaged multiple scans to reduce noise for each chosen experimental configuration, and all data points were placed on our frequency scale. Figure 38 illustrates how the signal intensity varies with atom density in the volumetric cell during the transition from $(6S_{1/2})((F = 4))$ to $(6P_{1/2})((F = 4))$, and subsequently to $(16S_{1/2})$."

Figure 38 – Linear absorption spectrum of Cesium for the atomic transition from $6S_{1/2}$ $(F = 4)$ to $6P_{1/2}$ $(F = 4)$ and to $16S_{1/2}$, at high densities and varying the Temperature of the Volumetric Cell.

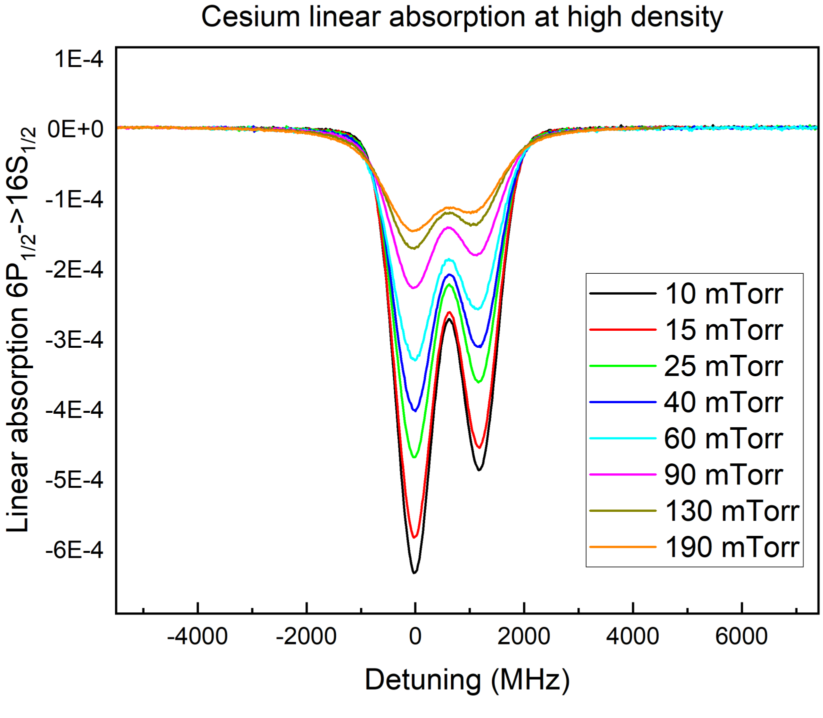

Soucer: The Author, 2024.

Additionally, we observed effects related to a collisional shift during the transition from state $(6S_{1/2})$ $(F = 4)$ to state $(6P_{1/2})$ $(F = 4)$ and subsequently to state $(16S_{1/2})$. The Doppler broadening was also evident in this context. In that experiment, we investigated the effects of cesium atom pressure within a volumetric cell. These effects are related to atom interactions and their influence on spectral lines.

The figure 39 shows the collisional broadening, that occurs when atoms collide during their interaction with light (Chen; Phelps, 1968). These collisions alter the observed spectral line width. In our measurements, we found a collisional broadening value of 3.9 GHz/Torr. This means that the spectral line width is increased due to cesium atom collisions. Understanding this phenomenon is crucial for spectral resolution and measurement precision in atomic systems.

Figure 39 – collisional broadening as a function of the caesium pressure for the transition to $(6S_{1/2})$ $(F = 4)$ to state $(6P_{1/2})$ $(F = 4)$ and subsequently to state $(16S_{1/2})$

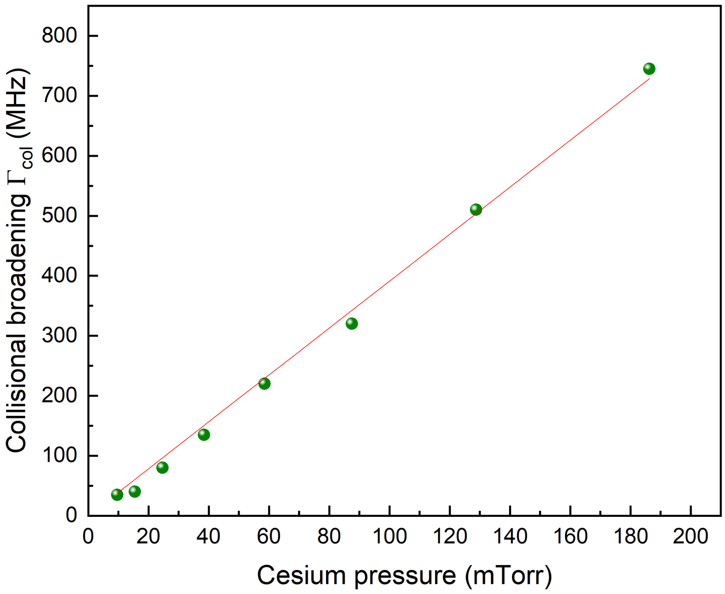

Soucer: The Author, 2024.

On the other hand, the figure 40 shows the collisional shift, that one refers to the displacement of the central frequency of the spectral line caused by atom collisions. We observed a shift of -450 MHz/Torr.

Figure 40 – Collisional shift as a function of the cesium pressure for the transition to $(6S_{1/2})$ $(F = 4)$ to state $(6P_{1/2})$ $(F = 4)$ and subsequently to state $(16S_{1/2})$

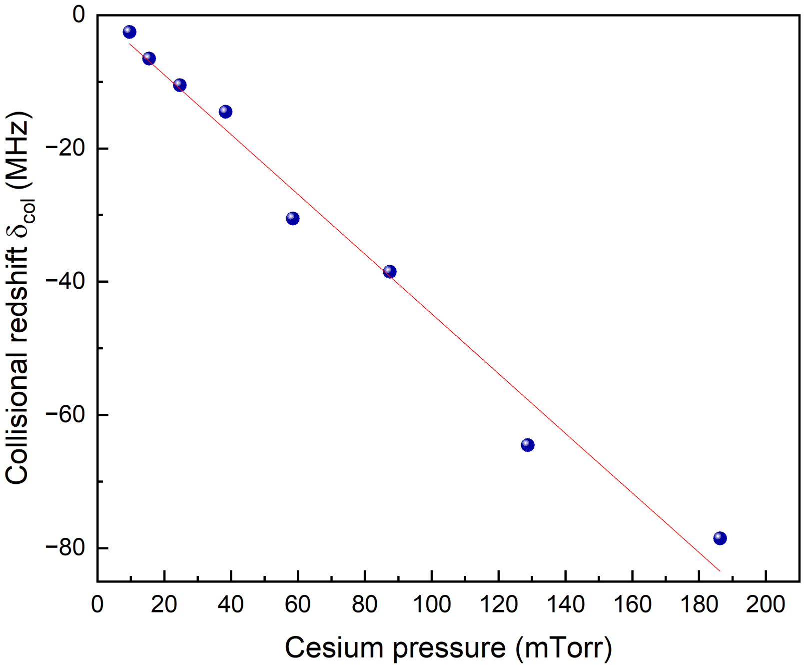

Soucer: The Author, 2024.

This effect is essential for calibrating measurement systems and compensating for deviations caused by collisions. The redshift (lower frequency) is a characteristic feature of this phenomenon (Garrett; Ch’en; Looi, 1967).

For the transition from $6S_{1/2}$ (F = 4) to $6P_{1/2}$ (F = 4) and to $15D_{3/2}$, we also performed measurements varying the temperature of the cell. The goal was to observe if the collisional shift would appear and to investigate changes in the behavior of collisional broadening. We conducted measurements by varying the cell temperature at 430K, 450K, 470K, 480K, and 490K in the volumetric cell. This result is shown in the Figure 41

Figure 41 – Linear absorption spectrum of Cesium for the atomic transition from $6S_{1/2}(F = 4)$ to $6P_{1/2}(F = 4)$ and to $15D_{3/2}$, at high densities and varying the Temperature of the Volumetric Cell.

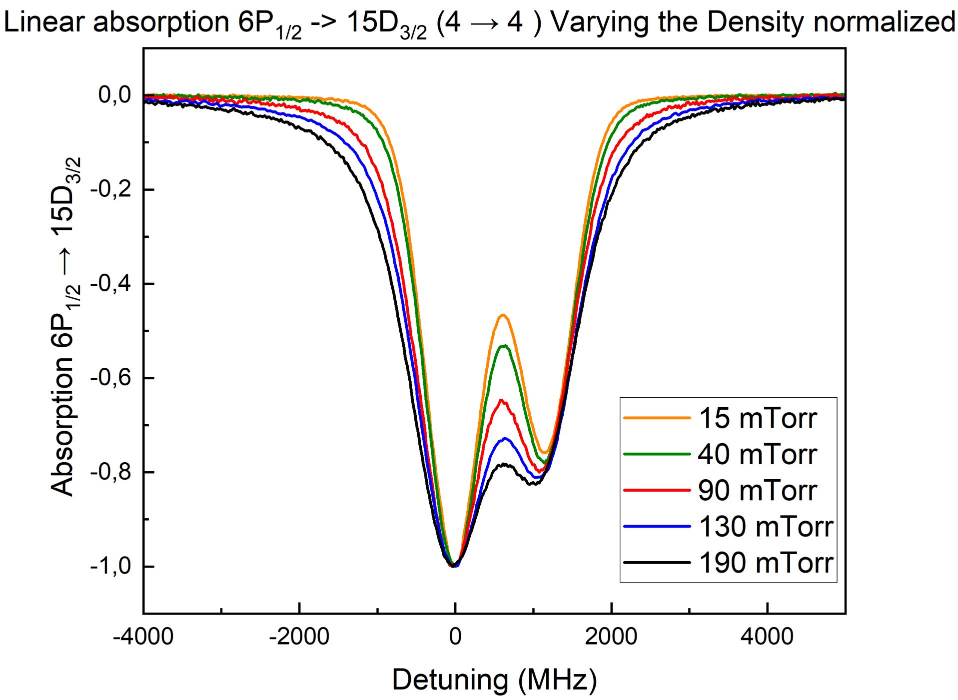

Soucer: The Author, 2024.

Meanwhile, the behavior we observe here is different from what occurred for the $16S_{1/2}$ state. We do not observe the collisional shift, but it is possible to visualize a significant difference graphically in the Doppler increase with increasing pressure, as shown in Figure 42.

Figure 42 – Collisional broadneing as a function of the caesium pressure for the transition to $(6S_{1/2})$ $(F = 4)$ to state $(6P_{1/2})$ $(F = 4)$ and subsequently to state $(15D_{3/2})$.

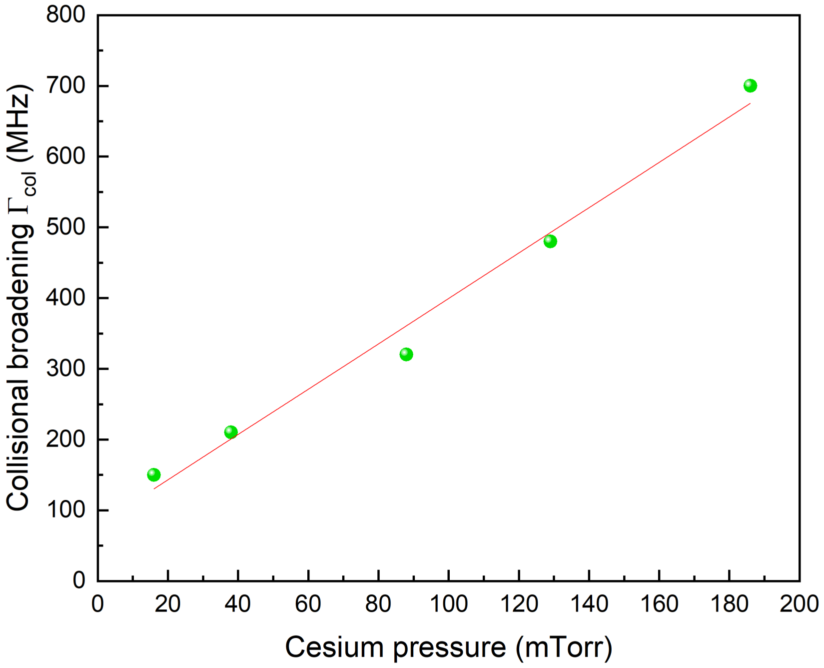

Soucer: The Author, 2024.

The increase in colisional broadening is shown in Figure 42 for the state $15D_{3/2}$, where we obtain a value of 3.20 MHz/mtorr. This indicates that the particles are moving in a way that magnifies the spectral lines. This enlargement can be caused by the thermal movement of the particles (temperature increase) and by frequent collisions between them (pressure increase). We were not able to visualize the shift for the $15D_{3/2}$ state, and an update to our program would be necessary to be able to visualize the shift that exists in this transition, which is a motivation for some ongoing work in the LPL OCR research group.

6.1.3 VARYING THE FREQUENCY

We also conducted an experiment with the goal of understanding the nature of sub-Doppler structure based on the tuned frequency of the pumping laser. The idea behind this experiment was to visualize the signal when the pumping laser is precisely at the 4-4 transition, both with higher and lower frequencies. To achieve this, we performed a scan of saturated cesium absorption using only the pump laser to visualize the two transitions, 4-3 and 4-4, as shown in figure 43, in order to determine the voltage range. Next, we conducted another scan, centering on the 4-4 resonance, allowing us to lock the laser at that frequency.

Figure 43 – Saturated absorption spectrum of Cesium to create a frequency scale, where we visualize the $6S_{1/2}(F=4)$ to $6P_{1/2}(F=3)$ transition on the left and the $S_{1/2}(F=4)$ to $6P_{1/2}(F=4)$ transition on the right

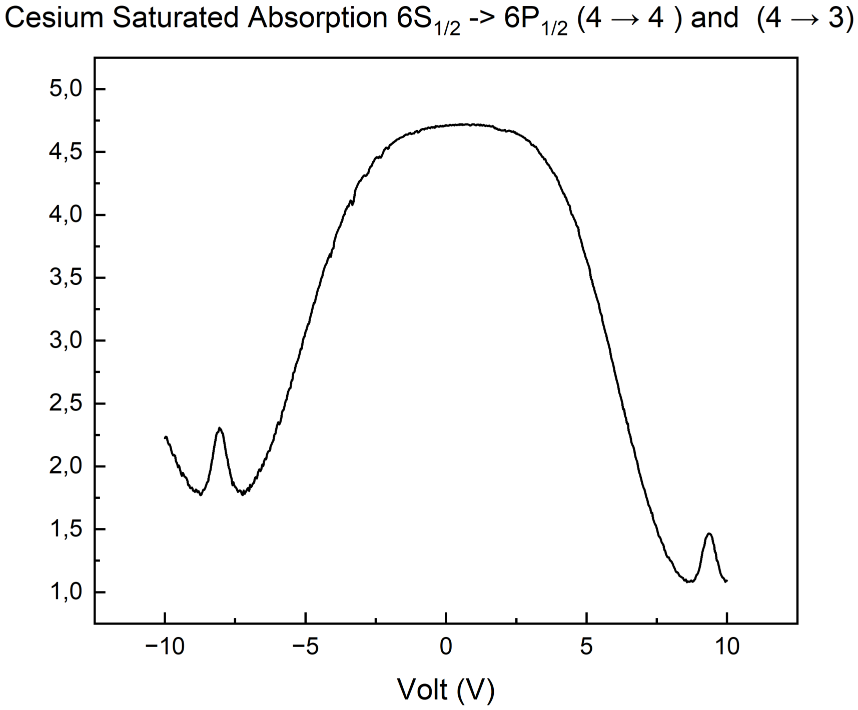

Soucer: The Author, 2024.

Subsequently, we performed a scan with the green laser, but this time we modified the pump frequency by directly adding voltage to the laser controller. This adjustment either increased or decreased the frequency of the pump beam. During the scan shown in figure 44, where we visualize only the $6S_{1/2}(F = 4)$ to $6P_{1/2}(F = 4)$ transition in the cesium saturated absorption, we observed an inverse proportionality between the pump frequency and voltage. To convert voltage to frequency, we established a voltage scale, leveraging our knowledge of the voltage-to-GHz conversion for the two transitions.

Figure 44 – Saturated absorption spectrum of Cesium to create a frequency scale, where the laser is tuned at transition $6S_{1/2}(F = 4)$ to $6P_{1/2}(F = 4)$.

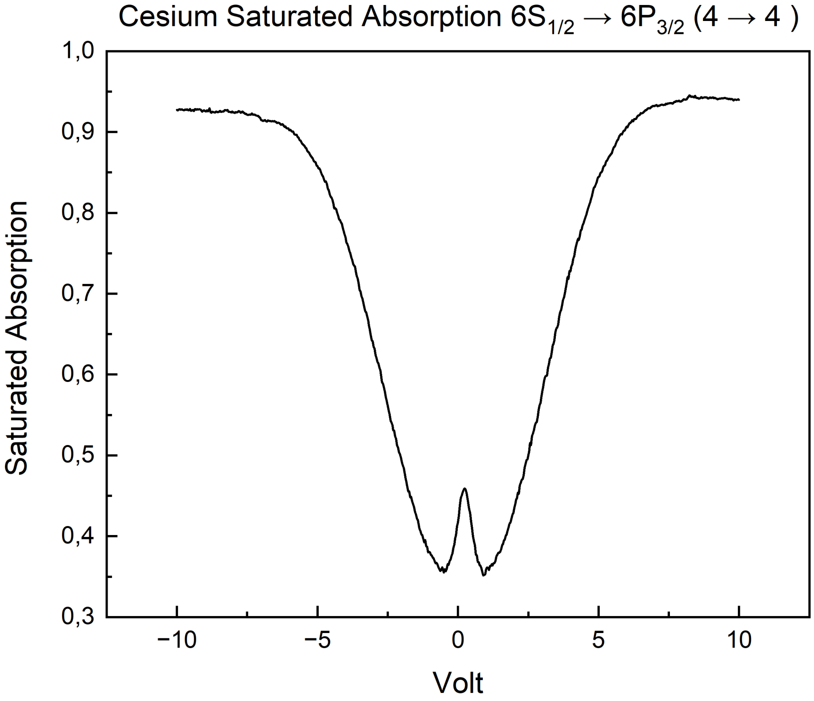

Soucer: The Author, 2024.

Our findings revealed that every 1V change in the controller corresponds to a 67.25 MHz detuning of the pump beam. Using the following equation 145, with the already known wavelength values of the probe beam (green) and the pump beam (Infrared) we estimated the value of the shift (Δ_{probe}) in our green beam based on the shift (Δ_{pump}) applied to the probe beam.

$$\Delta_{\text{probe}} = \frac{\Delta_{\text{pump}} \times \lambda_{\text{pump}}}{\lambda_{\text{probe}}} \tag{145}$$

As a result, we observed a shift in the probe beam of 344 MHz when the pumping beam shift was 354MHz $(\omega + \delta)$, and a shift of 340MHz in the probe beam when the pumping beam shift was -338MHz $(\omega - \delta)$. These results are graphically presented in figure 45

Figure 45 – Linear absorption spectrum of Cesium for the atomic transition normalized $6P1/2- > 15D3/2$ absorption spectra for Pump frequency, on the pump frequency on resonance (Black) when $\omega_I R = \omega_0$, pump frequency $\omega_I R = \omega_0$-δ (Blue) and pump frequency $\omega_I R = \omega_0$+δ (Red).

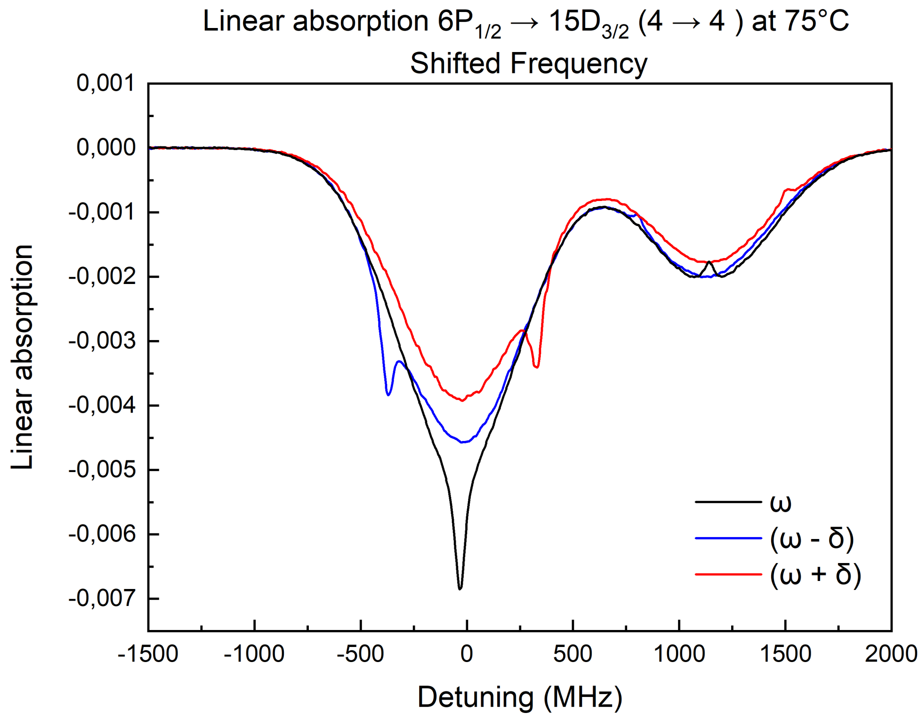
Linear absorption $6P_{1/2} \rightarrow 15D_{3/2}$ (4 → 4) at 75°C
Shifted Frequency

Soucer: The Author, 2024.

6.2 RESULTS THINCELL

Finally, we explored the Rydberg transition from $6P_{1/2} \rightarrow 15D_{3/2}$ in a nanometer-thick cell with thickness ranging from 257 nm to 640 µm. The experimental setup was described in Chapter 4, and we performed our spectroscopic measurement on the transmitted beam of the thin cell.

Biplab Dutta's work (DUTTA, 2023) presented preliminary measurements that focused on probing the transition from $6P_{1/2} \rightarrow 16S_{1/2}$ (at 513 nm). In our measurements, we probed the transition from $6P_{1/2} \rightarrow 15D_{3/2}$ (at 512 nm). Pump lasers 1 and 2 at 894 nm were amplitude-modulated (AM) and locked to transitions $(F = 4 \rightarrow F = 4)$ with pump 1 and $(F = 4 \rightarrow F = 3)$ with pump 2, while the probe beam was directed to the $15D_{3/2}$ state (with a wavelength of 513 nm).

In figure 46, we present all the transmission spectra of thin cells $6P_{1/2} \rightarrow 15D_{3/2}$ obtained and not normalized. With decreasing cell thickness (L), we do not observe a shift towards red or blue atomic resonance, but the homogeneous broadening of line shapes is clearly visible.

Figure 46 – Signal not normalized $6P_{1/2} \rightarrow 15D_{3/2}$ thin cell transmission spectra for various cell thicknesses L at the same cesium vapour pressures

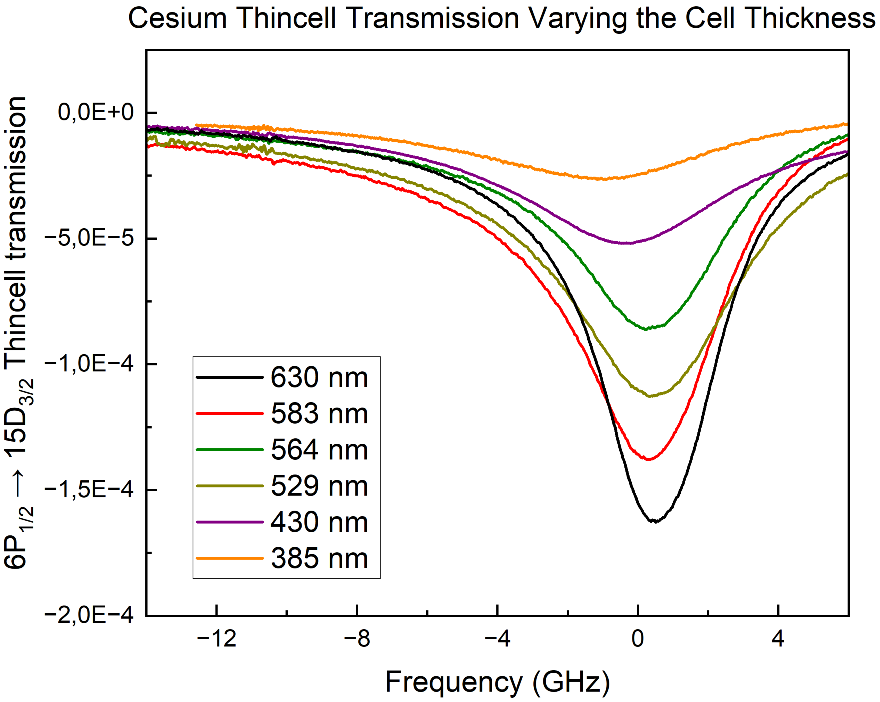

Soucer: The Author, 2024.

From a thickness of 385 nm at 240℃, in orange on the figure 46, the signal intensity becomes very small. Several measurements were taken at each thickness to present the average of various scans at the same temperature and thickness. However, we chose to present the smaller thicknesses separately in figure 47, where we show the transmitted signal of the thin cell with thicknesses of 385 nm, 300 nm, and 257 nm. For the smaller thicknesses, we also did not observe the collisional shift, only the change in the generated signal intensity, in the shape, and broadening of the transition.

Figure 47 – Signal not normalized $6P_{1/2} \rightarrow 15D_{3/2}$ thin cell transmission spectra for spectrum for smaller cell thicknesses L at the same cesium vapour pressures.

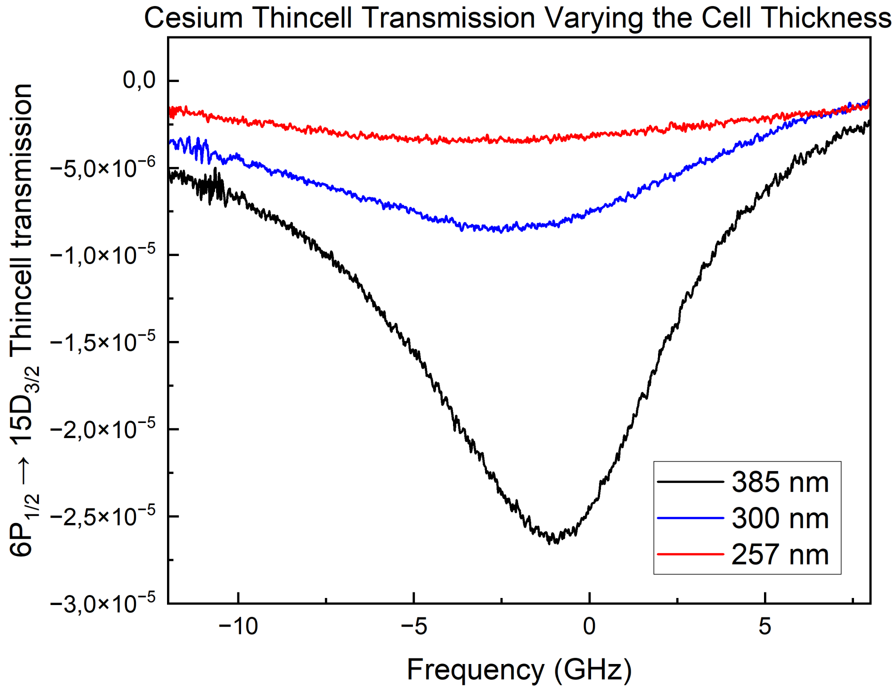

Soucer: The Author, 2024.

In measurements with the volumetric cell, we observed the contribution of two components. However, in the volumetric cell, the contribution of the second hyperfine component is strongly suppressed. (DUTTA, 2023) managed to observe the contribution of the second (small) component in the $6P_{1/2} \to 16S_{1/2}$ transition for large cell thicknesses. This likely occurs because collisions with cell walls dominate interatomic collisional redistribution. However, we did not observe this for the $6P_{1/2} \to 15D_{3/2}$ transition, suggesting that the D orbital is less sensitive to interactions between wall collisions and interatomic collisional redistribution.

7 CONCLUSION

This dissertation presents a comprehensive investigation into two key areas of contemporary optical physics: the theoretical and computational analysis of light propagation in nonlinear photonic structures, and the experimental study of velocity redistribution in excited cesium Rydberg atoms. These two areas are tackled in distinct yet complementary parts of the work, each offering significant insights into different aspects of light-matter interaction.

The first part of the work, spanning Chapters 1 to 3, focuses on the theoretical foundations and simulation of light propagation in Kerr-type nonlinear media. We began with a detailed review of the underlying principles of light manipulation, rooted in Maxwell's equations and the Helmholtz equation, which govern electromagnetic wave propagation. A significant portion of this part dealt with the interaction of light with nonlinear media, where the refractive index is dependent on light intensity.

The Kerr effect, a nonlinear optical phenomenon, plays a central role in our analysis. Through the application of the Split-Step Beam Propagation Method (SSBPM), we simulated the behavior of Gaussian beams in Kerr media. The simulations illustrated key phenomena such as self-focusing, where light beams tend to converge due to an intensity-dependent increase in refractive index, and self-defocusing, where beams diverge under similar conditions with opposite refractive index variations. These effects were rigorously analyzed, and the results showed how they can be harnessed to control beam propagation in nonlinear photonic structures.

One important contribution of this theoretical work is the demonstration of how photonic crystals, with periodic refractive index modulation, can be designed to manipulate light in highly controlled ways. These insights are crucial for developing future photonic devices such as waveguides, filters, and resonators that rely on nonlinear effects to optimize their performance. The computational simulations provide valuable predictions on how these structures can be optimized for specific applications, such as optical communications and all-optical switching.

The second part of the dissertation, covered in Chapters 4 to 6, shifts the focus to an experimental investigation of the velocity redistribution in excited cesium atoms using atom Rydberg spectroscopy. This part of the work was done in collaboration with the OCR research group at LPL, and in these chapters we provide a detailed examination of the dynamics of atomic excitation and the interaction between cesium atoms and external electromagnetic fields.

Rydberg atoms, known for their exaggerated atomic properties such as large orbital radii and extreme sensitivity to external fields, were central to our experimental approach. By using cesium atoms confined in both volumetric and nanometric-thin cells, we investigated the effects of velocity redistribution during atomic collisions and the influence of these interactions on the observed spectral lines. The experimental setup, designed to probe transitions in cesium Rydberg states, enabled us to measure these effects with high precision, allowing for a direct comparison with theoretical models.

One of the key findings of this experimental work is the observation of how collisions between cesium atoms lead to velocity redistribution, which in turn affects the width and shift of spectral lines. This phenomenon is especially significant in environments where atom-atom interactions are enhanced, such as in confined geometries or at high atomic densities. The experimental results from both volumetric and thin cells showed that changes in experimental parameters—such as laser power, atomic density, and laser detuning—affect the degree of velocity redistribution. These findings contribute to a deeper understanding of the role of collisions and Doppler effects in Rydberg spectroscopy, and they offer valuable experimental data that can be used to refine theoretical models of light-matter interaction.

This work successfully integrates both theoretical and experimental approaches to provide a multifaceted exploration of nonlinear optical effects and atomic spectroscopy. The theoretical work on light propagation in Kerr-type media and photonic structures offers new perspectives on how light can be controlled and manipulated in nonlinear environments, with potential applications in photonic devices and optical communication systems.

On the experimental side, the work on cesium Rydberg atoms presents novel insights into velocity redistribution mechanisms, contributing to the broader field of atomic physics and spectroscopy. The experimental findings have implications for understanding fundamental processes in light-matter interaction, particularly in confined atomic systems. This knowledge is not only crucial for applications in quantum technologies, such as quantum information processing, but also for the development of highly sensitive sensors based on Rydberg atoms.

This work makes significant contributions to two distinct yet interrelated areas of optical physics. The theoretical and simulation-based studies provide a framework for future developments in photonic technologies, while the experimental investigations offer valuable insights into atomic behavior in Rydberg states. Together, these two parts form a cohesive body of work that enhances our understanding of both nonlinear optics and atomic spectroscopy, with promising implications for future research and technological applications in fields such as quantum optics, optical communications, and spectroscopy.

REFERENCES

DUTTA, Biplab. [S.l.: s.n.].

ANDREEVA, C. et al. Saturation effects in the sub-doppler spectroscopy of cesium vapor confined in an extremely thin cell. **Physical Review A—Atomic, Molecular, and Optical Physics**, APS, v. 76, n. 1, p. 013837, 2007. DOI: https://doi.org/10.1103/PhysRevA.76.013837. Available in: https://journals.aps.org/pra/abstract/10.1103/PhysRevA.76.013837. Accessed on: May 20. 2024.

BADER, R. F.; ESSÉN, H. The characterization of atomic interactions. **The Journal of chemical physics**, American Institute of Physics, v. 80, n. 5, p. 1943–1960, 1984. DOI: https://doi.org/10.1063/1.446956. Available in: https://pubs.aip.org/aip/jcp/article-abstract/80/5/1943/316221/The-characterization-of-atomic. Accessed on: June 28. 2024.

BALL, G.; MOREY, W. Compression-tuned single-frequency bragg grating fiber laser. **Optics letters**, Optica Publishing Group, v. 19, n. 23, p. 1979–1981, 1994. DOI: https://doi.org/10.1364/OL.19.001979. Available in: https://opg.optica.org/ol/abstract.cfm?uri=ol-19-23-1979. Accessed on: Oct 04. 2023.

BARTSCHAT, K.; KUSHNER, M. J. Electron collisions with atoms, ions, molecules, and surfaces: Fundamental science empowering advances in technology. **Proceedings of the National Academy of Sciences**, National Acad Sciences, v. 113, n. 26, p. 7026–7034, 2016. DOI: https://doi.org/10.1073/pnas.1606132113. Available in: https://www.pnas.org/doi/full/10.1073/pnas.1606132113. Accessed on: June 20. 2024.

BERMAN, P.; HAVERKORT, J.; WOERDMAN, J. Collision kernels and transport coefficients. **Physical Review A**, APS, v. 34, n. 6, p. 4647, 1986. DOI: https://doi.org/10.1103/PhysRevA.34.4647. Available in: https://journals.aps.org/pra/abstract/10.1103/PhysRevA.34.4647 .Accessed on: Mar 17, 2024.

BERMAN, P. R. Effects of collisions on linear and non-linear spectroscopic line shapes. **Physics Reports**, Elsevier, v. 43, n. 3, p. 101–149, 1978. DOI: https://doi.org/10.1016/0370-1573(78)90018-2. Available in: https://www.sciencedirect.com/science/article/abs/pii/0370157378900182. Accessed on: Mar 17, 2024.

BETEROV, I.; RYABTSEV, I.; TRETYAKOV, D.; BEZUGLOV, N.; EKERS, A. Ionization of ns, np, and nd lithium, potassium, and cesium rydberg atoms by blackbody radiation. **Journal of Experimental and Theoretical Physics**, Springer, v. 107, p. 20–27, 2008. DOI:https://doi.org/10.1134/S1063776108070029. Available in: https://link.springer.com/article/10.1134/S1063776108070029. Accessed on: Nov 30. 2023.

BOYD, R. W.; GAUTHIER, D. J. Controlling the velocity of light pulses. **Science**, v. 326, n. 5949, p. 1074–1077, 2010. DOI https://doi.org/10.1103/PhysRevA.66.063816.

Available in: https://www.science.org/doi/abs/10.1126/science.1170885. Accessed on: Nov 20. 2023.

BRAGG, W. H.; BRAGG, W. L. The reflection of x-rays by crystals. **Proceedings of the Royal Society of London. Series A, Containing Papers of a Mathematical and Physical Character**, The Royal Society London, v. 88, n. 605, p. 428–438, 1913. DOI: https://doi.org/10.1098/rspa.1913.0040. Available in: https://royalsocietypublishing.org/doi/epdf/10.1098/rspa.1913.0040. Accessed on: Oct 20. 2023.

BYKOV, V. P. Spontaneous emission in a periodic structure. **Soviet Journal of Experimental and Theoretical Physics**, v. 35, p. 269, 1972. DOI: https://doi.org/10.1070/QE1975v004n07ABEH009654. Available in: https://iopscience.iop.org/article/10.1070/QE1975v004n07ABEH009654/meta. Accessed on: Oct 15. 2023.

CARVALHO, J. de A.; MAURIN, I.; FAILACHE, H.; BLOCH, D.; LALIOTIS, A. Velocity preserving transfer between highly excited atomic states: black body radiation and collisions. **Journal of Physics B: Atomic, Molecular and Optical Physics**, IOP Publishing, v. 54, n. 3, p. 035203, 2021. DOI: https://doi.org/10.1088/1361-6455/abd532. Available in: https://iopscience.iop.org/article/10.1088/1361-6455/abd532. Accessed on: May 20. 2024.

CHEN, C.; PHELPS, A. Self-broadening of cesium resonance lines at 8521 and 8944 å. **Physical Review**, APS, v. 173, n. 1, p. 62, 1968. DOI: https://doi.org/10.1103/PhysRev.173.62. Available in: https://journals.aps.org/pr/abstract/10.1103/PhysRev.173.62. Accessed on: May 16. 2024.

CHEN, Z.; SEGEV, M.; CHRISTODOULIDES, D. N. Optical spatial solitons: historical overview and recent advances. **Reports on Progress in Physics**, v. 75, n. 8, p. 086401, 2012. DOI: https://doi.org/10.1088/0034-4885/75/8/086401. Available in: {https://iopscience.iop.org/article/10.1088/0034-4885/75/8/086401}{https: //iopscience.iop.org/article/10.1088/0034-4885/75/8/086401} Accessed on: nov 20. 2023.

CIURYŁO, R.; SZUDY, J. Speed-dependent pressure broadening and shift in the soft collision approximation. **Journal of Quantitative Spectroscopy and Radiative Transfer**, Elsevier, v. 57, n. 3, p. 411–423, 1997. DOI: https://doi.org/10.1016/S0022-4073(96)00078-7. Available in: https://www.sciencedirect.com/science/article/abs/pii/S0022407396000787. Accessed on: Mar 10. 2024.

CONWAY, J. T.; COHL, H. S. Exact fourier expansion in cylindrical coordinates for the three-dimensional helmholtz green function. **Zeitschrift für angewandte Mathematik und Physik**, Springer, v. 61, p. 425–443, 2010. DOI: https://doi.org/10.1007/s00033-009-0039-6. Avalaible: https://link.springer.com/article/10.1007/s00033-009-0039-6. Accessed on: oct 10. 2023.

DEMTRÖDER, W. **Molecular physics: theoretical principles and experimental methods**. [S.l.]: John Wiley & Sons, 2008. DOI: https://doi.org/10.1002/anie.200585402.

Available in: https://onlinelibrary.wiley.com/doi/10.1002/anie.200585402. Accessed on: Mar 18. 2024.

DUTIER, G. **Cavité nanométrique de vapeur de Césium: spectroscopie à haute résolution et interaction de surface de type van der Waals**. Tese (Doutorado) — Université Paris-Nord-Paris XIII, 2003. Available in: https://theses.hal.science/tel-00583452/. Accessed on: May 15. 2024.

DUTTA, B. **Probing cesium Rydberg atoms close to a sapphire surface**. Tese (Doutorado) — Université Sorbonne Paris Nord, 2023. Available in: https://hal.science/tel-04588211/. Accessed on: May 20. 2024.

ECKERT, M. Max von laue and the discovery of x-ray diffraction in 1912. **Annalen der Physik**, WILEY-VCH Verlag Berlin, v. 524, n. 5, p. A83–A85, 2012. Available in: https://www.xtal.iqf.csic.es/Cristalografia/archivos_10/laue-experiment.pdf. Accessed on: Oct 18. 2023.

FIBICH, G. **The nonlinear Schrödinger equation**. [S.l.]: Springer, 2015. v. 192. DOI: https://doi.org/10.1007/978-3-319-12748-4 Available in: {https://link.springer.com/book/10.1007/978-3-319-12748-4}{https: //link.springer.com/book/10.1007/978-3-319-12748-4}ccessed on: oct 27, 2023.

GALLAGHER, T. F. Rydberg atoms. In: **Springer Handbook of Atomic, Molecular, and Optical Physics**. [S.l.]: Springer, 1994. p. 231–240. DOI: https://doi.org/10.1007/978-3-030-73893-8_15 Available in:

GARRETT, R. O.; CH'EN, S. Y.; LOOI, E. C. Pressure effects of foreign gases on the absorption lines of cesium. iv. the effects of neon. **Physical Review**, APS, v. 156, n. 1, p. 48, 1967. DOI: https://doi.org/10.1103/PhysRev.156.48 Available in: https://journals.aps.org/pr/abstract/10.1103/PhysRev.156.48 Accessed on: May 20. 2024.

GERSTENKORN, S.; LUC, P. **ATLAS DU SPECTRE D ABSORPTION DE LA MOLECULE D IODE**. [S.l.]: Editions du Centre National de la Recherche Scientifique (CNRS), 1978. Available in: https://ui.adsabs.harvard.edu/abs/1978adsa.book.....G/abstract. Accessed on: May 30. 2024.

GOUVEIA, E. J. T. d. A. **Mistura de ondas em meio Kerr e bi-estabilidade óptica em filmes**. Tese (Doutorado) — Universidade de São Paulo, 2016. Available in: http://www.teses.usp.br/teses/disponiveis/54/54132/tde-28042014-142147/. Accessed on: Oct 15, 2023.

HAVERKORT, J.; WOERDMAN, J. Rate equations for light-induced drift. **Annalen der Physik**, v. 502, n. 7, p. 519–538, 1990. DOI: https://doi.org/10.1103/PhysRevA.38.4054. Available in: https://journals.aps.org/pra/abstract/10.1103/PhysRevA.38.4054. Accessed on: March 18. 2024.

HERMANS, L. J. F.; KOKS, J.; HENGEVELD, A.; KNAAP, H. The heat conductivity of polyatomic gases in magnetic fields. **Physica**, Elsevier, v. 50, n. 3, p. 410–432, 1970. DOI: https://doi.org/10.1016/0031-8914(70)90261-2. Available in: https://www.sciencedirect.com/science/article/pii/0031891470902612. Accessed on: 27 Mar. 2024.

HINDMARSH, W. R.; FARR, J. M. Collision broadening of spectral lines by neutral atoms. **Progress in Quantum Electronics**, Elsevier, v. 2, p. 141–214, 1973. DOI: https://doi.org/10.1016/0079-6727(73)90005-0. Available in: https://www.sciencedirect.com/science/article/abs/pii/0079672773900050. Accessed on: 25 Mar. 2024.

HINDMARSH, W. R.; PETFORD, A.; SMITH, G. Interpretation of collision broadening and shift in atomic spectra. **Proceedings of the Royal Society of London. Series A. Mathematical and Physical Sciences**, The Royal Society London, v. 297, n. 1449, p. 296–304, 1967. DOI: https://doi.org/10.1098/rspa.1967.0068. Available in: https://royalsocietypublishing.org/doi/abs/10.1098/rspa.1967.0068. Accessed on: 20 Mar. 2024.

HO, T.-S.; WANG, K.; CHU, S.-I. Floquet-liouville supermatrix approach: Time development of density-matrix operator and multiphoton resonance fluorescence spectra in intense laser fields. **Physical Review A**, APS, v. 33, n. 3, p. 1798, 1986. DOI: https://doi.org/10.1103/PhysRevA.33.1798. Available in: https://journals.aps.org/pra/abstract/10.1103/PhysRevA.33.1798. Accessed on: Oct 05. 2023.

JACKSON, J. D. **Classical electrodynamics**. [S.l.]: John Wiley & Sons, 2021. Available in: https://www.perlego.com/book/3865737/classical-electrodynamics-pdf Accessed on: Oct 10. 2023.

JOHN, D. J.; JOANNOPOULOS, D.; WINN, J. N.; MEADE, R. D. Photonic crystals: molding the flow of light. **InPrinceton University of Press**: Princeton, NJ, USA, 2008. DOI: https://doi.org/10.1515/9781400828241. Available in: https://www.degruyter.com/document/doi/10.1515/9781400828241/html. Accessed on: Oct 20. 2023.

JOHN, S. Strong localization of photons in certain disordered dielectric superlattices. **Physical review letters**, APS, 1987. DOI: https://doi.org/10.1103/PhysRevLett.58.2486. Available in: https://journals.aps.org/prl/abstract/10.1103/PhysRevLett.58.2486. Accessed on: Oct 10, 2023.

KERAMATI, B.; MASTERS, M.; HUENNEKENS, J. Excitation-transfer collisions in cesium vapor: Cs (5 d 5/2)+ cs (6 s 1/2)→ cs (5 d 3/2)+ cs (6 s 1/2). **Physical Review A**, APS, v. 38, n. 9, p. 4518, 1988. DOI: https://doi.org/10.1103/PhysRevA.38.4518. Available in: https://journals.aps.org/pra/abstract/10.1103/PhysRevA.38.4518. Accessed on: May 15. 2024.

KLEINMAN, D. A. Theory of second harmonic generation of light. **Physical Review**, APS, v. 128, n. 4, p. 1761, 1962. DOI: https://doi.org/10.1103/PhysRev.128.1761. Available in: {https://journals.aps.org/pr/abstract/10.1103/PhysRev.128.1761}{https://journals.aps.org/pr/abstract/10.1103/PhysRev.128.1761}ccessed on: oct 14. 2023.

KOLCHENKO, A.; PUKHOV, A.; RAUTIAN, S.; SHALAGIN, A. Effect of selective collisions on the velocity distribution of atoms and on nonlinear interference effects. **Sov. Phys. JETP**, v. 36, p. 619–628, 1973. Available in: https://www.osti.gov/biblio/4606208 Accessed on: May 05, 2024.

LIU, C.-S.; SHIH, W.-Y.; LI, Y.-C.; TZENG, Y.-C. Design of thicknesses and refractive indexes measurement system combined with auto-focus system for multilayer transparent samples. **Optics & Laser Technology**, Elsevier, v. 177, p. 111188, 2024. DOI: https://doi.org/10.1016/j.optlastec.2024.111188. Available in: https://doi.org/10.1016/j.optlastec.2024.111188. Accessed on: May 20. 2023.

LOPES, M. V. P. **Acopladores de cristais fotônicos e acesso múltiplo por divisão de código óptico (OCDMA) com pulsos ultracurtos em fibras de Bragg**. Dissertação (Mestrado) — Universidade Federal do Ceará, 2012. Available in: http://repositorio.ufc.br/handle/riufc/2319. Accessed on: Nov 25. 2023.

MALDONADO, E. P.; JUNIOR, N. D. V. **Dispositivos acustico-opticos aplicados a modulação da potencia intracavidade de lasers continuamente bombeados**. Dissertação (Mestrado) — Universidade de São Paulo, 1991. Available in: https://repositorio.usp.br/item/000734472. Accessed on: Nov 20. 2023.

MCCOURT, F. R.; LIU, W.-K. Anisotropic intermolecular potentials and transport properties in polyatomic gases. **Faraday Discussions of the Chemical Society**, Royal Society of Chemistry, v. 73, p. 241–256, 1982. Available in: https://doi.org/10.1039/DC9827300241 Accessed on: May 05, 2024.

MELO, Rosália Luana de Oliveira Silva et al. **estudo de propagação de luz em meio kerr utilizando um material fotorrefrativo**. 2022. Available in:http://www.repositorio.ufal.br/jspui/handle/123456789/12221. Accessed on: Nov 25. 2023.

MIKHAILOV, A.; BOUDOT, R.; BRAZHNIKOV, D. Line shape of the sub-doppler resonance in alkali-metal atomic vapors in the field of counterpropagating bichromatic laser beams. **Journal of Experimental and Theoretical Physics**, Springer, v. 133, n. 6, p. 696–710, 2021. DOI: https://doi.org/10.1134/S106377612112013X. Available in: https://link.springer.com/article/10.1134/S106377612112013X. Accessed on: May 16. 2024.

NIENHUIS, G. Impressed by light: Mechanical action of radiation on atomic motion. **Physics Reports**, Elsevier, v. 138, n. 3, p. 151–192, 1986. DOI: https://doi.org/10.1016/0370-1573(86)90035-9. Available in: https://www.sciencedirect.com/science/article/abs/pii/0370157386900359. Accessed on: Oct 07. 2023.

OLIVEIRA, A. **Estudos em Atomos de Rydberg Frios**. Tese (Doutorado) — Tese de Doutorado, UFSCar, 2001. Available in: https://oasisbr.ibict.br/vufind/Record/BRCRIS_c91aede035c2afe002969fe3f70f31eb?lng=en. Accessed on: Mar 11. 2024.

PACHOLSKI, C. Photonic crystal sensors based on porous silicon. **Sensors**, Molecular Diversity Preservation International (MDPI), v. 13, n. 4, p. 4694–4713, 2013. DOI: https://doi.org/10.3390/s130404694. Available in:https://www.mdpi.com/1424-8220/13/4/4694. Accessed on: 20 Mar. 2024.

PAUL, B.; COOPER, J.; GALLAGHER, A.; RAYMER, M. Theory of optical near-resonant cone emission in atomic vapor. **Physical Review A**, APS, v. 66, n. 6, p. 063816, 2002. DOI: https://doi.org/10.1103/PhysRevA.66.063816.Available in: https://doi.org/10.1103/PhysRevA.66.063816. Accessed on: Nov 17. 2023.

PEDROLA, G. L. **Beam propagation method for design of optical waveguide devices**. [S.l.]: John Wiley & Sons, 2015. DOI: https://doi.org/10.1002/9781119083405 Available in: http://repositorio.ufc.br/handle/riufc/2319 Accessed on: Nov 25. 2023.

PITZ, G. A. **Collisional dynamics of the Cesium D1 and D2 transitions**. [S.l.]: Air Force Institute of Technology, 2010. Available in: https://www.proquest.com/openview/e2c0d859b22a0d78340b008d1730d5fc/1?pq-origsite=gscholar&cbl=18750. Accessed on: May 24. 2024.

POON, T.-C.; KIM, T. **Engineering optics with Matlab®**. [S.l.]: World Scientific, 2006. DOI: https://doi.org/10.1142/6166. Available in: {https://www.worldscientific.com/worldscibooks/10.1142/6166#t=aboutBook}{https://www.worldscientific.com/worldscibooks/10.1142/6166#t=aboutBook} Accessed on: oct 20. 2023.

PREBLE, S.; LIPSON, M.; LIPSON, H. Two-dimensional photonic crystals designed by evolutionary algorithms. **Applied Physics Letters**, AIP Publishing, v. 86, n. 6, 2005. DOI: https://doi.org/10.1063/1.1862783. Available in: https://pubs.aip.org/aip/apl/article-abstract/86/6/061111/117582/Two-dimensional-photonic-crystals-designed-by?redirectedFrom=fulltext. Accessed on: Oct 19. 2023.

RAFAC, R. J.; TANNER, C. E. Measurement of the ratio of the cesium d-line transition strengths. **Physical Review A**, APS, v. 58, n. 2, p. 1087, 1998. DOI: https://doi.org/10.1103/PhysRevA.58.1087. Available in: https://journals.aps.org/pra/abstract/10.1103/PhysRevA.58.1087. Accessed on: May 17. 2024.

RAYLEIGH, L. Xvii. on the maintenance of vibrations by forces of double frequency, and on the propagation of waves through a medium endowed with a periodic structure. **The London, Edinburgh, and Dublin Philosophical Magazine and Journal of Science**, Taylor & Francis, v. 24, n. 147, p. 145–159, 1887. DOI: https://doi.org/10.1080/14786448708628074. Available in: https://www.tandfonline.com/doi/pdf/10.1080/14786448708628074. Accessed on: Oct 10. 2023.

RODRIGUES, I. L. et al. **Lei de potência na distribuição de intensidade de padrão de Speckles interagindo com vapor de Césio**. Dissertação (Mestrado) — Universidade Federal da Paraíba, 2022. Available in: https://repositorio.ufpb.br/jspui/handle/123456789/25991. Accessed on: Nov 15. 2023.

RUE, R. D. L.; MCCOMB, D.; TREBLE, B.; RICHEL, A.; JOHNSON, N.; PEMBLE, M.; YATES, H. Three-dimensional photonic crystals: Approaches to fabrication. In: AMERICAN INSTITUTE OF PHYSICS. **AIP Conference Proceedings**. [S.l.], 2001. v. 560, n. 1, p. 424–448. DOI: https://doi.org/10.1063/1.1372740. Available in:https://pubs.aip.org/aip/acp/article-abstract/560/1/424/574066/Three-dimensional-photonic-crystals-Approaches-to?redirectedFrom=fulltext. Accessed on: 25 Mar. 2024.

SANTOS, F. Eroni Paz dos. **Óptica não linear em vidros especiais e filmes com nanoestruturas**. Tese (Doutorado) — Universidade Federal de Pernambuco, 2009. Available in: {https://repositorio.ufpe.br/handle/123456789/6146}{https://repositorio.ufpe.br/handle/123456789/6146} Accessed on: Nov 17. 2023.

SAXON, R. P.; OLSON, R.; LIU, B. Ab initio calculations for the x 2σ, a 2π, and b 2σ states of naar: Emission spectra and cross sections for fine-structure transitions in na–ar collisions. **The Journal of Chemical Physics**, AIP Publishing, v. 67, n. 6, p.

2692–2702, 1977. DOI: https://doi.org/10.1063/1.435183. Available in: https://pubs.aip.org/aip/jcp/article-abstract/67/6/2692/774430/Ab-initio-calculations-for-the-X-2-A-2-and-B-2?redirectedFrom=fulltext. Accessed on: Apr 07. 2024.

SCHMIDT, C. D. **Estudo da seção de choque de fotoionização de estados de Rydberg**. Dissertação (Mestrado) — UNIVERSIDADE DO ESTADO DE SANTA CATARINA-UDESC CENTRO DE CIENCIAS TECNOLOGICAS-CCT DEPARTAMENTO DE FÍSICA-DFIS PROGRAMA DE POS-GRADUAC AO EM FÍSICA-PPGF, 2012. Available in: https://oasisbr.ibict.br/vufind/Record/BRCRIS_e63c62457ee60ece33dc5e56a51d04a8. Accessed on: May 23. 2024.

SILVA, G. C. G. d. **Mistura de quatro ondas multicanal em vapor atômico**. Dissertação (Mestrado) — Universidade Federal da Paraíba, 2023. Available in: https://repositorio.ufpb.br/jspui/handle/123456789/29978. Accessed on: Apr 25. 2024.

SMITH, P.; ASHKIN, A.; TOMLINSON, W. Four-wave mixing in an artificial kerr medium. **Optics letters**, v. 6, n. 6, p. 284–286, 1981. DOI: https://doi.org/10.1364/OL.6.000284. Available in: {https://opg.optica.org/ol/abstract.cfm?uri=ol-6-6-284}{https://opg.optica.org/ol/abstract.cfm?uri=ol-6-6-284}ccessed on: nov 20. 2023.

SNIDER, R. Eigenvalues and eigenvectors for a hermitian gaussian operator: Role of the schrödinger-robertson uncertainty relation. **Electronic Research Archive**, v. 31, n. 9, p. 5541–5558, 2023. Available in: https://pdfs.semanticscholar.org/2a26/185cce9a514f959520bda220e9640b15792a.pdf. Accessed on: May 07. 2024.

STECK, D. A. **Cesium D line data**. 2003. Available in: https://steck.us/alkalidata/cesiumnumbers.pdf. Accessed on: May 20. 2024.

STONE, J.; EWING, C.; SPANN, J.; STEINKULLER, E.; WILLIAMS, D.; MILLER, R. High temperature vapor pressures of sodium, potassium, and cesium. **Journal of Chemical and Engineering Data**, ACS Publications, v. 11, n. 3, p. 315–320, 1966. DOI:https://doi.org/10.1021/je60030a007. Available in: https://pubs.acs.org/doi/abs/10.1021/je60030a007. Accessed on: Nov 28. 2023.

TOMASI, F. de; ALLEGRINI, M.; ARIMONDO, E.; AGARWAL, G.; ANANTHALAKSHMI, P. Collision-enhanced resonance of laser-diode-excited cs in a buffer gas. **Physical Review A**, APS, v. 48, n. 5, p. 3820, 1993. DOI: https://doi.org/10.1103/PhysRevA.48.3820. Available in: https://journals.aps.org/pra/abstract/10.1103/PhysRevA.48.3820. Accessed on: Mar 17. 2024.

VUKUSIC, P.; HOOPER, I. Directionally controlled fluorescence emission in butterflies. **Science**, American Association for the Advancement of Science, v. 310, n. 5751, p. 1151–1151, 2005. DOI: https://doi.org/10.1126/science.1116612. Available in: https://www.science.org/doi/abs/10.1126/science.1116612. Accessed on: Oct 19. 2023.

WERIJ, H.; HAVERKORT, J.; PLANKEN, P.; ELIEL, E.; WOERDMAN, J.; ATUTOV, S.; CHAPOVSKII, P.; GEL’MUKHANOV, F. K. Light-induced drift velocities in na–noble-gas mixtures. **Physical review letters**, APS, v. 58, n. 25, p. 2660, 1987. DOI: https://doi.org/10.1103/PhysRevLett.58.2660. Available in:

https://journals.aps.org/prl/abstract/10.1103/PhysRevLett.58.2660. Accessed on: Jun 10. 2024.

WERIJ, H.; HAVERKORT, J.; PLANKEN, P.; ELIEL, E.; WOERDMAN, J.; ATUTOV, S.; CHAPOVSKII, P.; GELMUKHANOV, F. K. **study of the optical piston**. In: OPTICA PUBLISHING GROUP. International Quantum Electronics Conference. [S.l.], 1987. p. THHH1. DOI: https://doi.org/10.1103/PhysRevA.33.3270. Available in: https://journals.aps.org/pra/abstract/10.1103/PhysRevA.33.3270. Accessed on: Oct 05. 2023.

WOOD, R. W. Fluorescence and magnetic rotation spectra of sodium vapor, and their analysis. In: JSTOR. **Proceedings of the American Academy of Arts and Sciences**. [S.l.], 1906. v. 42, n. 13, p. 235–260. DOI: https://doi.org/10.2307/20022222. Available in:https://www.jstor.org/stable/20022222?origin=crossref. Accessed on: March 15. 2024.

YABLONOVITCH, E. Inhibited spontaneous emission in solid-state physics and electronics. **Physical review letters**, APS, v. 58, n. 20, p. 2059, 1987. DOI: https://doi.org/10.1103/PhysRevLett.58.2059. Available in: https://journals.aps.org/prl/abstract/10.1103/PhysRevLett.58.2059. Accessed on: Oct 10. 2023.

ZIELINSKA, S. A new aspect of the velocity redistribution of atoms induced by a light beam and collisions: the atomic drift effect. **Journal of Physics B: Atomic and Molecular Physics**, IOP Publishing, v. 18, n. 7, p. 1333, 1985. DOI: https://doi.org/10.1088/0022-3700/18/7/014. Available in: https://iopscience.iop.org/article/10.1088/0022-3700/18/7/014. Accessed on: May 15. 2024.